Dissertation

Chemical Looping Combustion – A sustainable combustion technology for negative emission energy production

carried out for the purpose of obtaining the academic degree

Doctor technicae (Dr. techn.)

submitted at TU Wien
Faculty of Mechanical and Industrial Engineering

by

Robert Pachler
Matr.Nr.: 0525676

under the supervision of
Univ. Prof. Dr. Hermann Hofbauer
DI Dr. Stefan Penthor
Institute of Chemical, Enviromental and Biological Engineering
E166

Wien, 09. Juni 2019

Robert Pachler

Affidavit

I, Robert Pachler, hereby declare

1. that I am the sole author of the resent thesis, 'Chemical Looping Combustion – A sustainable combustion technology for negative emission energy production ', 157 pages, bound and that I have not used any source or tool other than those referenced or any other illicit aid or tool.
2. that I have not prior to this date submitted this thesis as an examination paper in any form in Austria or abroad.

Wien, 09. Juni 2019 Robert Pachler

Acknowledgement

Die vorliegende Dissertation entstand während meiner Tätigkeit als wissenschaftlicher Mitarbeiter am Institut für Verfahrenstechnik, Umwelttechnik und Technische Biowissenschaften – Forschungsgruppe Zero Emission Technologies an der Technischen Universität Wien mit finanzieller Unterstützung der Österreichischen Forschungsförderungsgesellschaft (FFG) sowie durch das 7th Framework Programm (FP7) der Europäischen Kommission. Ich möchte mich an dieser Stelle bei all jenen Menschen bedanken, die direkt und indirekt beteiligt waren und mich bis an diesen Punkt begleitet haben.

Zuallererst möchte ich Prof. Hermann Hofbauer danken, der mir die Möglichkeit gegeben hat, an diesem spannenden Thema zu forschen. Die konstruktiven Gespräche und seine passionierte Einstellung für die Wirbelschichttechnik, waren stets sehr motivierend. Des Weiteren möchte ich Stefan Penthor danken. Neben zahlreichen fachlichen Diskussionen in unserem meist zu kalt oder warmen Büro, hat er mir viele Freiheiten gegeben, mich zu entwickeln. Meinen Dank möchte ich auch all meinen Kollegen in der ZET-Gruppe aussprechen. Die unzähligen gemeinsamen Stunden an den Versuchsanlagen sowie die Nachbereitungszeit beim Bitzinger waren eine wirkliche Bereicherung.
Ein großes Dankeschön für die gemeinsame Zeit gilt meinen Kollegen aus der WTF, allen voran Markus Deutsch. Neben all dem Schabernack, war der wissenschaftliche Austausch sehr inspirierend und unsere damals endlosen Diskussionen fehlen mir heute noch manchmal.

Im für mich sehr anspruchsvollen Finale der Dissertation waren Matthias Kuba und Fritz Kirnbauer wie zwei Anker in der Brandung und haben maßgeblich dazu beigetragen, dass ich diese Arbeit fertig schreibe. Vielen Dank dafür, dass ich euch die Ohren blutig reden durfte und die unterhaltsame Zeit damals als Zimmernachbarn. Danke auch für den Tipp, ich soll keine Doktorarbeit daraus machen.

Der größte Dank gebührt natürlich meinen Eltern Magdalena und Herbert für ihre unendliche Unterstützung, sowie meiner Frau Marie-Christine für die motivierenden und aufbauenden Gespräche, wenn es mal holprig war. Sie hat mir den notwendigen Freiraum gegeben, sodass neben Familie und Beruf sich auch die Dissertation ausgegangen ist. Ihr überschwänglicher Optimismus ist bis heute sehr inspirierend für mich. Mein Sohn Maximilian danke ich für die lustigen Stunden zu zweit, die einem wieder auf den Boden der Tatsachen zurückholen und bei der Priorisierung helfen.

Abstract

Chemical looping combustion (CLC) is considered as a sustainable combustion technology for negative emission energy production. Thereby an inherent CO_2 separation is one of the main benefits of this technology. Unlike a conventional combustion, the combustion process is separated into two areas, so that fuel and combustion air are never mixed. To realize that, a metal oxide, the so-called oxygen carrier (OC), is used to deliver the necessary oxygen for oxidizing the fuel. The typical CLC system consist of two reactors which are designed as circulating fluidized beds. The oxidation of the OC takes place in the so-called air reactor and is reduced in combination with the used fuel in the so-called fuel reactor. The technology readiness level (TRL) is high for gaseous fuels, but when using solid fuels, such as biomass or coal, the developments are not so far advanced.

To contribute to the development of CLC of biomass, in this thesis experiments on two different scales of reactor systems have been conducted. Especially to evaluate the influence of fuel impurities typical for solid fuels in CLC, such as sulfur or nitrogen, investigation in a pilot plant for gaseous fuels have been performed. Additionally a novel batch reactor for gaseous and solid fuels have been developed and build, to accelerate the screening of suitable OCs with both kind of fuels. The experiments included experiments with a cooper based oxygen carrier (Cu15), perovskite and ilmenite.

Experiments in the pilot plant with natural gas as fuel and gaseous impurities, such as hydrogen sulfide (H_2S) and ammonia (NH_3) showed that, concentration of impurities and solid inventory have a big influence on the performance. During all experiments a stable operation was possible regardless which OC or impurity have been combined. Only with large amounts of H_2S the long-term operation suffer when using perovskite as OC. Fuel conversion and CO_2 yield decreased from the presence of sulfur in the system with Cu15 and perovskite. On the other hand NH_3 caused no effect on the fuel conversion or CO_2 yield with both OCs. Separate evaluation of the emissions of the air and fuel reactor showed that, at any time of the experiments the air reactor exhaust gas was not polluted. The only emissions have been in the fuel reactor off gas as SO_2 when using Cu15 and perovskite or NO only when using perovskite.

To further assess the capability of potential OCs, experiments in a novel fluidized bed batch reactor with ilmenite as OC have been performed using biomass as fuel. During the commissioning and the very first experiments, methane has been used as fuel. In a second

step wood and chicken manure pellets have been used to investigate the influence of bed temperature, fluidization rate and solid fuel dosing speed on the performance of the OC. To conclude from the batch reactor to the pilot plant, a method have been developed to evaluate the results. Due to the carbon loss in the exhaust gas, the in- and outgoing carbon could not be properly balanced. The carbon loss varies from 11 % when using methane, up to 15 % with chicken manure and 18 % with wood pellets as solid fuel. Higher hydrocarbons such as ethylene, ethane and acetylene could be confirmed, using a gas chromatograph in additional to the online gas analysis.

Publication

Journal Publications

Robert F. Pachler, Stefan Penthor, Karl Mayer, Hermann Hofbauer

Investigation of the fate of nitrogen in chemical looping combustion of gaseous fuels using two different oxygen carriers

Submitted to Energy – The International Journal, ISSN: 0360-5442

Robert F. Pachler, Stefan Penthor, Karl Mayer, Hermann Hofbauer

Fate of sulfur in chemical looping combustion of gaseous fuels using a Perovskite oxygen carrier

Fuel, 241 (2019) 432-441

DOI: 10.1016/j.fuel.2018.12.054

Robert F. Pachler, Karl Mayer, Stefan Penthor, Mario Kollerits, Hermann Hofbauer

Fate of sulfur in chemical looping combustion of gaseous fuels using a copper-based oxygen carrier

International Journal of Greenhouse Gas Control, 71 (2018) 86–94

DOI: 10.1016/j.ijggc.2018.02.006

Robert F. Pachler, Ajoy K. Ramalingam, K. Alexander Heufer, Franz Winter

Reduction and validation of a chemical kinetic mechanism including necessity analysis and investigation of CH4/C3H8 oxidation at pressures up to 120 bar using a rapid compression machine

Fuel, 172 (2016) 139–145

DOI: 10.1016/j.fuel.2015.12.044

Conference Publications

Robert F. Pachler, Mario Kollerits, Karl Mayer, Stefan Penthor, Hermann Hofbauer

Fate of sulfur in chemical looping combustion of gaseous fuels using a copper based oxygen carrier

4th International Conference on Chemical Looping, 26.-28 September, 2016, Nanjing, China

Holly, W., Lauer, T., Pachler, R., Winter, F., Bacher, C., Schuemie, H. and Murakami, S.,

Numerical Optimisation Approach for a Large Gas Engine Considering Different Fuel Gas Qualities

15th Conference "The Working Process of the Internal Combustion Engine", Graz, 2015

Poster Publication

Robert F. Pachler, Winter, F.

Lean Methane/Propane Ignition at High Pressures: Comparison of Chemical Kinetic Mechanisms

35th International Symposium on Combustion, 3.-8. August 2014, San Francisco, USA

Patent

Antrag für Solid Sampler eingereicht???

Supervised master theses

Hannes Vogtenhuber, 2015

Aufbau eines Heißgaskomponentenprüfstandes zwecks Untersuchung des Einflusses der AdBlue®-Additivierung auf die Ablagerungsneigung in der Dosierstrecke eines Euro VI NFZ-Abgasnachbehandlungssystems

Sebastian Parzer, 2018

Design, Errichtung und Inbetriebnahme einer Versuchsanlage für innovative Wirbelschichtprozesse

Content

Chapter One

1. Introduction

"You can't always get what you want.

But if you try sometime

You'll find

You get what you need"

Following the lyrics released by Mick Jagger and Keith Richards in 1969, we are meant to grow beyond ourselves. But no one says how to grow. As a result, the majority of people or societies prefer the supposedly easiest or fastest way, without thinking about the consequences. The pursuit for prosperity is omnipresent. Each of us, has dreams and goals we want to achieve. Even if they are unreachable, we are taught that we can achieve anything if we really want to.

Especially in the entire western economy, economic growth goes hand in hand with energy thirst. During the past centuries, mankind has discovered many ways to convert available energy from less desirable forms like water, wind or radiation from the sun to a more useable form of mechanical and thermal energy [1].
During the same period of time, especially since the 1950s, a significant change in temperature and atmospheric CO_2 have been observed. Compared to the centuries before, that are the fastest changes in climate ever measured. The annual report on the state of climate of the National Centers for Environmental Information and National Aeronautics and Space Administration (NASA) states, that most of the warming has occurred in the past 35 years, with 17 of the 18 warmest years on record occurring since 2001.
Phenomena such as El Niño or La Niña, which warm or cool the tropical Pacific Ocean, can contribute to short-term variations in global average temperature. Figure 1 shows temperature trends in relation to El Niño and La Niña events. Orange bars represent global temperature anomalies in El Niño years, with the orange line showing the trend. Purple bars depict La Niña years, and the purple line shows that trend. Neutral years are shown in gray, and the dashed black line shows the overall temperature trend since 1950 [2, 3].

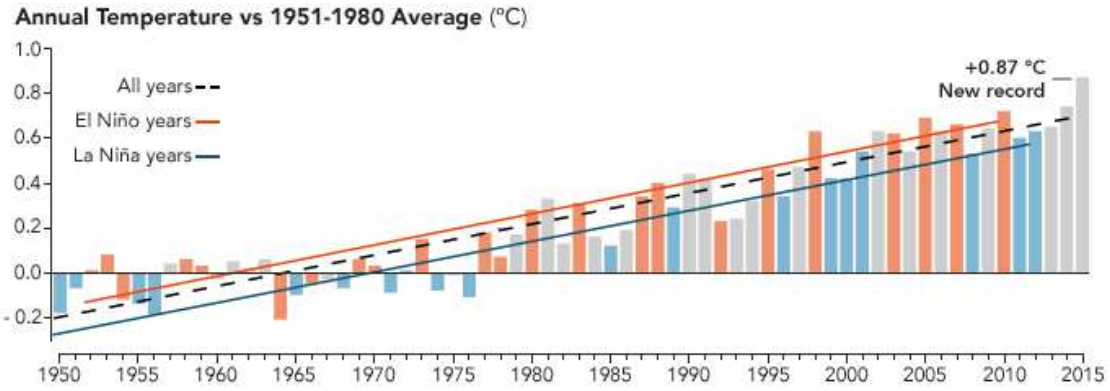

Figure 1: Temperature trends in relation to El Niño and La Niña events, red bars represent global temperature anomalies in El Niño years, with the red line showing the trend. Blue bars depict La Niña years, and the blue line shows that trend. Neutral years are shown in grey and the dashed black line shows the overall temperature trend since 1950 until 2015 [2, 3].

Carbon dioxide is the most discussed greenhouse gas in today's news. Whether the exhaust gases of an internal combustion engine or the concentration in the atmosphere, CO_2 has proven strongly harmful to the climate.

In May 2013 the concentration of CO_2, measured at Mauna Loa station, which holds the longest running record of direct measurements of atmospheric CO_2 concentration, went above 400 parts per million (ppm) for the first time in history [4]. Mauna Loa, Hawaii, is in sufficient distance to any big emitter, so that no direct emissions could influence the measurements.

In the last three centuries, the concentration of carbon dioxide in the atmosphere has increased from approximately 277 ppm in 1750 [5], the beginning of the industrial era, to 399.4±0.1 ppm in 2015 [6]. The global monthly average concentration was above 400 ppm in March through May 2015 and again since November 2015 [6]. Initially the atmospheric CO_2 increase above pre-industrial levels was primarily caused by the release of carbon to the atmosphere from deforestation and other land-use-change activities [7]. While emissions from fossil fuels started before the industrial era, they only became the dominant source of anthropogenic emissions to the atmosphere from around 1920, and their relative share has continued to increase until present [8].

Figure 2 shows historical increase of atmospheric CO_2 concentration since 1958 in the so called Keeling curve. The annual fluctuation in CO_2 is caused by seasonal variations in CO_2 uptake by land-based vegetation.

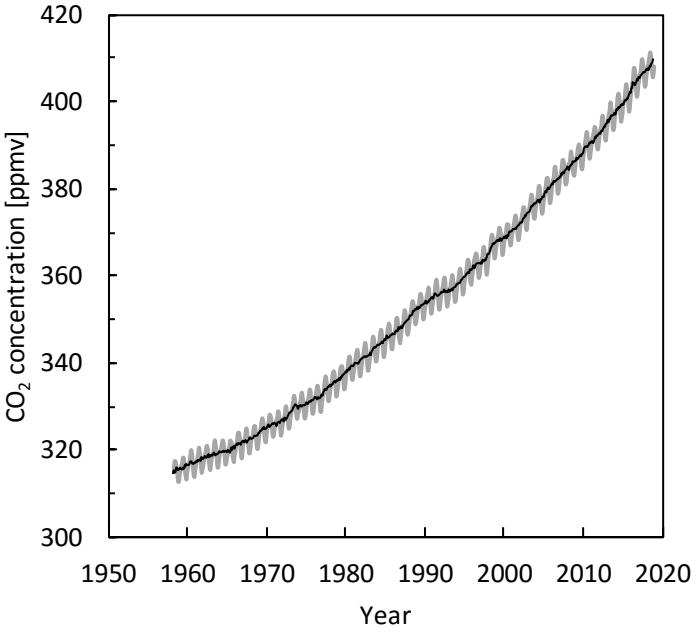

Figure 2: Trends in atmospheric CO_2 (monthly mean data) since 1958 until today measured at Mauna Loa, Hawaii [4].

1.1. Energy demand

1.1.1. Development of energy demand of human race

Earl Cook wrote in 1971 [9] that the success of an industrial society, the growth of its economy, the quality of the life of its people and its impact on other societies and on the total environment are determined in large part by the quantities and the kinds of energy resources it exploits and by the efficiency of its system for converting potential energy into work and heat.

In Figure 3, the historical development of the daily energy consumption per capita is shown. The primitives' man daily energy consumption, manly dependent on the food he could eat without discovered the use of fire, has been approximately 8 MJ. After the fire could be tamed, the energy consumption more than doubled to a value of approximately 20 MJ per day. With the development of a primitive agrarian culture including domestic livestock, the energy consumption per capita increased to approximately 50 MJ per day. In a next evolutional step livestock farming has been discovered and also animals have been harnessed for transportation. Devices have been invented to develop the power of wind and water and led to another doubling of the daily energy consumption per capita of the advanced agricultural man to approximately 100 MJ. By inventing the steam machine at the beginning of the industrial revolution, humans were no longer limited to natural energy sources and were able to commercially use concentrated energy sources such as coal, gas, and oil. In the second half of the 19th century, the peak of the industrial revolution, the daily consumption of energy has been increased to an estimated value of approximately 300 MJ per day. The modern man with a high degree of industrialization, the daily energy

consumption dramatically increased over a short period of a few generations. In 1970, the average technological man in the U.S. consumed approximately 900 MJ per day [9]. In the actual key world energy statistics from the International Energy Agency (IEA) [10] the primary energy consumption per capita in 2018 in an OECD country have been approximately 551.6 MJ per day. The occurred deviation can be attributed to the increased population, compared to 1971 estimated by Cook.

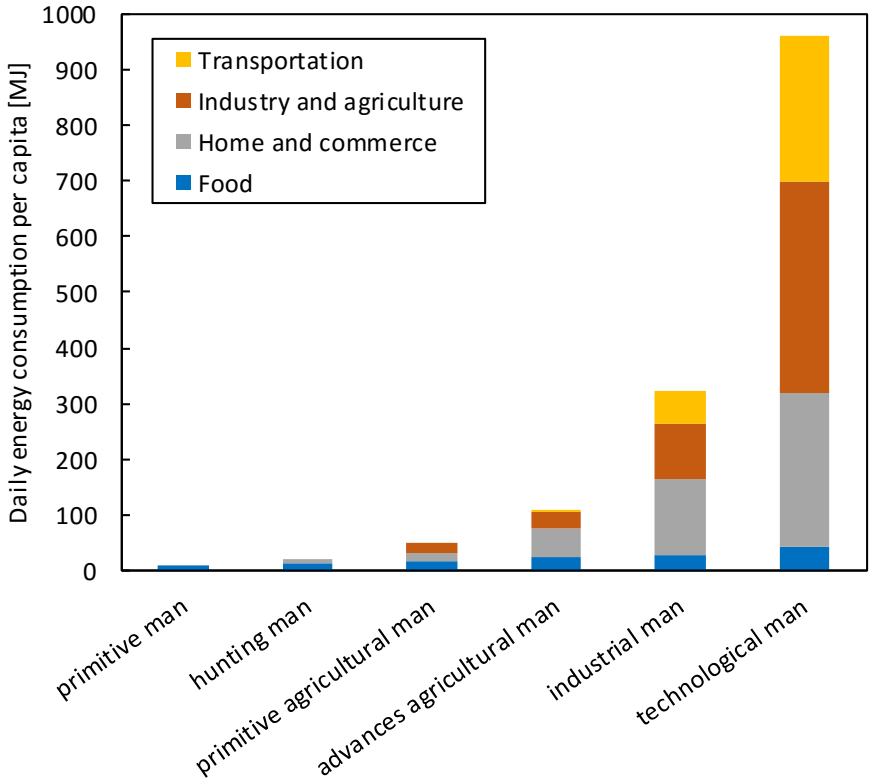

Figure 3: Estimated daily energy consumption per person over the evolution of the human race, adapted from [9].

Between 1971 and 2016, total final consumption (TFC) was multiplied by 2.25. However, the energy use by most economy sectors did not change and has been fairly stable for several years. Energy use in transport significantly increased, from 23% of TFC in 1971 to 29% in 2016 as well as in 2015. Nevertheless, in 2016 industry remained the largest consuming sector, only one percentage point lower than in 1971 (37%). The residential sector ranked third in 2016 (22%) [11].

1.1.2. Energy sources

When looking on the todays energy mix, it becomes obvious that the most of the energy produced relies on the use of coal, oil and gas (see Figure 4). At the beginning of the 19th century, the energy demand was completely covered by renewable energy sources (biomass, water and wind power). With the industrialization of the society, coal becomes more and more important for energy production. Around 1920 the produced global primary energy was 50:50 shared into renewable and non-renewable energy sources. With ongoing development of big oil fields in the U.S., crude oil and natural gas began their triumphant march into the energy production until today.

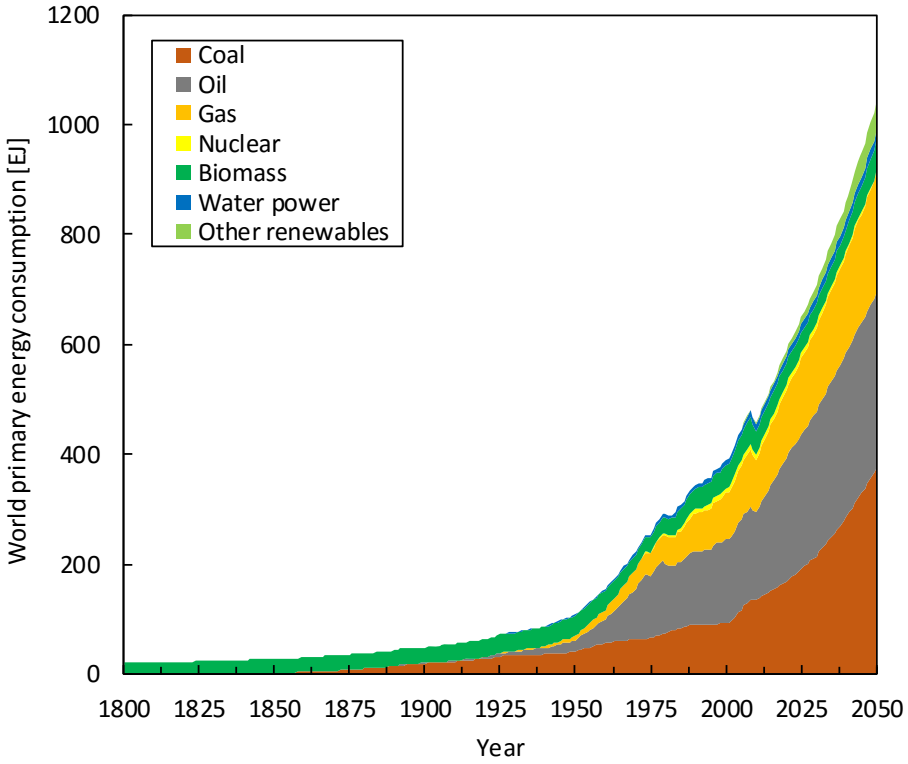

Figure 4: Development of the world primary energy consumption from 1800 to 2050. The period 2010 to 2050 follows the business-as-usual scenario developed by GEA, adapted from [12].

In 2005 less than 15 % of the consumed energy was produced from renewable energy sources. It has to be mentioned, that from 2010 the primary energy demand are based on the Global Energy Assessment (GEA) baseline scenario. The scenario includes the assumption that no additional actions to reduce the dependency on fossil fuels are set (business-as-usual), which would result in failing the 2°C target with a probability of 99 % [12].

1.2. Climate change mitigation strategies and global energy demand

When our modern industrial societies are based on the use of power - the rate at which useful work is done and power depends on energy, which is the ability to do work. Would this implicate that, like Earl Cook mentioned, everything in a modern society revolves around energy consumption? Is there really no growth or a step backwards in evolution when the current rate of increase of energy consumption stagnates or decreases? If so, the life of an American citizen must be 1.8 times better than that of an Austrian, when comparing the energy consumption per capita [13]. On the other hand Vienna has been ranked first for eight consecutive years as the most livable city worldwide and American cities had not even among the top 30 in 2018 [14]. Most likely there is no correlation between a massive energy consumption and the living standard in a sophisticated society. Mazur et al. showed in an empirical work, that the ongoing waste of substantial amounts of energy may not be necessary to maintain current living standards [15].

To reduce the emissions produced in the GEA scenario, the energy mix has to be changed sustainably. Such a high dependency on fossil fuels are not effective in terms of climate change. Further, renewable energy sources alone will not be able to cover the increase in the energy consumption. The *German Advisory Council on Global Change* (WBGU) noted, that additional to changing the energy mix, it is also necessary to limit and reduce the primary energy demand [12]. The issued scenario assumes, that this can be achieved by several measures until 2050. Manly realized by limiting the growth of the primary energy demand of the transport sector and the electricity to 1% per year, while simultaneous reducing the global heating and cooling demand yearly by 1%. Additional a drastically efficiency increase for electricity generation, the conversion from primary energy sources to electricity are assumed. About two-thirds of the total primary energy input for electricity production is lost today during the conversion from heat to electricity in form of waste heat (conversion losses from thermal production, own consumption of power plants and transmission and distribution) [16].

> *The Paris agreement shows where we want to go — the brave new world of a balanced carbon budget — but not how to get there [17].*

Different mitigation strategies can achieve the net emissions reductions that would be required to follow a pathway that limits global warming to 1.5°C with no or limited overshoot. All pathways use Carbon Dioxide Removal (CDR), but the amount varies across pathways, as do the relative contributions of Bioenergy with Carbon Capture and Storage (BECCS) and removals in the Agriculture, Forestry and Other Land Use (AFOLU) sector. This has implications for emissions and several other pathway characteristics. Figure 5 represents four illustrative mitigation pathways compatible with 1.5°C in the context of sustainable development [18].

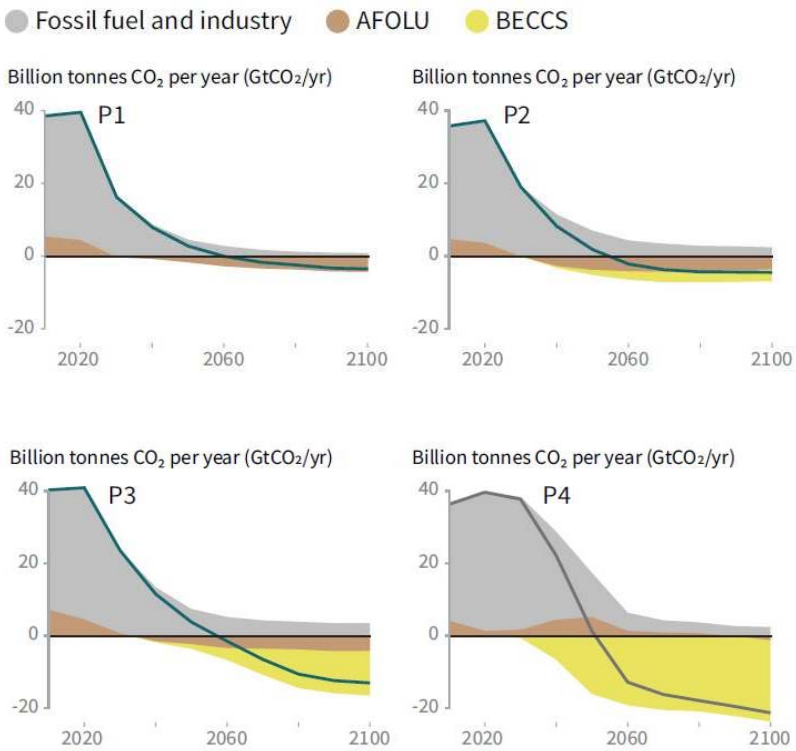

Figure 5: Global net CO_2 emissions in four model pathways (P1-P4) [18]

Beginning with the first scenario pathway (P1), in which social, business and technological innovations result in lower energy demand up to 2050, while living standards rise, especially in the global South. A downsized energy system enables rapid decarbonization of energy supply. Afforestation is the only CDR option considered, neither fossil fuels with CCS nor BECCS are used. The contribution of BECCS on net emissions reduction continuously rise from P2 to P4. Where pathway 4 is the most extreme case, a resource- and energy-intensive scenario in which economic growth and globalization lead to widespread adoption of greenhouse-gas-intensive lifestyles, including high demand for transportation fuels and livestock products. Emissions reductions are mainly achieved through technological means, making strong use of CDR through the deployment of BECCS [18].
Which pathway will be taken will be revealed in the coming years, the truth will probably be somewhere in between.

1.3. Biomass for energy production

Sources for energy, produced to meet our daily needs can be categorized in two groups, either renewable or non-renewable. Renewable energy is energy derived from sources that replenish naturally on a human timescale, while non-renewable energy sources not at all (e.g. uranium) or only slowly replenish (e.g. coal). Typical representatives of renewable energy are solar, wind, hydro, bioenergy/biomass and geothermal energy [19-21].

Biomass for energy production became a crucial part in the 2017 Energy Technology Perspectives published by the IEA. Negative emissions, notably in power generation and

fuel transformation, became critical as low-carbon ambitions rise. In the Beyond 2°C Scenario (B2DS), BECCS delivers almost 5 gigatonnes of "negative emissions" in 2060. These negative emissions are key to the energy sector, becoming emissions-neutral by 2060. While BECCS technologies face substantial challenges, they compensate for residual emissions elsewhere in the energy system that are even more technically difficult or costly to abate directly. This will require massive technological learning and scale-up in both sustainable bioenergy and CCS, which have been lagging behind so far [22]. Biomass is the oldest source of consumer energy known to mankind and is still today the largest source of renewable energy, accounting for 10% of world's total primary energy supply. The bioenergy technology roadmap envisages world total primary bioenergy supply increasing from 50 EJ today to 160 EJ in 2050, with 100 EJ of this for generation of heat and power [23].

Biomass can be used as source for a wide range of energy products like electricity, heat and fuels for transport. It releases the exact same amount of carbon that has been bound during the growth period and during the conversion process and can thus be considered as carbon neutral. A number of conversion pathways are available to produce different forms of energy. This includes direct conversion into heat via combustion or intermediate conversion into a gas via e.g. gasification, pyrolysis or fermentation and subsequent utilization. Utilization options are again production of heat via combustion or synthesis of liquid fuels or chemical products [24]. The rationale for using biomass can be summarized as [23]:

- Biomass is a unique source and can be provided as gaseous, solid and liquid fuel.
- It can be used for generating electricity, heat and transport fuels.
- It can be used in industry to generate high temperature heat.
- Biomass can be stored at times of low demand and provide dispatchable energy when needed.
- It exists high potential of generating additional sources of income along the whole value chain, from cultivation to energy production.

1.4. Carbon capture and utilization (CCU)

1.4.1. Potential of CCU

As an alternative to storing captured CO_2 in geological formations, in the oceans, or in mineral form as carbonates, net CO_2 emissions to the atmosphere can be reduced by using CO_2 either directly or as a feedstock in chemical processes that produce valuable carbon containing products. The utilization of CO_2 establishes an inventory of stored CO_2, the so-called carbon chemical pool, primarily in the form of carbon-containing fuels, chemicals and other products [25]. The production and use of these products involve a variety of different 'life cycles' (i.e., the chain of processes required to manufacture a product from raw materials, to use the product for its intended purpose and ultimately to dispose of it or to reuse it in some fashion). Depending on the product life-cycle, CO_2 is stored for varying periods of time and in varying amounts. As long as the recycled carbon remains in use, this

carbon pool successfully stores carbon. Withdrawal from this pool, by decay or by disposal typically re-injects this carbon into the atmospheric pool [26].

Utilization of captured CO_2 for industrial processes is already economical in some applications and could have co - benefits in terms of accelerated development of capture technologies and CO_2 transport infrastructure. Commercial CCU connections between carbon sources and applications could develop infrastructure and capture technology that could then be used in the longer term in combination with permanent storage. In primary chemicals production, CCU accounts for almost 6 Gt CO_2 by 2060 in the B2DS, of which 97 % is carbon capture from CO_2 emissions from ammonia production for making urea.
Of the global cumulative CO_2 captured and stored in the B2DS, 39% is in China and 13 % is in the Middle East. Primary chemicals production is expected to double in China and more than double in the Middle East by 2060 from current levels [22].

1.4.2. The carbon cycle

The Earth's climate and the carbon cycle are inherently linked. Carbon cycle processes determine the flow of carbon between reservoirs. Figure 6 represents the main carbon flows among atmospheric, land, ocean and geological reservoirs. The first illustration (a) shows the earth before significant anthropogenic impacts and how carbon flows have or may have changed due to anthropogenic activities such as (b) industrial era fossil fuel combustion or (c) when carbon dioxide removal (CDR) begins, but net CO_2 emissions are positive. The last illustration (d) shows when CO_2 is removed from the atmosphere, i.e., "net negative emissions". It have to be mentioned, that in scenario (d) still positive emissions are possible but not depict. As well as carbon exchanges shown in (a; black and dashed lines) also occur in b, c, and d. In the atmosphere, the carbon-containing gases carbon dioxide and methane, along with water vapor, are the major greenhouse gases (GHGs). These GHGs absorb a proportion of the Earth's emitted long-wavelength radiation, thereby trapping heat. CO_2 in particular is a very long-lived greenhouse gas, whose atmospheric concentration has been rising at unprecedented rates due to continued intensive fossil fuel use, land use change, and cement production [27].

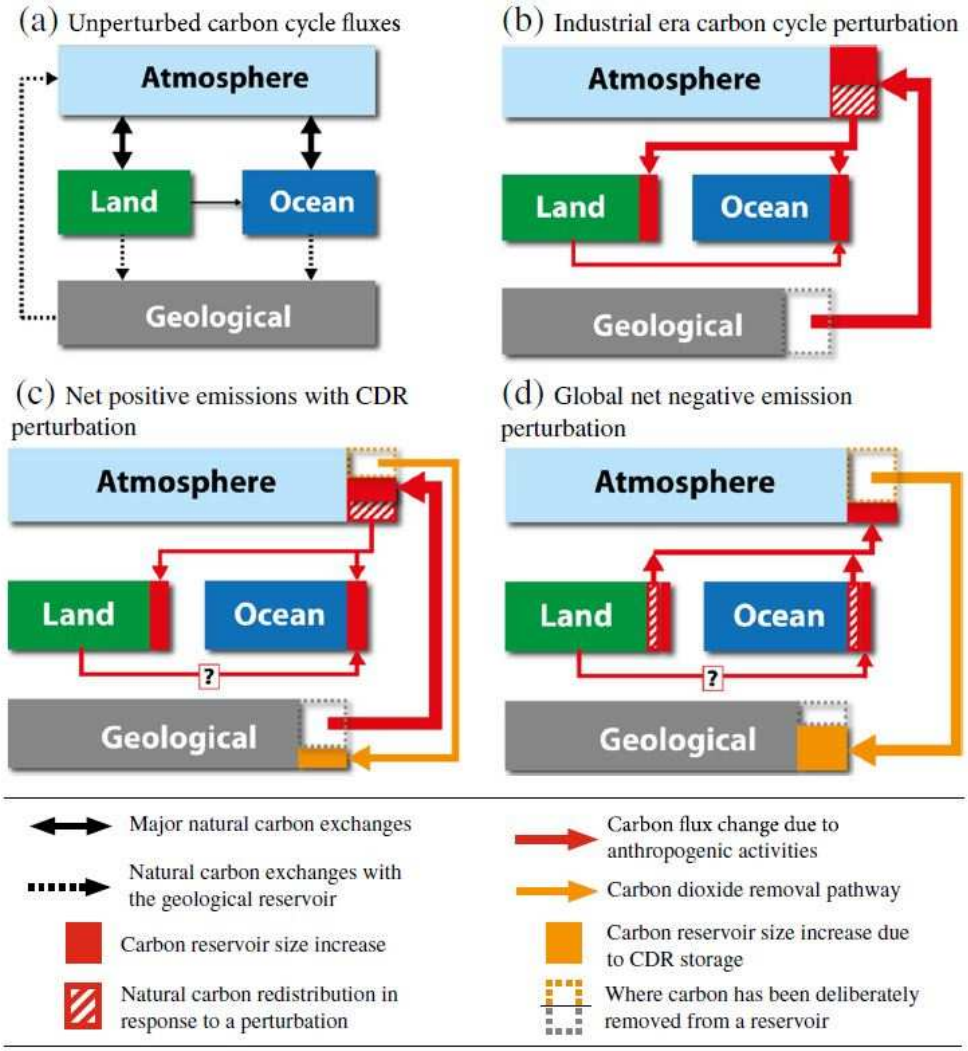

Figure 6: Main carbon flow among atmospheric, land, ocean and geological reservoirs [27]

As atmospheric CO_2 levels continue to rise the likelihood of "severe, pervasive, and irreversible" impacts increases [28]. This was recognized by the United Nations Framework Convention on Climate Change, who facilitated the Paris Agreement on climate change [29] in which countries pledged Nationally Determined Contributions (NDCs) to deliver emissions reductions. However, the emissions reductions resulting from current NDCs appear to be insufficient to limit warming to "well below 2°C above pre-industrial," the goal of the Paris Agreement [30]. Consequently, it is increasingly likely that some form of carbon dioxide removal will be needed [31-34] to reach this goal [27].

At present, CDR methods and technology are immature and untested at scale [35], so our understanding of their potential and impacts, including possible carbon cycle feedbacks, are reviewed from limited investigations. For example, many studies extrapolate from natural analogues or local applications, modeling and/or laboratory investigations, and in some cases a small number of pilot projects. However, these are insufficient for a full assessment of CDR and so there is a pressing need to advance research and, where relevant, the development of CDR technologies [17].

1.4.3. Carbon capture technologies

Table 1 gives a short overview of proposed CDR methods that investigate carbon cycle responses on large-scale (e.g. $>$ 1 Pg C) deployment [27].

Table 1: Description of proposed carbon dioxide removal (CDR) methods where enough literature exists to understand how the carbon cycle may respond to large scale deployment, adapted from [27]

Method	General description
Direct air capture of CO_2 with storage	Technology that chemically or electro-chemically removes CO_2 from air and concentrates it for storage
Bioenergy with carbon capture and storage	Grow terrestrial vegetation and use the biomass to create biofuels that can be burned in conjunction with carbon capture and storage technology
Afforestation/reforestation	Plant or restore forests to increase CO_2 uptake (via primary production) and storage in biomass and soils
Soil and land carbon management	Employ management practices, such as no-till agriculture, irrigation, cover crops, compost amendments, wetland restoration, and fire management, to increase C retention and storage in agricultural soils or managed natural lands
Biochar	Pyrolyze terrestrial biomass to form biochar and add it to soils where the C can remain sequestered (biochar is recalcitrant); biochar amendments may also enhance vegetation productivity and soil carbon storage
Enhanced weathering on land	Spread alkaline minerals on land to chemically remove CO_2 from the atmosphere in reactions that form ions, which are eventually transported to the ocean, or in some cases solid minerals (geological sequestration), may also enhance vegetation productivity and subsequently soil carbon storage
Ocean alkalinization	Increase the alkalinity of the upper ocean to chemically increase the carbon storage capacity of seawater and thus, also increase CO_2 uptake
Ocean fertilization	Add micronutrients like iron or macronutrients like nitrogen and phosphorus to increase phytoplankton growth (CO_2 fixation) and ocean carbon storage via the biological pump (the transport of this fixed carbon into the deep ocean)
Artificial ocean upwelling	Use pipes or other methods to pump nutrient rich deep ocean water to the surface where it has a fertilizing effect; see ocean fertilization above

When looking for carbon capture technologies, they can be categorized into four basic groups of approaches:

- Post-combustion capture: CO_2 is removed from an exhaust gas after the combustion step by absorption (e.g. using amine solutions) or adsorption (e.g. via pressure swing processes). This kind of technology is the most mature capture technology and can be applied to any kind of combustion process [26].
- Pre-combustion capture: This category includes all technologies where fuel is decarbonized before the combustion process. The most famous technology is the integrated gasification cycle process (IGCC), where a gasification step transforming the solid fuel into a gas. In a water-gas-shift reactor the energy is concentrated in H_2 and carbon is shifted to CO_2. By physical or chemical processes the CO_2 is separated from the gas stream, to further use the hydrogen in the energy conversion process.
- Oxyfuel combustion: Instead of ambient air, a mixture of pure oxygen and recycled exhaust gas is used for combustion. The resulting exhaust gas stream consists only of CO_2, water vapor and trace pollutants. The oxygen demand is covered by an air separation unit, which in turn is mainly responsible for the energy penalties of this technology.
- Unmixed combustion: This is a new form of combustion, where air and fuel are not mixed [36]. Two separate reactors, the air reactor and the fuel reactor, are connected with each other and in-between oxygen is transported. Thereby two exhaust gas streams are yielded, a gas stream out of the air reactor consisting of oxygen depleted air and the second exhaust gas stream a mixture of CO_2 and water vapor out of the fuel reactor. One of the main advantages of this technology is the lack of an energy demanding gas-gas separation step. The investigations in this thesis have been conducted with the chemical looping technology, which belongs to the group of unmixed combustion and is often named as a representative of the next generation carbon capture technologies.

1.4.4. Chemical looping combustion

The concept of chemical looping combustion (CLC) goes back originally to the 1951 proposed concept by Lewis et al. [37] but the term was first used by Ishida et al. in 1987 [38] who also proposed it as carbon capture technology [39]. CLC is an innovative combustion technology and can be attributed to the family of unmixed combustion technologies.
Figure 7 gives a general overview of the combustion process. As can be seen, the process is divided into two steps or reactors. In a first step a metal-oxide, the so-called oxygen carrier, is oxidized by combustion air in the air reactor, before entering the fuel reactor. In a second step the oxygen carrier delivers the oxygen necessary for oxidation of the fuel in the fuel reactor and is subsequently reduced while the fuel is oxidized.

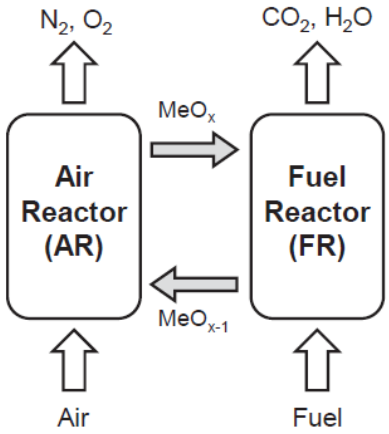

Figure 7: Basic concept of chemical looping combustion

The two separate resulting exhaust gas streams, ideally only consist of the combustion products CO_2 and water vapor when exiting the fuel reactor and oxygen depleted air when exiting the air reactor. The fact that CO_2 is captured inherently with nearly no energy penalty makes CLC a highly efficient combustion concept. Avoiding the energy intensive gas-gas separation step, CLC has been identified as one of the most efficient processes for carbon capture [40].

1.5. Bioenergy in combination with carbon capture and storage (BECCS)

The Paris Agreement in 2015 set the objective of limiting the global average temperature increase to 2°C by reducing the GHG emissions and within them, CO_2 emissions [29]. To reach this goal, it becomes necessary to develop not only neutral but also negative carbon emission technologies (NETs) during the present century [17, 41]. Fossil-fuel CCS is capable to realize zero emission energy production, but when combining bioenergy with CCS (BECSS), negative greenhouse gas emissions can be achieved and thus CO_2 is consequently removed from the atmosphere [18, 23]. BECCS has a wide area of use and can be applied to almost all biomass conversion routes like bio-chemical, thermo-chemical or traditional combustion [42]. In the 2013 proposed technology roadmap for carbon capture and storage [43] the application of BECCS in biofuels production is a perfect application for CCS deployment since biofuel production processes already yield nearly pure CO_2 streams. Wallquist et al. [44] showed that the public perception for CCS decreases when bioenergy is involved.

1.6. Aim of this work

The still strongly increasing worldwide energy demand, in combination with the established goal of limiting global average temperature rise to 2°C in the Paris Agreement of 2015, are contradictory and make drastically reduction of GHG emissions inevitable [29]. As mentioned before, the cornerstone of the today energy production are fossil fuels. Therefore a method for sustainable energy production would help in the short to medium term to reduce environmental threats caused by CO_2 or nitrogen oxides emissions. To be able to take countermeasures timely, not only neutral but also negative carbon emissions technologies (NETs) have to be developed during the next decades [17]. Chemical Looping Combustion of solid fuels, especially biomass (BECCS) is one of the possibilities with several benefits in terms of sustainable energy production with negative CO_2 emissions and a high technology readiness level (TRL).

In a first step, the performed experiments in this work should help to understand the behavior of fuel impurities in Chemical Looping Combustion typical for solid fuels, such as sulfur or nitrogen. In several test series in a 120 kW dual circulating fluidized bed reactor (DCFB) for gaseous fuels, the experiments with a cooper based oxygen carrier and perovskite have been conducted using natural gas with gaseous impurities in form of hydrogen sulfide (H_2S) and ammonia (NH_3).

Due to the size of the pilot scale reactor system including high personnel and operating expenses and the challenging task to keep as many parameters as constant as possible, in a second step a novel fluidized bed batch reactor have been developed and build. The reactor system has been designed, constructed and commissioned within this thesis and first experiments with ilmenite as oxygen carrier and two different kind of solid fuels and methane have been conducted.

The main goal was to contribute to the development of CLC of biomass through experimental work at 2 different scales. Within the scope of this dissertation, three master theses have been created and one supervised [45-47].

Chapter Two

2. Chemical looping combustion

2.1. General aspects

When looking for a promising combustion technology for reducing global CO_2 emissions, chemical looping combustion (CLC) is, by its ability of inherently capturing of CO_2 a sustainable and/or zero emission power generation technology [48]. Because CLC is a so-called unmixed combustion technology, the energy intensive gas/gas separation step is not needed and a reduction of costs and energy penalties in industrial application are the consequence.
CLC was originally proposed as a process for production of CO_2 from any carbonaceous fuel in 1951 by Lewis et al. [37]. Four decades later Ishida and Jin [39] proposed it in 1994 for inherently capturing CO_2 from combustion processes (see Figure 8).

In a CLC system, fuel and combustion air are never come in contact with each other (see Figure 8). The system consists of two reactors, an air reactor (AR) and a fuel reactor (FR). In between a so-called oxygen carrier (OC) is responsible for transporting the necessary oxygen for oxidation from the AR to the FR. The OC, a metal oxide, is alternately reduced by the introduced fuel during the combustion step and is oxidized by combustion air in another step. This procedure can either be made in batch mode or by circulating it between two separate reactors. In this doctoral thesis, the experiments are mainly conducted using a 120 kW circulating fluidized bed reactor system. Additional in chapter 6 the first results of experiments with a new developed batch reactor system will be discussed.
A general thermodynamic analysis of CLC has been performed by Jerndal et al. [49]. The oxidation reaction of the OC which occurs in the AR is:

$$MeO_{\propto-1} + \frac{1}{2}O_2 \rightarrow MeO_{\propto} \tag{1}$$

The general reduction reaction of the OC by fuel in the FR is:

$$\left(2x + \frac{y}{2} - z\right) MeO_{\propto} + C_xH_yO_z \rightarrow \left(2x + \frac{y}{2} - z\right) MeO_{\propto-1} + \frac{y}{2}H_2O + xCO_2 \tag{2}$$

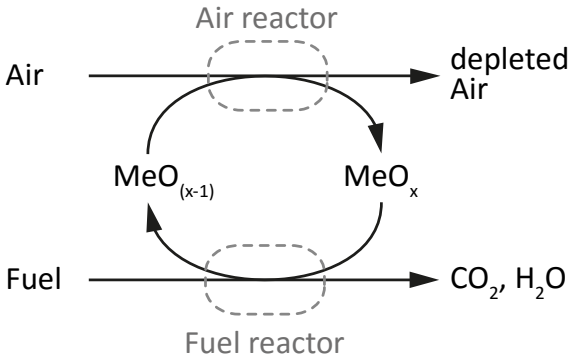

Figure 8: Basic scheme of the chemical looping combustion process.

Leakages from the AR to the FR are prevented, thus no nitrogen is involved into the combustion step and only CO_2 and H_2O exit the FR. After condensation of H_2O, a highly concentrated CO_2 stream is available for further processing. The AR exhaust stream contains the excess O_2 and N_2. The total heat release, during the combustion (oxidation + reduction step) in two separate reactors, is exactly the same as in conventional combustion processes [50].

2.2. Oxygen carriers

In CLC, beside the reactor design the OC is one of the most crucial parts of the system. The performance of the OC influences process efficiency and economics to the same extent. The constant increasing number of lab scale and pilot scale reactor systems leads to a steadily expanding knowledge on CLC, gained by the continuously growing community [51], identified beside perovskite type OC the materials Ni, Cu, Fe and Mn as potential candidates [52-56]. The most important requirements of a modern OC for a sustainable process are the following [51]:

- High reactivity with fuel and oxygen
- The ability for complete fuel conversion
- High oxygen transport capacity
- Low tendency for agglomeration
- High mechanical stability and thus a long particle lifetime
- Low environmental impact and harmless to human beings
- Good economic performance

The equilibrium reaction of CO and H_2 determine the maximum achievable fuel conversion with the metal oxide:

$$CO + MeO_{\propto} \leftrightarrow CO_2 + MeO_{\alpha-1} \tag{3}$$

$$H_2 + MeO_{\propto} \leftrightarrow H_2O + MeO_{\alpha-1} \tag{4}$$

The ability of the OC to convert fuel is on the one hand dependent on thermodynamics and on the other by the reactivity. Thereby the amount of oxygen, the OC is capable to transport, is crucial and is expressed by the oxygen transport capacity R_O:

$$R_O = \frac{m_{ox} - m_{red}}{m_{ox}} \tag{5}$$

Where m_{ox} is the sample mass in fully oxidized form and m_{red} is the fully reduced mass of the OC.
Table 2 shows the values of R_O for the most relevant pure redox systems. Even though nickel based OCs are thermodynamically limited, when using gaseous fuels they are still among the best performing OCs found in literature [57-59] because of high reactivity. To strengthen the mechanical stability of the pure OC, the active metal is mixed with an inert support material.

Table 2: Oxygen transport capacity for relevant OC systems

OC system	**R_O [kg/kg]**
CuO-Cu	0.2011
Fe_2O_3-Fe_3O_4	0.0334
Mn_3O_4-MnO	0.0699
NiO-Ni	0.2142

As long as there is no perfect OC available on the market, the reactor system has to be able to cover the weaknesses of some OCs by the ability of adjustability during operation.
Economically, fixed costs like the raw material, respectively production costs of the particles, are crucial in the same sense as characteristics, like the particle lifetime, that affect the operating costs. Therefore high production costs, can be compensate with a long particle lifetime and vice versa. Conventionally OC particles are manufactured but can be of natural origin like ores either. Artificial produced particles can be waste or by products from industry, e.g. steel production, or synthetically manufactured particles, e.g. by spray-drying or impregnation on a highly porous support material [58].

There are two types of OCs, which either can be natural origin or synthetically manufactured particles. The first category are so-called iG-CLC (in-situ gasification CLC)

oxygen carriers, where the fuel is converted via gas-solid reactions and secondly CLOU – chemical looping with oxygen uncoupling, where oxygen can be released gaseous [55, 60, 61]. In the experiments conducted either with the 120 kW dual fluidized pilot plant or with the newly designed batch fluidized bed reactor, three different types of both categories of bed materials have been used as OC.

2.2.1. Cooper based oxygen carriers

Due to its thermodynamic ability to completely convert the fuel into CO_2 and H_2O, its high reactivity, high oxygen transport capacity and low toxicity towards human beings [62], copper has the potential to be a suitable OC [63]. The main disadvantages are the higher material costs compared to materials like Fe or Mn. Additionally the low melting point of elemental Cu of 1085°C [64] is limiting the operating temperature and thereby the thermodynamics. In literature results can be found with natural and synthetic particles with and without CLOU capabilities [57, 58, 65-71]. To increase the mechanical strength of synthetically produced particles, the active Cu is often mixed with an inert support like Al_2O_3, SiO, ZrO_2 or $MgAl_2O_4$ [72-75]. The way the support material interacts at operating temperatures with the active metal, influences the mechanism of oxygen release (iG-CLC or CLOU) [62, 72, 76]. Zhou et al. [77] introduced a model for a CuO OC, capable for both types, iG-CLC and CLOU. The model is based on reaction rates between 750 to 980°C determined in a bench scale fixed bed unit. In García-Labiano et al. [78] strategies for waste management for Cu based OCs have been proposed.

2.2.2. Perovskite oxygen carriers

Perovskite type minerals have the common composition of calcium titanate ($CaTiO_3$), with the generalized perovskite structure of ABO_3, where the cation on the A site is larger than the one on the B site. Synthesized multicomponent perovskites can also be made, thereby the cations from the A and B site are replaced to form a new structure in the form of $A_{1-x}A'_xB_{1-y}B'_yO_3$ [56, 79]. Perovskites e.g. $CaMnO_{3-\delta}$ have been investigated as oxidation and reduction catalysts [80, 81]. Perovskite is a typical OC for a CLOU process, due to the property to release oxygen in atmospheres with low oxygen partial pressure [82]. Bakken et al. [83] investigated the influence of the oxygen partial pressure on $CaMnO_{3-\delta}$ and found a correlation between $3 - \delta$ and oxygen partial pressure. The higher the oxygen concentrations is, the higher the material is oxidized. Further Bakken et al. [84] and Leonidova et al. [85] studied the decomposition of the perovskite under deep reduced conditions and examined structural changes during oxidation and reduction. Various test with perovskite type OC materials investigated among others the effect by replacing manganese with MgO to $CaMnO_{3-\delta}$ [86] and replacing wider range of the B site [87] and validated that perovskite type OC materials hav e a great potential in CLC applications. Experiments have been conducted by Ryden et al. [88] using a $300W_{th}$ unit, using a perovskite with titanium and manganese at the B site.

2.2.3. Ilmenite oxygen carriers

Due to its good fluidizability, low agglomeration tendencies, and low decrease in reactivity [89, 90], ilmenite is a promising candidate for the use with solid fuels. In literature it has been used in pilot plant units up to 100 kW fuel input [91-98]. A comparison of different bed materials including ilmenite have been published by Berdugo Vilches et al. using a 12 MW_{th} circulating fluidized bed boiler [99] Tan et al. [100] were carried out experiments in a pressurized thermogravimetric analyzer to study the effect of H_2S on the reactivity. First operational results are published by Ströhle et al. in a 1 MW chemical looping plant using ilmenite and hard coal as fuel [101, 102].
Further, in the project 'Negative CO_2 Emissions with Chemical Looping Combustion of Biomass' a project consortium from Denmark, Finland, Iceland, Norway and Sweden are focusing on the use of cheap and readily available minerals such as ilmenite or manganese ore in Chemical-Looping Combustion of biomass (Bio-CLC)[103].
In the group of OCs with natural origin, ilmenite has been investigated in detail by Borowiec and Rosenqvist [104] and Nell [105], which studied the solid chemistry and phase interaction extensively. Ilmenite is mainly composed of titanium-iron oxide ($FeTiO_3$), where iron oxide is the active phase that behaves as oxygen carrier [57]. Kintetics of redox reactions have been investigated by Abad et al. [106].

2.3. Reactor systems

Beside the OC, the reactor system represents the second crucial part of a CLC system. The OC can either be operated in a fixed bed, a fluidized bed or a rotating bed. A combination of fixed bed and fluidized bed is another concept of operation and is called moving bed. No matter which type of fluidization is used, the OC is alternately oxidized and reduced [57, 58, 107-110].
The reactor systems can be designed as two or more interconnected fluidized beds, where the OC is the bed material. To avoid gas leakage between the reactors when using a multiple reactor design, the fluidized beds are connected via steam or CO_2 fluidized loop seals. The main requirements of a modern CLC fluidized bed system are:

- High gas-solid contact for maximum gas conversion.
- Sufficient bed material inventory for full fuel conversion.
- Optimum solids circulation between AR and FR to ensure oxygen transport and keep temperature difference between the reactors as low as possible.
- Low mechanical and thermal stress on particles and thus low particle attrition.
- Excellent gas-solids contact and therefore sufficient solids circulation even under part-load operation.
- Small reactor footprint.

As mentioned before, the two main important components in a CLC systems are the OC and the reactor design, which must be harmonized with each other. The reactor system

design has to take the characteristics and demands of the OC into account and should be adapted to the operating conditions. Abad et al. [111] investigated solids circulation, solids inventory, solids residence time and temperature for the most usual metal oxides (CuO, Fe_2O_3 and NiO) and different fuel gases (CH_4, H_2 and CO). Mayer et al. [55] investigated the different demands of oxygen carriers on the reactor system in a 120 kW_{th} pilot plant.

2.3.1. The dual fluidized bed system

The Dual Circulating Fluidized Bed concept (DCFB) is shown in Figure 9, which consists of two fluidized beds [112, 113], the AR and FR. The two reaction zones are interconnected by two steam fluidized loop seals, the upper loop seal (ULS) and the lower loop seal (LLS) to prevent gas leakage. The solids circulation between AR and FR is mainly controlled by the AR fluidization rate.

In the AR, air is used for fluidization, while the gaseous fuel itself (natural gas, propane, syngas etc.) is used to fluidize the FR. All loop seals are fluidized with steam. When leaving the AR, the oxidized particles are separated from the gas stream in a cyclone and transported to the FR via the ULS. In the FR, the particles are reduced by the gaseous fuel, fed to the system, and transported back to the AR via the LLS. To adjust the internal solids circulation independently from the global solid circulation, the FR additionally contains an internal solids circulation loop with a steam fluidized loop seal (internal loop seal - ILS). The design and benefits of the DCFB system have been described by Kolbitsch et al. [112]. Various results obtained with this reactor concept can be found in literature [55, 68, 114-119].

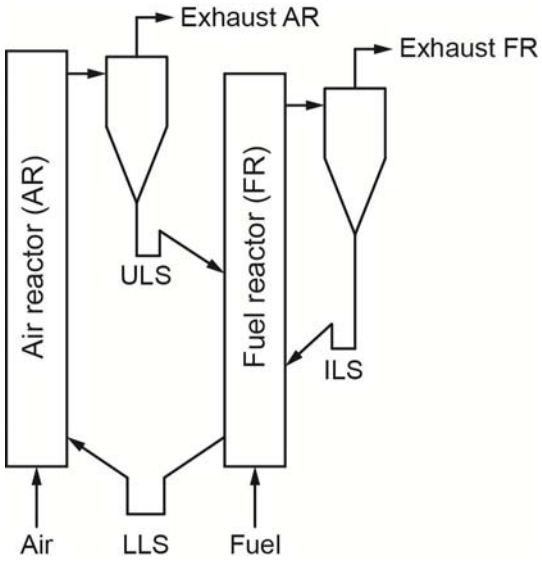

Figure 9: The Dual Circulating Fluidized Bed (DCFB) concept

2.4. Chemical looping combustion of biomass

In order to reach the target set in the Paris Agreement of 2015, the global average temperature rise should be limited to 2°C, which makes a drastically reduction of GHG inevitable [29]. To reach this goal, not only neutral but also negative carbon emissions technologies (NETs) have to be developed during the next decades [17]. Using solid fuels, especially biomass in the CLC process is one of the possibilities with several benefits in terms of sustainable energy production with negative CO_2 emissions (Bio-CLC and BECCS). The direct use of solid fuels in a CLC reactor systems leads to several difficulties which have to be faced [120].

In contrast to gaseous fuels, solid fuels have to be dried, devolatilized and decomposed, where they stepwise break down into gaseous compounds (Figure 10). Compared to the fast step of devolatilization, the gasification of the char, using H_2O and CO_2 is one of the slowest and limiting steps [121].The main gasification reactions are:

$$C + H_2O \rightarrow CO + H_2 \tag{6}$$

$$CO + H_2O \rightarrow CO_2 + H_2 \tag{7}$$

$$CO_2 + C \rightarrow 2CO \tag{8}$$

Due to the long lasting gasification step and because the char particles are expected to be well mixed with the oxygen carrier, a partial transportation to the AR is most likely during operation. To minimize the loss of char to the AR, the residence time in the FR has to be as long enough to maximize the fuel conversion. Solid fuel components like ash and inert content have to be separated from the oxygen carrier and removed from the system [122].

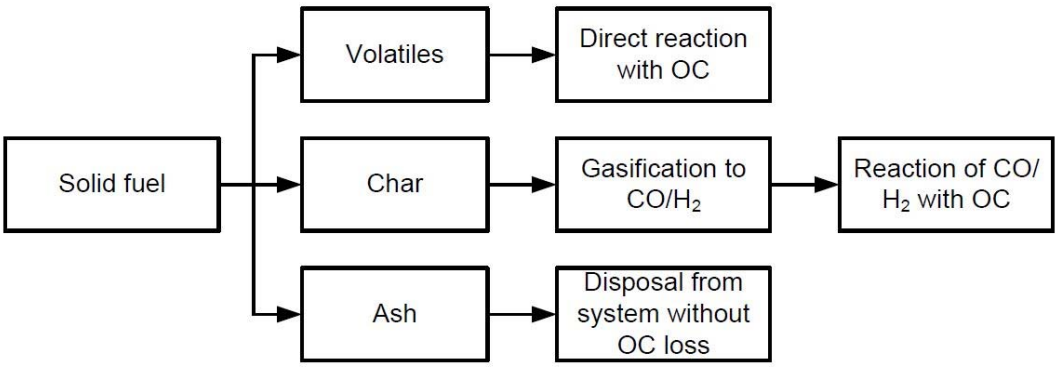

Figure 10: Basic path of conversion of solid fuels in CLC [63]:

Besides the possibility of being a NET, BioCLC is also attractive because of the combustion characteristics of biomass. When using biomass at operating temperatures around 900 °C (typical for the FR), it has a very high volatile content (up to 85% of the dry organic matter). Additionally char from biomass shows very high reactivity compared to char from coal [123]. Biomass also shows low contents of ash and other pollutants like sulfur. Due to

the fact, biomass does not contain fossil carbon, it is considered carbon neutral, when CO_2 emissions caused by char lost to the AR [63].
In summary, CLC of solid fuels requires different design criteria of the reactor as well as other main properties of the OC, compared to gaseous fuels. The main requirements are following [124]:

- Fuel feeding: To ensure a high fuel conversion, the solid fuel has to be fed in an optimum way into the FR, which allows good gas/solid contact between the volatiles and the OC.
- Retention time: Due to the fact, the gasification of char happens very slowly, the FR design has to be suitable to improve the retention time of the solid fuel, in order to avoid char to enter the AR. In the AR, char will produce CO_2 emissions which are not captured.
- OC dilution: Because solid fuels usually contain ashes, this should be considered when selecting an OC. During operation, the increasing ash content in the bed material leads to a continuous dilution of the OC. Remedy for this problem, a separation of the ash will cause inevitable a loss of bed material too. Therefore an affordable OC with good reactivity has to be selected.

Lyngfelt et al. published 2017 a summary of the recent progress and status of CLC of solid fuels. More than 70 different materials have been used in operation of small CLC pilots, as reported from more than 150 publications. Totally, more than 9000 h of operation have been reported, of which >3000 h have been conducted with solid fuels [125]. Substantial contributions to solid-/ BioCLC were made by the research groups Instituto de Carboquímica (ICB-CSIC) from Zaragoza, the Chalmers University of Technology and the Thermoenergy Engineering Research Institute of the Southeast University.

A very comprehensive overview of BioCLC gives the investigations of Mendiara et al. [41, 126-128] and Adánez-Rubio et al. [129, 130] from CSIC. In [128] an overview of the status of development of the use of biofuels in chemical looping technologies, including chemical looping combustion (CLC) and chemical looping with oxygen uncoupling (CLOU) for the production of heat/electricity, as well as chemical looping reforming (CLR), chemical looping gasification (CLG) and chemical looping coupled with water splitting (CLWS) for syngas/H_2 generation can be found. Further the main milestones in the development of such processes are shown, and the future trends and opportunities for CL technology with biofuels are discussed. In Mendiara et al. [41, 126, 127, 129, 130] experiments have been performed at the ICB-CSIC-s1 unit. This lab scale unit allows operation between 0.5 (iG-CLC) and 1.5 kW (CLOU), with different types of forest and agricultural residues (pine wood in form of pine sawdust or milled chips, olive stone and almond shell) as fuels. The publications comparing an iron ore OC, a Cu based (60 wt% active CuO content) and a mixed Cu-Mn oxide (34 wt% active CuO and 66 wt% Mn_3O_4 content) CLOU-OC prepared by spray-drying. The carbon capture efficiency was high for all OCs (>90%), reaching 100% carbon capture efficiency under certain conditions were achieved with the CLOU particles as well as with the iron ore. Calculations based on the experimental results also showed that the necessary amount of OC in the FR to reach 95% carbon capture efficiency is significantly

lower using the CLOU-OC. With the Cu-Mn oxide 100% combustion efficiencies were achieved.
Schmitz et al. from Chalmers investigated the performance of a Ca-Mn based CLOU-OC, using wood char of different origins and sizes as fuel in a 10 kW unit [131]. An additional publication from Schmitz et al. investigated the performance of a sintered manganese ore within the same 10 kW unit and a 100 kW pilot unit [132]. During the experiments with both OCs, almost full fuel conversion was achieved, resulting in carbon capture efficiencies up to 100%. The sintered manganese ore achieved compared to the Ca-Mn based CLOU-OC a higher lifetime, while gas conversion performance was similar.
Shen et al.[133] from the Southeast University examined pine sawdust and an iron ore as OC in a 10 kW unit consisting of two interconnected reactors. Further Gu et al. [134] investigated the effect of temperature on gas composition of both the FR and AR, conversion efficiency of carbonaceous gases, carbon capture efficiency, and oxide oxygen fraction using recycled CO_2 as fluidization and gasification agent. The experiments have been conducted with mixtures of coal and biomass and an iron ore as OC in a 1 kW unit with a similar design to the 10 kW unit used by Shen et al. in [133]. After the experiments, analysis of used OC particles showed depositions of alkali metals from biomass ash on the particles without influencing reactivity or causing agglomerations. Gu et al. [135], examined the interaction between biomass ash and iron ore oxygen carrier during chemical looping combustion more closely. The fuel conversion was significantly influenced by the addition of biomass ash by sintering effects of the OC, including a reactivity decrease.

Further Pérez-Astray et al. [136] and Moldenhauer et al. [137] released experimental results obtained in laboratory-scale, circulating fluidized-bed CLC systems under both iG-CLC and CLOU modes.

2.5. Pollutant emissions in CLC

2.5.1. Assessment of emissions in CLC

Due to the fact that the CLC system consists of two different reactors, the situation of pollutant emissions for CLC is different than in traditional combustion processes. From the two different exhaust gas streams out of the AR and FR, only the exhaust gas stream out of the AR is emitted to the atmosphere, therefore needs to comply with environmental guidelines, while the FR exhaust gas is further processed in carbon capture and utilization (CCU) or carbon capture and storage (CCS). Therefore it has to meet different criteria (e.g. SO_2 or NO_X), depending on the planned application of the FR exhaust gas stream (e.g. CO_2 as resource for chemical processes, transportation via pipelines, enhanced oil recovery, etc.).

In current European pollutant regulations, the amount of released pollutants are based on the generated exhaust gas stream from the combustion process, i.e. mg/Nm^3 dry flue gas. [138, 139]. For novel combustion technologies such as CLC, this kind of limits are not up to date and needs to be newly rated. A more modern approach was published by Normann et al. [140] and suggest to relate the amount of emitted pollutants to the energy produced or

the total energy input, i.e. in mg/MJ, which would also takes the overall plant efficiency into account. In the United States of America an evaluation like this is already part of regulations [63].

Due to the different purpose of exhaust gases, emissions from AR and FR have to be evaluated separately. When using CO_2 in following industrial applications, the effect of impurities on the liquefied product have to be assessed regarding concentration limits for transportation as well as health and safety considerations, e.g. unplanned venting [63]. The effects of impurification such as N_2, O_2, Ar or SO_X on CO_2 injection and storage has been investigated by Wang et al. [141-143]. To describe the effect of impurities on the fundamental properties of CO_2 mixtures and their impact on the chain integrity and economies, Neele at al. have developed an impact toolbox which comprises new experimental data, thermodynamic reference models for CO_2 mixtures relevant for CCS and the framework for CCS risk assessment taking Health Safety & Environment aspects, the impact of the quality of the CO_2 and CCS chain integrity into account [144].

2.5.2. Formation of nitrogen oxides in combustion processes

The overall reaction sequences for the formation of NO_X and N_2O in conventional air combustion are fairly well-established [145, 146]. Nitric oxide (NO) is besides nitrogen dioxide (NO_2) and nitrous oxide (N_2O) the most relevant species and responsible for 90% of total emissions in combustion processes. NO_2 is subsequently formed in the atmosphere by oxidation of NO. N_2O contributes to the greenhouse effect in the troposphere and participates in ozone depletion in the stratosphere but occurs only at lower combustion temperatures, e.g. fluidized bed combustion [147, 148]. The generally accepted pathways for NO_X formation are the following three mechanisms [148, 149].

Thermal NO formation results from N_2 and O_2 reacting at high temperatures (above 1500 °C). The mechanism involves three reactions, known as the extended Zeldovich-Mechanism [150].

$$N_2 + O \leftrightarrow NO + N \tag{9}$$

$$N + O_2 \leftrightarrow NO + O \tag{10}$$

$$N + OH \leftrightarrow NO + H \tag{11}$$

The prompt NO is formed when hydrocarbon radicals in fuel-rich zones attack molecular nitrogen to form cyanide species, which subsequently form NO when oxidized. These reactions can take place at temperatures lower than required for thermal NO formation.

Fuel NO is derived from nitrogen in the fuel, reacting through either volatile-N or char-N. Nitrogen released with the volatiles further decomposes into cyanide and amine species. These intermediate species may react to produce N_2 or NO, depending on the conditions. Char-N reacts through heterogeneous reactions and intermediate CN species to eventually produce NO or N_2. Detailed understanding of the reaction pathways for the conversion of

char- N has not been established and is still an area of active research. The split between NO and N_2 on an overall level depends on factors such as the nitrogen content of the fuel, its rank and volatility, as well as the stoichiometry [151].
Glarborg et al. [145] generally assumed that up to 20% of the total NO_X formed from e.g. pulverized coal combustion in air is due to thermal NO_X and about 80-100% is derived from fuel-N while the prompt NO_X mechanism is negligible, depending on the quantity of fuel-bound nitrogen species.
Normann et al. [152] measured and modelled the oxidation of ammonia over a copper oxide (CuO) under conditions relevant to CLOU in a lab scale fluidized bed reactor and showed that, under most of the conditions, NH_3 is fully converted into NO or N_2. It is further mentioned, that metal-based oxygen carriers interact with nitrogen in both oxidized and reduced states. In a well-mixed furnace, it can be expected that oxidized and reduced metal oxides will be present simultaneously. It is feasible that the metal oxide will provide a surface for catalytic oxidation:

$$N + \frac{1}{2} O_2 \rightarrow NO \tag{12}$$

The mobility of oxygen in the oxide would make it possible for non-catalytic reactions to occur:

$$Me - O + N \rightarrow Me + NO \tag{13}$$

Ammonia may also be catalytically decomposed to N_2 and H_2 according to the following reaction:

$$2NH_3 \rightarrow N_2 + 3H_2 \tag{14}$$

Reaction (14) has been shown to be catalyzed by metals, such as Fe-dolomite, iron sinter, and nickel. There is also the possibility that the reduced metal oxide reacts with nitrogen oxides to form N_2 through the following overall reaction:

$$2Me + 2NO \rightarrow N_2 + 2Me + O_2 \tag{15}$$

The oxygen carrier may also catalyze the reduction of NO by the fuel, for example, carbon monoxide (CO). The importance of the fuel may be attributed to the regeneration of active sites or to direct reduction, catalyzed by a surface, as follows:

$$CO + Me - O \rightarrow CO_2 + Me \tag{16}$$

$$NO + CO \rightarrow \frac{1}{2} N_2 + CO_2 \tag{17}$$

2.6. Existing CLC batch reactor systems

Until today, there are a number of various CLC batch reactors in different research institutions in use. Beside Chalmers University of Technology [91], the Department of Energy and Environment, Instituto de Carboquimica (CSIC) [64] and University of Stuttgart [153] have introduced small lab-scale fluidized bed reactors for process development.

Leion et al. [91] investigated the influences of the amount of steam in the reducing cycle and of bed temperature on the fuel conversion rate. As fuel, 0.2g of different types of coal were used per cycle. For the investigations, two different oxygen carriers have been used as bed material. The reactor has a height of 870 mm and has a porous quartz plate as nozzle plate with a diameter of 10mm (Figure 11). To minimize the discharge of bed material and unburned fuel, the inside diameter of the reactor widens up (45 mm) above the quartz plate. Nitrogen with 5% oxygen was used as oxidation medium and nitrogen with steam as reduction medium, while the volume flows varied around 600Nml/min.

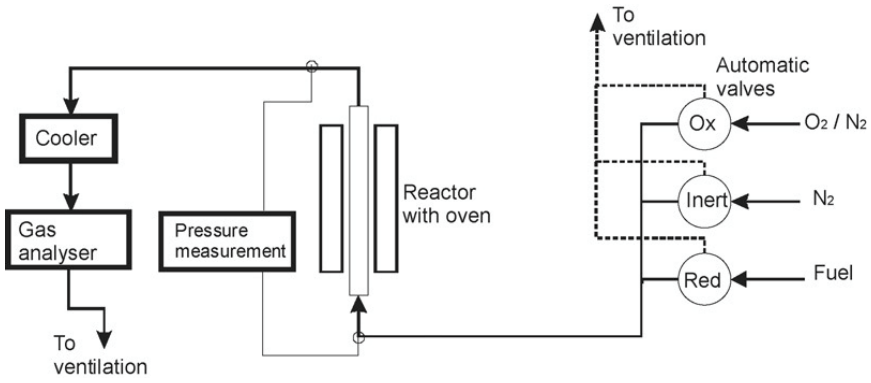

Figure 11: Schematic layout of the laboratory setup [91]

Another batch reactor was described by de Diego et al. [64]. Experiments with different oxygen carriers have been performed using 200g of bed material with a bed temperature of 800°C. As reducing agent, methane was used and between the cycles, the reactor system was purged with N_2. The fluidized bed reactor has an inner diameter of 54 mm and a height of 500 mm. Before the fluids enter the reaction zone, they have to pass a 300 mm high preheating zone (Figure 12). To determine the amount of lost bed material or unburned fuel, filters have been used. For quantifying the tendency and amount of agglomeration of an OC, the pressure loss over the bed has been measured.

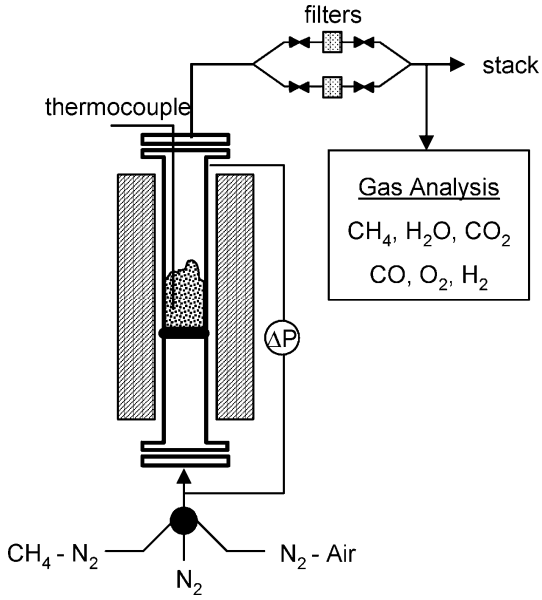

Figure 12: Experimental setup used for multicycle tests [64]

Linderholm et al. [154] investigated the influence of temperature on coke conversion when using hard coal, carried out in a circulating fluidized bed system, with no circulation of the bed material in batch mode (Figure 13). To be able to study only coke gasification in the iG-CLC process, the fuel was previously treated with heat to remove volatile components.

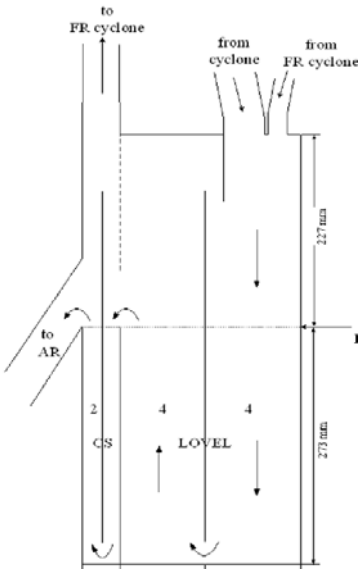

Figure 13: FR scheme of the reactor for batch experiments [154]

Bidwe et al. [153] conducted batch experiments in a circulating fluidized bed pilot plant using ilmenite as OC. The oxygen capacity as well as the reactivity with CO, H_2 and CH_4 were investigated as a function of the number of cycles. For the oxidation of the bed material, air has been used for fluidization and for the reduction cycle a mixture of CO, H_2

and N_2 has been used. Between the cycles, the FR have been purged with N_2. In addition, coal was used as fuel to study the oxygen capacity of ilmenite. For this purpose, the fuel was fed into the FR until the exhaust gas composition was constant. Thus, the available oxygen has been consumed and a pure gasification reaction occurred. Before switching to the oxidation cycle where all existing species have been burned, the reactor have been purged with N_2.

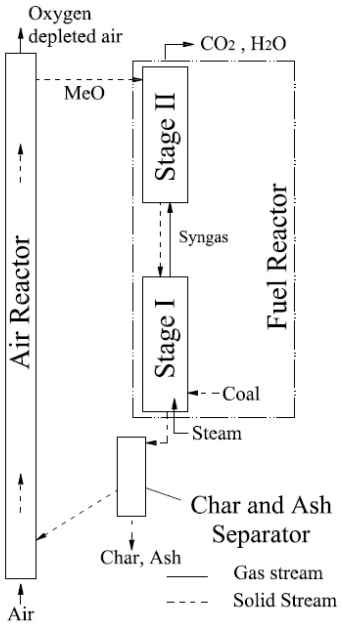

Figure 14: Scheme of the circulating fluidized bed reactor [153]

Chapter Three

3. Fundamentals

3.1. Fluidized bed technology

3.1.1. Classification of particles

In fluidized bed technology the description of particles and their properties is an important component. The bed material in a fluidized bed consists of a great variety of individual particles. Consequently, there are parameters that describe the individual particles and parameters that classify the entire mass of particles. The particle diameter only partially reflects the actual particle properties, since most particles deviate from the ideal of a sphere. For this reason, mainly equivalent diameters are used for the description (see Table 3). In addition, the form factor φ is used, which describes the deviation to a volume equal sphere. [155]

Table 3: Equivalent diameter and form factor

designation	***formula***
Sieve diameter	d_P
Volume-related diameter	$d_V = \sqrt[3]{6 * \frac{V_P}{\pi}}$
Surface-related diameter	$d_S = \sqrt{\frac{O_P}{\pi}}$
Surface/volume-related diameter (Sauter mean diameter)	$d_{SV} = 6 * \frac{V_P}{O_P}$
Shape factor	$\phi = \left(\frac{d_V}{d_S}\right)^2$

A particle cluster can be described with the particle size distributions (d_i, x_i), the porosity ε and the bulk density ρ_B. An important possibility of the divisibility of bulk materials is the Geldart method [156]. The difference between particle density and gas density is plotted as a function of the particle sauter mean diameter (see Figure 15).

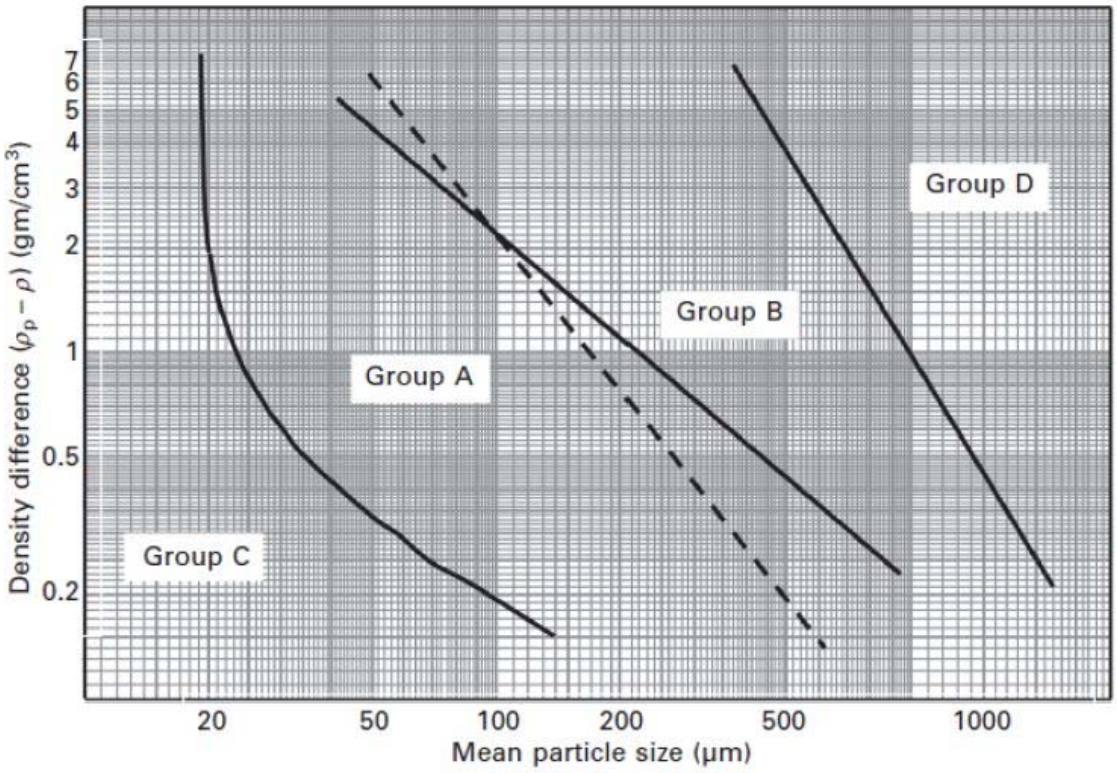

Figure 15: Particle classification by Geldart [156]

The four areas in the diagram represent different property groups [156].

Group A: This group includes particles with small particle diameter and / or low particle density. With increasing gas velocity, a bed expansion first occurs and only later bubbles. E.g: cracking catalysts.

Group B: In contrast to group A, in group B bubbles are formed beginning with the minimum fluidization velocity. Bubble formation enables very good solids mixing. E.g.: quartz sand

.

Group C: Bulk solids that exhibit strong cohesive behavior belong to group C. Fluidization of these particles is very difficult and therefore less suitable for fluidized bed applications. Particles of this category are very small and strongly differ from the shape of a sphere. E.g.: flour.

Group D: The particles of group D are large and / or have a high density. Therefore, bubbles rise more slowly than the fluidizing medium. This has the consequence that the solids mixing is relatively low and the gas exchange in the bubbles is rather high. E.g.: coffee beans.

3.1.2. Operating modes of fluidized beds

To fluidize the bed material, a fluid is introduced though openings in the bottom of the reactor. Depending on the fluidization velocity, different operating states of the fluidized bed occur (see Figure 16).

The fluidization velocity is referred to the superficial gas velocity U and represents the flow velocity in an empty tube.

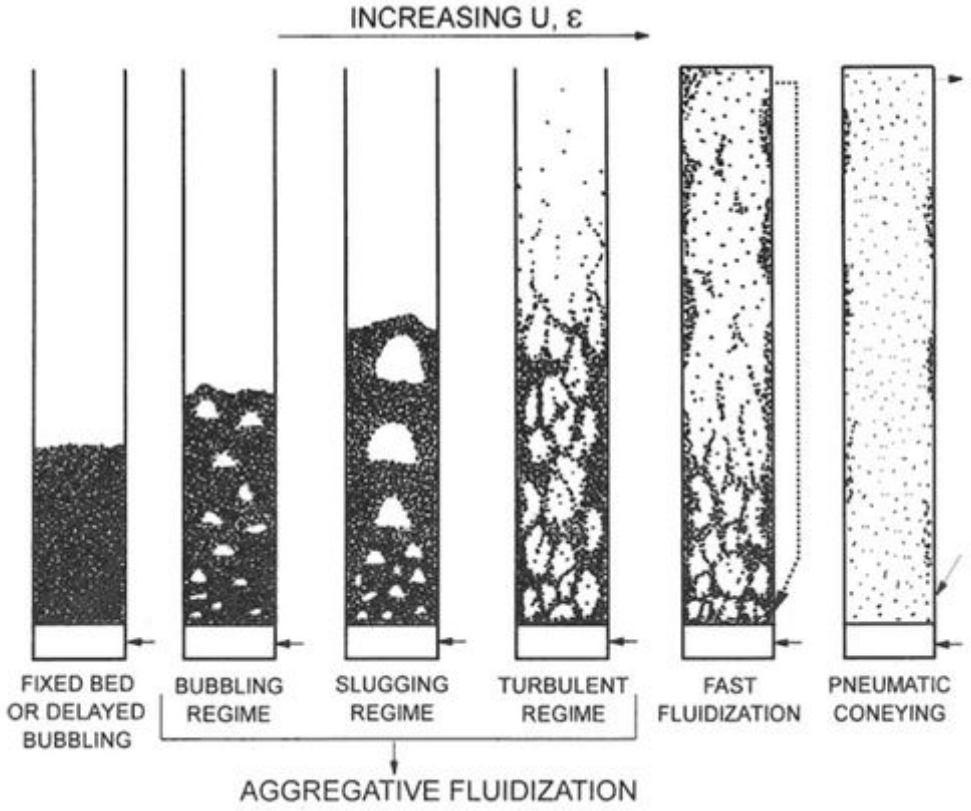

Figure 16: Flow patterns in gas- solids fluidized beds [157]

A fixed bed is formed when the bed of loose particles forms a solid packing. When the fluidization increase, the fix bed is still present but the bed starts to expand until the minimum fluidization velocity is reached. Thereafter bubbles are formed and migrate through the bed and burst at the bed surface. Form this point on, the prevailing flow patterns belong to the fluidized bed regime.

A special form of the bubbling fluidized bed is the slugging fluidized bed. An increasing gas velocity and a small fluidized bed diameter cause the bubbles to enlarge until the reach a diameter similar to the fluidized bed diameter. If the superficial gas velocity is further increased in a bubbling fluidized bed, separated particles are discharged into the area above it. This condition is called a turbulent fluidized bed and is characterized by a good gas-solid contact. If the bed material is evenly distributed in the reactor, it is called fast fluidized

bed. In this case, a significant portion of the bed material is discharged and must therefore be returned to the reactor to ensure a constant bed material inventory. If the gas velocity is clearly above the terminal velocity of the individual particles, this is referred as pneumatic transport. [158]

In addition to the gas velocity, the particle density, particle shape and gas properties, such as density and viscosity, have a significant influence on the fluidization properties. Figure 17 shows the pressure drop in the fluidized bed as a function of the superficial gas velocity U. The minimum fluidization velocity U_{mf} represents and indicates the transition from packed bed to fluidized bed region. Through a fluidized bed, the pressure drop is constant with increasing superficial gas velocity. Depending on the characteristics of the bed material, this condition will persist until the regime of fast fluidization begins. With particles in Group D of the Geldart classification, the transition starts when the terminal velocity U_t is exceeded. Then the pressure drop increases again and pneumatic transport takes place and the bed material is discharged [159].

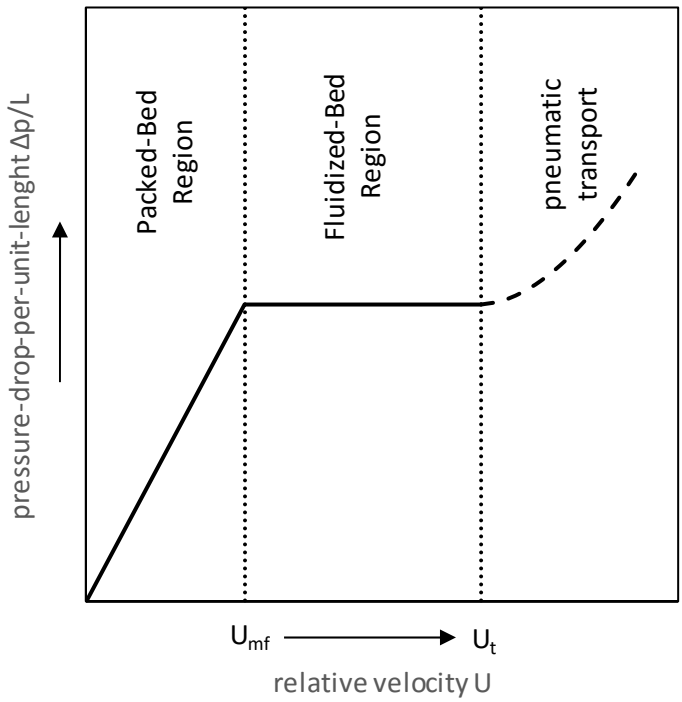

Figure 17: Pressure drop related fluidization curves for particles in Group D of the Geldart classification

To make statements about the operating state of a fluidized bed, the diagram according to Grace [160] is used. With the help of dimensionless key figures, such as the Reynolds number Re and the Archimedes number Ar, the classification is made.

$$Re = \frac{U * d_P * \rho_g}{\mu} \tag{18}$$

$$Ar = \frac{\rho_g * {d_{SV}}^3 * (\rho_p - \rho_g) * g}{\mu^2} \tag{19}$$

The Grace diagram shows the dimensionless gas velocity U^* as a function of the dimensionless particle diameter ${d_p}^*$ (see Figure 18).

$$U^* = \frac{Re}{Ar^{1/3}} \tag{20}$$

$${d_p}^* = Ar^{1/3} \tag{21}$$

This diagram shows all the main operating states. The fixed bed regime is present in the area below U_{mf}. In the area between U_{mf} and U_c is the area of the bubbling fluidized beds. The turbulent fluidized bed regime lies between U_c and U_{se}. The area just above U_{se} represents the fast-fluidized bed.

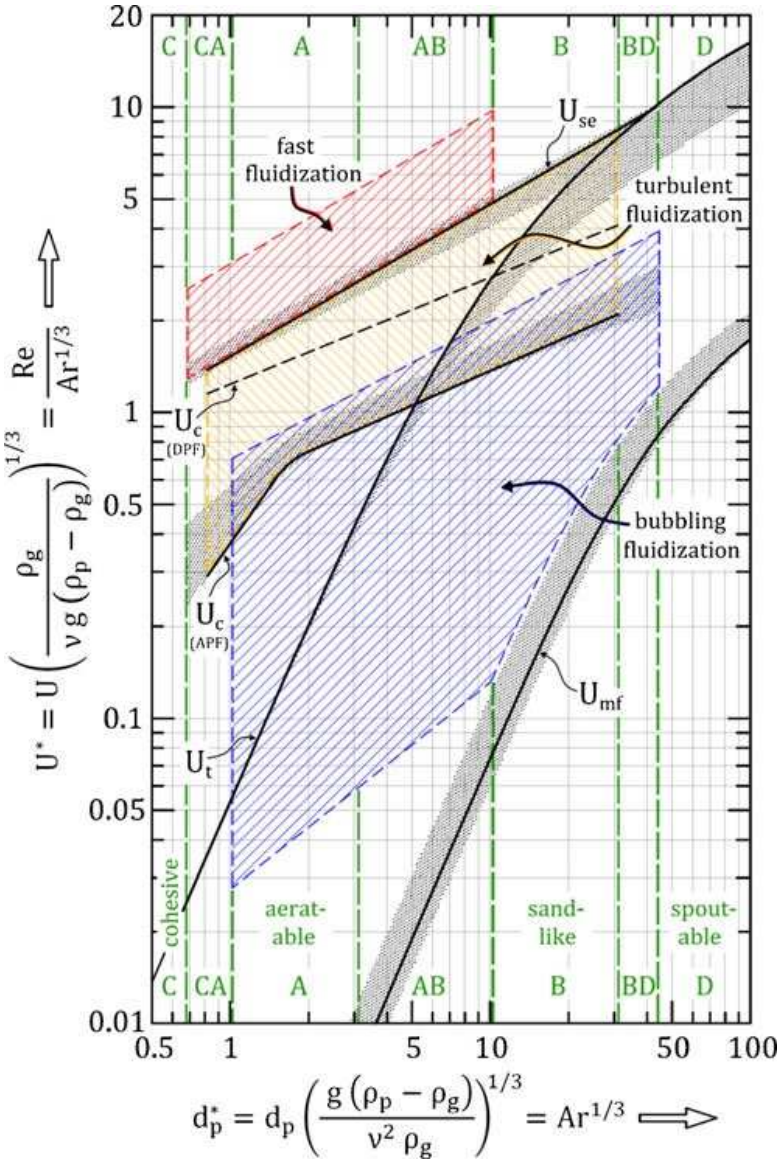

Figure 18: Grace Diagram with adaptions from Schmid et al. [161]

Chapter Four

4. Experimental setup pilot operation

4.1. 120 kW CLC pilot plant for gaseous fuels

A 120 kW_{th} chemical looping pilot plant (Figure 19) designed as a dual circulation fluidized bed (DCFB) system has been used in this work. The system consists of two reactors, an AR and FR. The two reaction zones are interconnected by two steam fluidized loop seals, the upper loop seal (ULS) and the lower loop seal (LLS) to prevent gas leakage. The solids circulation between AR and FR is mainly controlled by the AR fluidization rate [112].

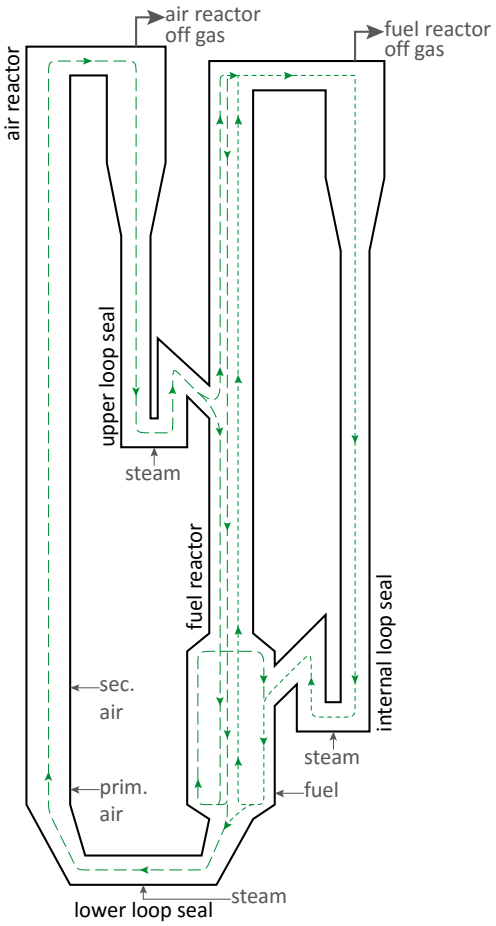

Figure 19: Scheme of the 120 kW CLC pilot plant

As mentioned in section 2.3.1, in the AR, air is used for fluidization, while the gaseous fuel itself (natural gas, propane, syngas etc.) is used to fluidize the FR. All loop seals are fluidized with steam. When leaving the AR the oxidized particles are separated from the gas stream in a cyclone and transported to the FR via the ULS. In the FR, the particles are reduced by the gaseous fuel fed to the system and transported back to the AR via the LLS. The composition of the used natural gas from the Viennese gas grid for the experiments can be found in . To adjust the global solid circulation independently from the internal solids circulation, the FR additionally has an internal solids circulation loop with a steam fluidized loop seal (internal loop seal - ILS). The design and benefits of the DCFB system used in this study have been described by Kolbitsch et al. [112]. Various results obtained with this reactor concept can be found in literature [55, 68, 114-117].

Table 4: Composition of natural gas from the Viennese gas grid

Species	Concentration [vol%]
CH_4	96.61
C_2H_6	1.49
C_3+	0.54
H_2	0
CO_2	0.30
N_2	1.05

Exhaust gases from AR and FR are collected, mixed and subsequently burned using a gas burner (fire tube burner, FTB), to ensure that no combustible gases are emitted into the atmosphere via the stack.

Regular solid sampling from the DCFB under hot conditions during operation is possible due to a specially constructed device. The samples are taken from the ULS (representing AR) and the LLS (representing conditions in the FR). The sampling procedure and method for determination of OC oxidation states has been described by Kolbitsch et al. [162].

4.1.1. Data evaluation using mass and energy balances

The experimental data obtained with the 120 kW pilot plant have been evaluated using the process simulation software IPSEpro. Figure 20 shows the model of the 120 kW pilot plant proposed by Penthor [63]. Both AR and FR have been modeled as a single balance zone and the solid OC is circulating between them.

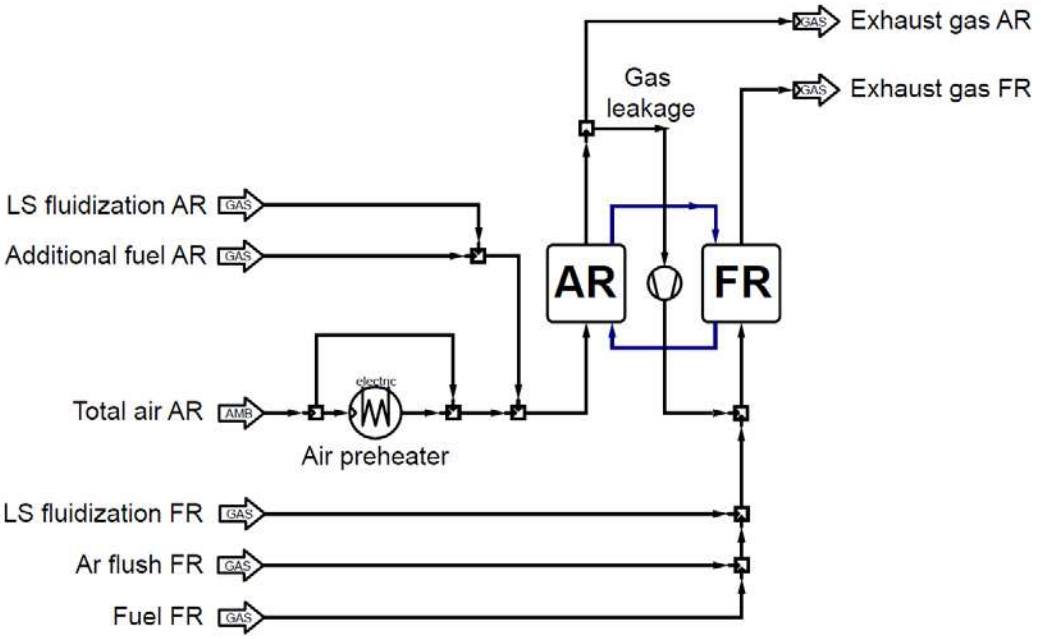

Figure 20: Flowsheet of the 120 kW CLC pilot Unit in IPSEpro used for data validation and evaluation [63]

The in- and outgoing gas streams of each reactor are summarized prior to entering the reactor including fluidization gases of the loop seals. Here, LLS fluidization is fully included in the gas stream entering the AR and the fluidization streams of ULS and ILS are completely added to the streams entering the FR. Gas leakage between AR and FR via the ULS is modeled as well. The model also allows intermediate access to process parameters like solids circulation between the reactors and several performance parameters based on fuel conversion. In the present work, solids circulation between the two reactors is not measured but calculated based on reactor temperatures, gas conversion and solids conversion.

4.2. Additional analytical methods and equipment

4.2.1. SEM/EDS analysis

To determine the morphology of the fresh and used oxygen carrier material a scanning electron microscope (SEM) combined with energy dispersive X-ray spectroscopy (EDS) was used. Thereby the collected solid samples were either loose or embedded in epoxy, cross-sectioned and polished analyzed.

4.2.2. ICP-OES/XRF/CHNS analysis

For quantifying the amount of deposited sulfur an inductively coupled plasma optical emission spectrometry (ICP-OES), a x-ray fluorescence spectroscopy (XRF) and an elemental analysis (CHNS) have been used.

For the ICP-OES measurement, 20-30 mg of the sample was weighed into a Teflon tube and then added with 7 ml of concentrated nitric acid and 2 ml of hydrogen peroxide (30%). The samples were then digested in a microwave (type: MLS Start 1500). The cooled product was filtered off over a white-band filter and diluted with Millipore water up to 50 ml. The analyte was subsequently measured in an ICP-OES type Perkin Elmer Optima 8300 in combination with an SC-2 DX FAST Loop auto sampler. For calibration, a suitable single-element standard from Roth was used and sulfur was calibrated on the wavelengths 180.669, 181.975 and 189.965 by means of 4-point calibration.

When measuring the contents of sulfur with XRF an ANALYTICON XL3t-Air x-ray fluorescence gun in stationary lead-chamber operation were used. The spectrometer operated in the TestAllGeo correction mode for soil sampling.

The sulfur values determined with the elemental analysis were measured in an ELEMENTAR Vario Macro in CHNS mode with thermal conductivity detector. For each sample, 80-90 mg were weighed and analyzed by double determination. The calibration was carried out on a daily basis, taking into account the expected sulfur content and including a daily factor.

4.2.3. Gas analysis methods

Different kinds of analysis methods have been used to determine the fate of nitrogen and sulfur from the entrance to the exhaust within the system (see Figure 21).
To quantify potential NO_X emissions during the operation of the CLC pilot plant, both the FR and the AR exhaust gas were measured with an Eco Physics CLD 822 M hr chemiluminescence detector. Further the AR exhaust gas stream was continuously analyzed

with respect to CO, CO_2, O_2, NO, NO_2 and N_2O using a Rosemount NGA 2000 infrared gas analyzer including a paramagnetic analyzer for O_2.
The FR exhaust gas was also analyzed with a Rosemount NGA 2000 (CO: 0-100%, CO_2: 0-100%, O_2: 0-25%, H_2: 0-100%, CH_4: 0-100%, SO_2: 0-1000ppm) gas analysis. Additionally carbon species and determination of the N_2 content in the FR off gas was measured redundantly with an online gas chromatograph Perkin Elmer Arnel Clarus® 500. The AR off gas was analyzed with another Rosemount NGA 2000 (CO: 0-100%, CO_2: 0-100% and O_2: 0-25%).

The content of SO_2 in the FR was measured according to DIN EN ISO 14791. The detailed measuring method is described in relation to the used 120 kW CLC pilot plant by Mayer et al. [163].

The concentration of NH_3 in the FR was measured by wet chemical analysis according to VDI 3878 where NH_3 has been solved in 0.05 M H_2SO_4 as NH_4^+ ions. The NH_4^+ ions are detected by ion chromatography. The detailed measuring method is described by Wilk and Hofbauer [164].

During the operation of the CLC pilot plant, gas samples via gas sample bags were used to determine H_2S components both in the FR as well as in the AR. These gas samples were analysed using a gas chromatograph. The gas chromatograph was a Perkin Elmer Arnel Clarus® 500 with a flame photometric detector and a thermo conductivity detector.

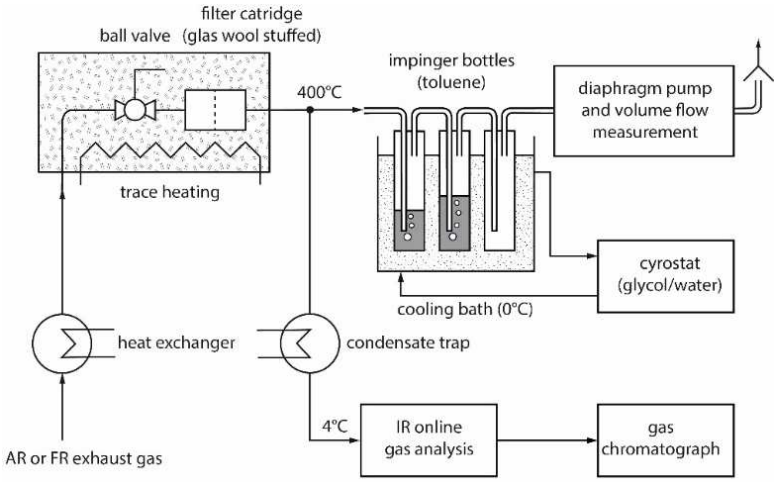

Figure 21: Exhaust gas analysis scheme

4.3. Used oxygen carriers

For the experimental work in the 120 kW pilot plant conducted in this thesis, two different synthetically produced OCs have been used, a $CaMn_{0,775}Mg_{0,1}Ti_{0,125}O_{3-\delta}$ based (C28) and a copper based (Cu15) OC.

4.3.1. The cooper based oxygen carrier Cu15

The copper based OC was prepared by impregnation of CuO on a highly porous Al_2O_3 support material. The material was originally developed by CSIC and underwent extensive testing in several pilot units [165, 166]. The batch used during the investigations was produced by Johnson Matthey using industrially relevant raw materials and production methods [71]. Although it is a CuO based OC, the OC is a so-called CLC OC according to the classification by Adánez et al. [57]. It is thus not able to release gaseous oxygen in the FR. At higher temperatures during the production process or during operation, the CuO interacts with the Al_2O_3 support and forms a $CuAl_2O_4$ spinel at temperatures between 800 and 1000 °C [167, 168] and the redox system then changes from CuO-Cu_2O to CuO-Cu. This loss of active CuO has no effect on the conversion capabilities of the OC but reduces the equilibrium partial pressure of O_2 and release of gaseous oxygen is not possible under common operating temperatures [169].

The composition of the fresh OC material used in the studies is shown in Table 5. The CuO content was determined by a PANalytical Axios Advanced wavelength dispersive X-ray fluorescence spectrometer. Excitation voltage was 50 kV, tube current 50 mA, a Rh tube was used and the measuring chamber stood under vacuum. The particle size distribution was measured by means of a laser diffraction technique with a Malvern Mastersizer 2000 and a Scirocco 2000 dry powder feeder. X-ray powder diffraction was collected by a PANalytical MPD Pro X-ray powder diffractometer equipped with an X-ray source with a Cu anode and a PIXCel 3D semiconductor detector.

Table 5: Physical and chemical properties of the fresh Cu15 OC

Parameter	Value
XRD main phases	CuO, γ-Al_2O_3
Total CuO content [wt%]	23
Mean particle size [µm]	153
Bulk density [kg/m³]	841

4.3.1.1. General remarks about operation with the Cu15 OC in the 120 kW pilot plant

The fresh copper material used in these investigations shows a significant loss of CuO at the beginning of CLC operation. During the first five hours of operation the amount of CuO on

the particles goes down from about 23 wt% to about 16 wt%. Within these first hours, the methane conversion and carbon dioxide yield are noticeably elevated compared to the steady state operation afterwards. This behavior could be reproduced in several experiments. Figure 22 shows the active CuO content of the OC material depended upon the operation time.

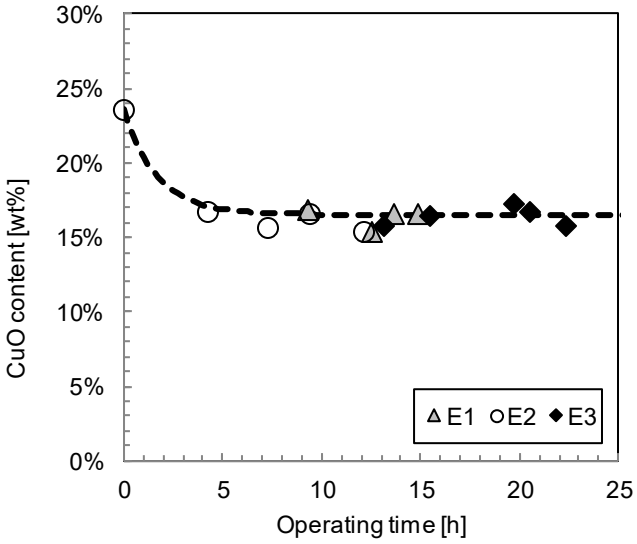

Figure 22: Active copper content of Cu oxygen carrier (E1: Experiment 1; E2: Experiment 2; E3: Experiment 3)

Based on the knowledge all following experiments were conducted at steady conditions after this first few hours.

To investigate the decrease of the copper content during the first hours of operation, fresh and used OC material from the same batch were compared with each other. Figure 23 representing solid samples of the fresh oxygen carrier (left) compared to collected samples out of the LLS after 15.5 hours of operation (right).

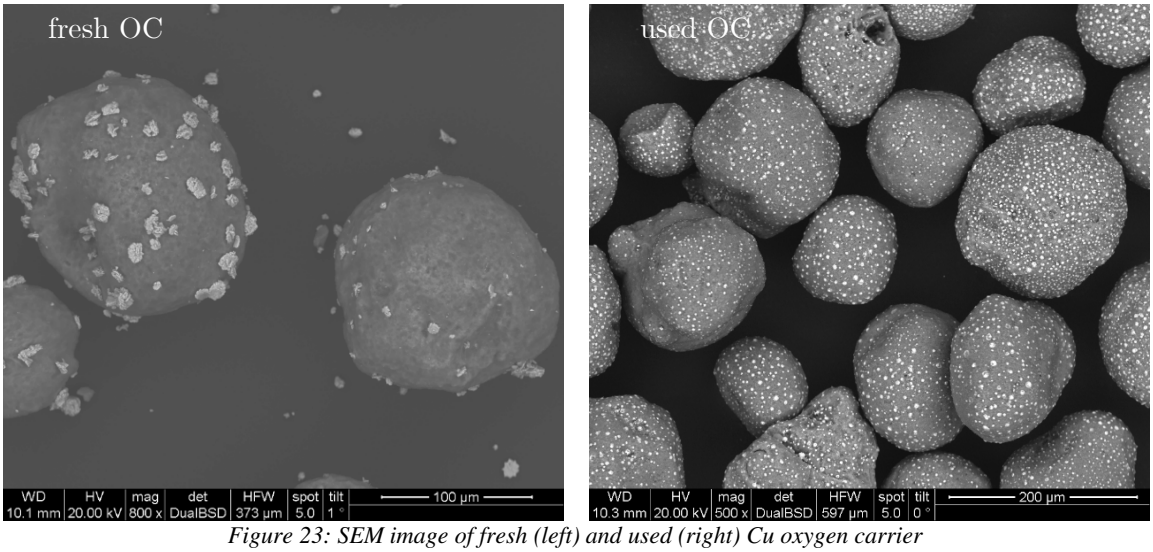

Figure 23: SEM image of fresh (left) and used (right) Cu oxygen carrier

The applied copper forms flakes on the surface of the γ-Al_2O_3 support material. These concentrated areas of copper protrude from the subjacent surface. Thereby some of the impregnated flakes are very loose connected to the aluminum oxide. Compared to the right image, after almost 16 hours of operation, the copper impregnation was relocated and well dispersed on the surface (white spots). It is assumed that the extended loss of CuO in the first few hours of operation is generated by the mechanical stress on the particles, such as intergranular friction or crushing actions.

However, when looking on cross-section images of the fresh and used material this relocation process becomes clearer (Figures 6 and 7). During operation under CLC conditions in the 120 kW pilot plant the superficial Cu flakes are diffusing into the Al_2O_3 material. This effect will cause an additional reduction of the active copper content, which is responsible for the oxygen transportation process. According to the circulation rate of the OC in both the oxidizing air reactor and reducing fuel reactor the retention time is being influenced and coincidently the amount of oxygen which can be adsorbed.

Figure 24 and Figure 25 representing SEM images of OC material samples embedded in epoxy, cross-sectioned and polished. Both right images are showing copper highlighted by energy dispersive X-ray spectroscopy, colored in yellow. The higher the Cu concentration in the sample is, the stronger the tone of yellow.

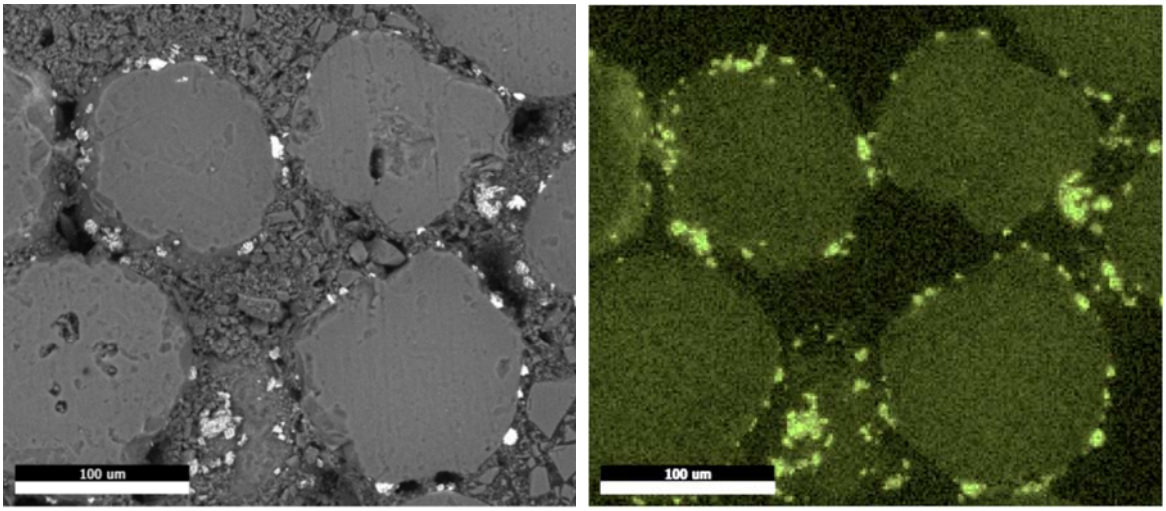

Figure 24: Cross-sectional SEM images of the fresh OC and overlayed Cu EDS signal (yellow)

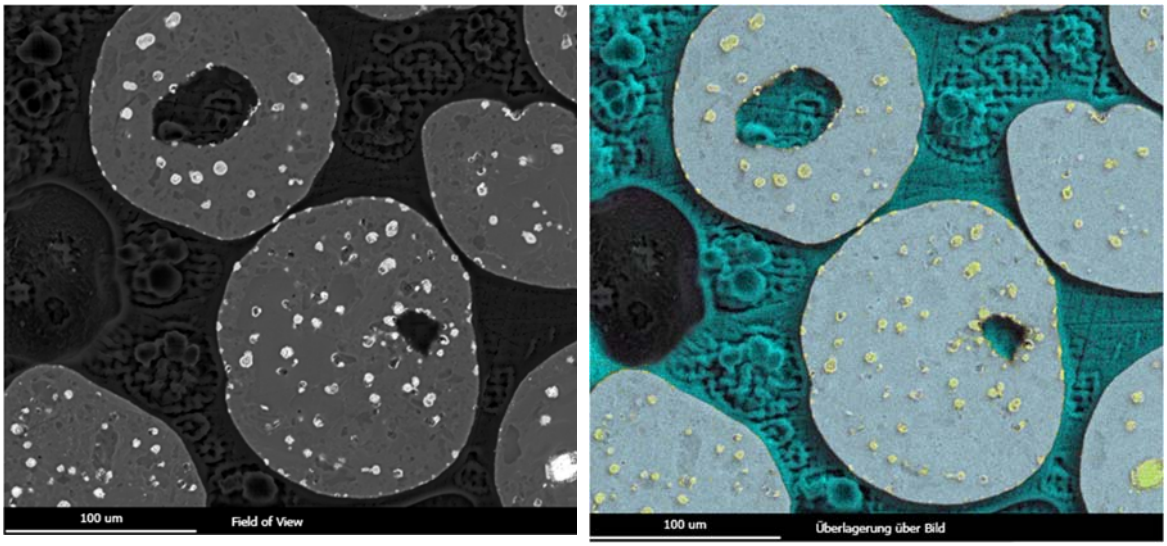

Figure 25: Cross-sectional SEM images of the used OC and overlayed Cu EDS signal (yellow)

4.3.2. The perovskite oxygen carrier C28

The $CaMn_{0,775}Mg_{0,1}Ti_{0,125}O_{3-\delta}$ based OC, called C28, was originally developed by Chalmers University of Technology and VITO [170]. Production of the OC was scaled up using industrially available raw materials and infrastructure during the EU funded project SUCCESS [171]. The batch used for this study was produced by Euro Support Advanced Materials by spray drying and calcination using industrially relevant raw materials and production methods [172]. Perovskite based oxygen carriers release oxygen under reducing conditions with low oxygen partial pressure and therefore allow chemical looping with oxygen uncoupling (CLOU). The kinetics of C28 have been investigated by Abad et al. [173].

The composition of the fresh OC material used during the investigations is shown in Table 5. The particle size distribution was measured by means of a laser diffraction technique with a Malvern Mastersizer 2000. The formed crystalline phases were analysed by X-ray powder diffraction (XRD) using a Philips X'Pert diffractometer with PANalytical X'Pert Pro software.

Table 6: Physical and chemical properties of the fresh C28 OC

Parameter	Value
XRD main phases	$Ca((Mn_{0.9}Ti_{0.1})O_{2.961}$, MgO, $CaMn_2O_4$
Mean particle size [µm]	139
Bulk density [kg/m³]	1780

Chapter Five

5. Fate of fuel contaminants

5.1. Benchmark parameters

For comparison of process performance and operating conditions, different parameters are used. The methane conversion X_{CH_4}, indicates how much of the CH_4 entering the FR is converted to CO_2, CO and H_2. The H_2S conversion X_{H2S} and NH_3 conversion X_{NH3} quantifies how much of the sulfur or ammonia fed to the FR reacts to SO_2 respectively to N_2 or NO_X:

$$X_i = 1 - \frac{\dot{n}_{FR,exh} * y_{i,FR,exh}}{\dot{n}_{FR,feed} * y_{i,FR,feed}} \qquad i=CH_4,\ NH_3,\ H_2S \tag{22}$$

Where $\dot{n}_i$ is the molar flow and y_i is the molar concentration of species i either CH_4, NH_3 or H_2S. To quantify the conversion of carbon into CO_2 the carbon dioxide yield γ_{CO_2} is used. This is an important parameter for carbon capture and storage (CCS):

$$\gamma_{CO_2} = \frac{\dot{n}_{CO_2,FR,exh}}{\dot{n}_{C,FR,feed}} \tag{23}$$

The air to fuel ratio λ describes the ratio of the actually supplied amount of oxygen to the AR, to the stoichiometric required oxygen for full fuel conversion:

$$\lambda = \frac{\dot{m}_{O_2,AR\ feed}}{\dot{m}_{O_2,FR\ Stoichiometric}} \tag{24}$$

Where is $\dot{m}_{O_2,AR\ feed}$ the mass flow of oxygen fed to the system via the AR and $\dot{m}_{O_2,FR\ Stoichiometric}$ is the stoichiometric mass flow of oxygen necessary for full combustion.

5.2. Path of nitrogen

A modified version of this chapter has been submitted to Energy as :
Robert F. Pachler, Stefan Penthor, Karl Mayer, Hermann Hofbauer
Investigation of the fate of nitrogen in chemical looping combustion of gaseous fuels using two different oxygen carriers

5.2.1. CLC operating conditions

In order to determine the fate of nitrogen, the NH_3 concentration in the fuel feed was varied, whereas all other process parameters (p, T, circulation rate, fluidization, etc.) were kept as constant as possible. The operating conditions of the 120kW CLC unit with the two different OC including the air-to-fuel ratio λ, the fuel power P_{th}, the FR temperature T_{FR}, the OC inventory m_{total} and the concentrations of NH_3 in the fuel feed are represented in Table 7. When only NH_3 is taken into account (i.e., N_2 from natural gas does not add up to fuel nitrogen), this corresponds to fuel nitrogen contents between 0 and 1.4 wt % related to the total fuel feed (Table 8). The operating temperature was, depending on the OC used, around 955°C in the FR for the perovskite type (C28) and 805 °C in the FR for the copper based OC (Cu15) according to the manufacturer. Previous tests showed, that the cooper-based OC performed best at around 800°C in the FR and OC to fuel ratios above 1.4. When further increasing the temperature from 800 to 900°C, the particle lifetime decreased from 2700 to 1100 hours [66, 174]. When using the perovskite type OC, the only limit was the melting point of the reactor material.

Table 7: Operating conditions with nitrogen impurities

Parameter	Unit	C28	Cu15
P_{th}	[kW]	64 ± 1	70 ± 1
T_{FR}	[°C]	955 ± 1	805 ± 2
λ	[-]	1.3	1.5
m_{tot}	[kg]	50	40
x_{N_feed}	[wt%]	0.4 - 0.6	0.4 - 1.4
operating point	[-]	OP1-5	OP6-10

Table 8: Operating points with corresponding OC, nitrogen concentration and sampling position

OP [-]	OC [-]	$x_{N\ feed}$ [wt%]	$y_{NH3\ feed}$ [Nl/h]
1	C28	0	0
2	C28	0.44	33
3	C28	0.63	48
4	C28	0.52	40
5	C28	0	0
6	Cu15	0	0
7	Cu15	0.38	32
8	Cu15	0.71	59
9	Cu15	1.40	115
10	Cu15	0	0

5.2.2. Effect on fuel conversion

The operating conditions were chosen based on operational experience with the two OC materials without NH_3. High, but not full fuel conversion (X_{CH4}, γ_{CO2}) was desired, in order to observe changes in performance. Figure 38 shows the overall performance of the 120 kW_{th} CLC pilot plant for two different OC and various concentrations of NH_3 in the fuel feed.

The course of reactivity of the oxygen carriers, expressed by the CH_4 conversion and CO_2 yield, shows a similar behavior. With both oxygen carriers, the decrease of performance is attributed to the loss of bed material. (Figure 26).
Each symbol in the diagram stands for a validated operating point. Stable operation of the pilot plant was possible, even with high nitrogen concentrations in the fuel feed. During the experiments, fresh OC material has been used and added as makeup when the amount of total active inventory decreased over 20% from the initial amount.

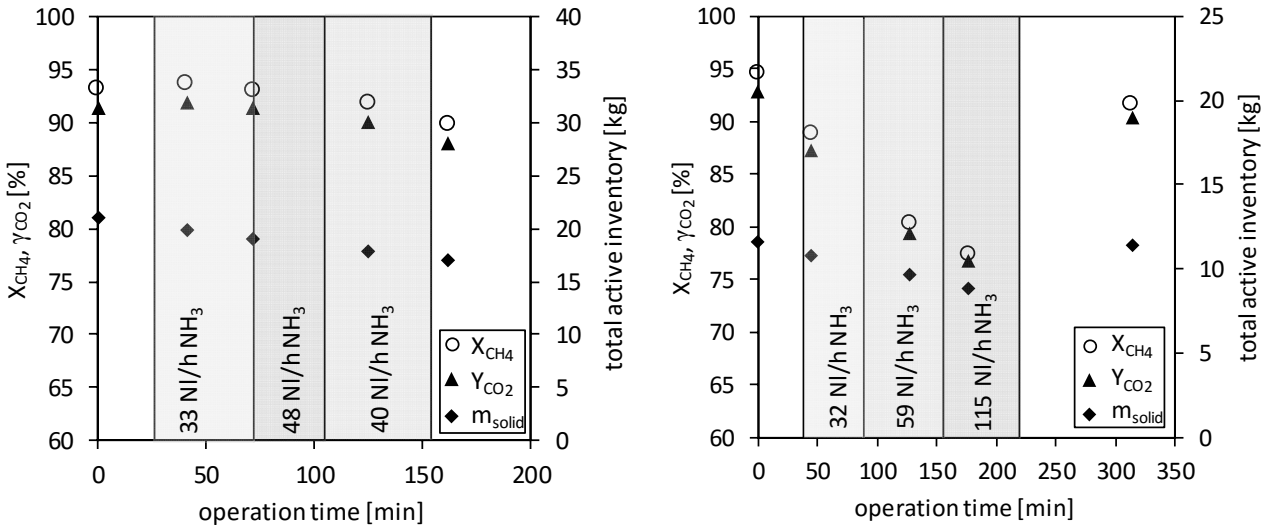

Figure 26: CH4 conversion and CO2 yield before, during and after NH3 in the FR feed, left with C28 and right with Cu15 as OC

With C28 as OC no improvement, neither in CH_4 conversion nor in CO_2 yield could be observed when switching off the NH_3 supply.

In Figure 27, CH_4 conversion and CO_2 yield as a function of increasing N content in the fuel feed are shown. When using the C28 OC, the CH_4 conversion as well as the CO_2 yield stayed almost constant. However, when using Cu15 as OC both the CH_4 conversion and CO_2 yield reacted very sensitive to changes in the total active inventory. But even with increasing fuel N-content, the performance decrease has been similar to previous results of experiments without nitrogen in the fuel feed and the same OC.

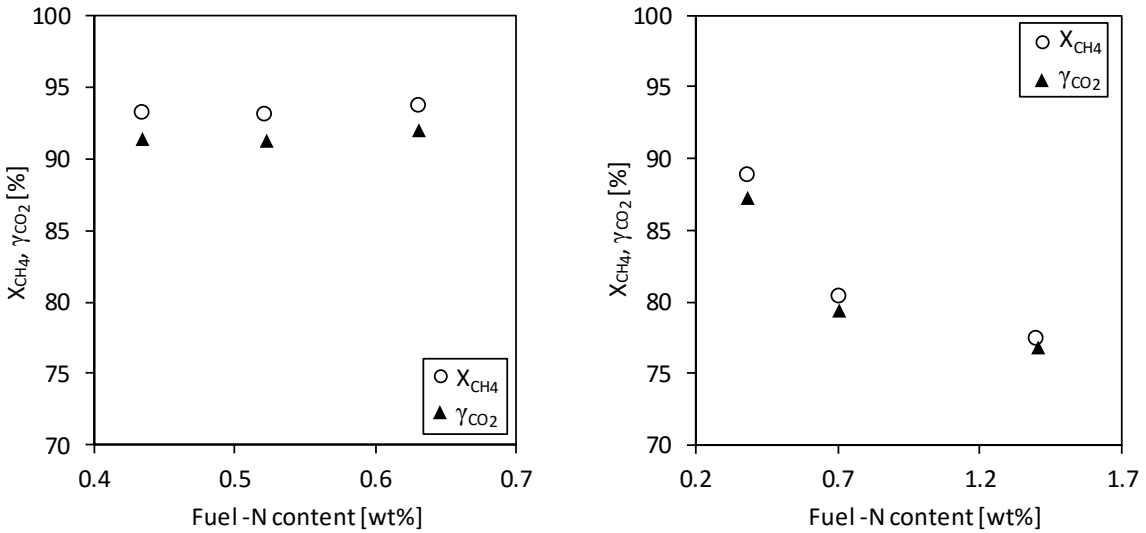

Figure 27: CH4 conversion and CO2 yield as a function of increasing N content in the fuel feed, left with C28 and right with Cu15 as OC

Figure 28 shows the FR flue gas composition before (OP1/OP6), during (OP3/OP9) and after (OP5/OP10) operation with NH_3. With C28, the FR flue gas composition stayed almost constant (OP1 to OP3). The amount of CH_4 increased and the amount of CO_2 decreased at OP5 due to the loss of active inventory in the reactor system. As mentioned before, the total active inventory has an influence on the overall performance and thereby on the flue gas composition.

Similar but significantly amplified, when using Cu15 as OC, the CH_4 conversion and CO_2 yield decreased at the same time due to the loss of bed inventory (OP9). This results in a larger amount of CH_4 and a smaller amount of CO_2 in the FR exhaust gas stream. Further, a higher amount of hydrogen was measured in the flue gas during operation with 1.4 wt% N in the fuel feed. After switching off the ammonia supply, a fast regeneration could be observed (OP10). It has to be mentioned, that the regeneration effect is superimposed with a makeup of new bed material due to excessive deviation from the initial conditions (see Figure 26 right diagram). Therefore a causal relationship cannot be confirmed.

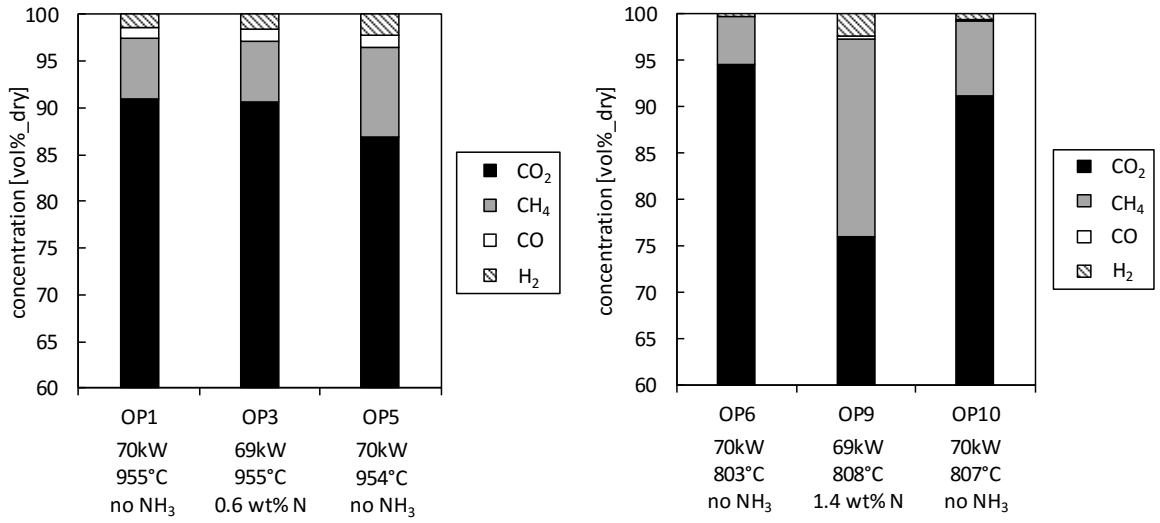

Figure 28: FR flue gas composition in subject to the nitrogen fuel feed and temperature, left with C28 and right with Cu15 as OC

5.2.3. Effect on emissions

Figure 29 shows the nitrogen emissions in the FR exhaust gas in form of NO_X and NH_3. The measured concentration of NH_3 was a result of gas slip through the FR. Values for NH_3 conversion have been calculated on the basis of the measured NH_3 concentration in the FR exhaust gas. When using the perovskite type C28 OC, only around 72 percent of the fed ammonia were converted (71-74.5%) in the FR. Further, NO_X emissions in form of NO are clearly increased and related to the amount of N in the fuel feed. Due to the high NO_X concentration (beyond 1000ppm NO = limit of analysis) in the FR at OP4, the amount of NH_3 was decreased again from 48 Nl/h (OP3) to 40 Nl/h (OP4). With Cu15 as OC the conversion of NH_3 has been nearly complete (>99.8%) for all operating points and no NO_X emissions occurred in the FR exhaust gas.

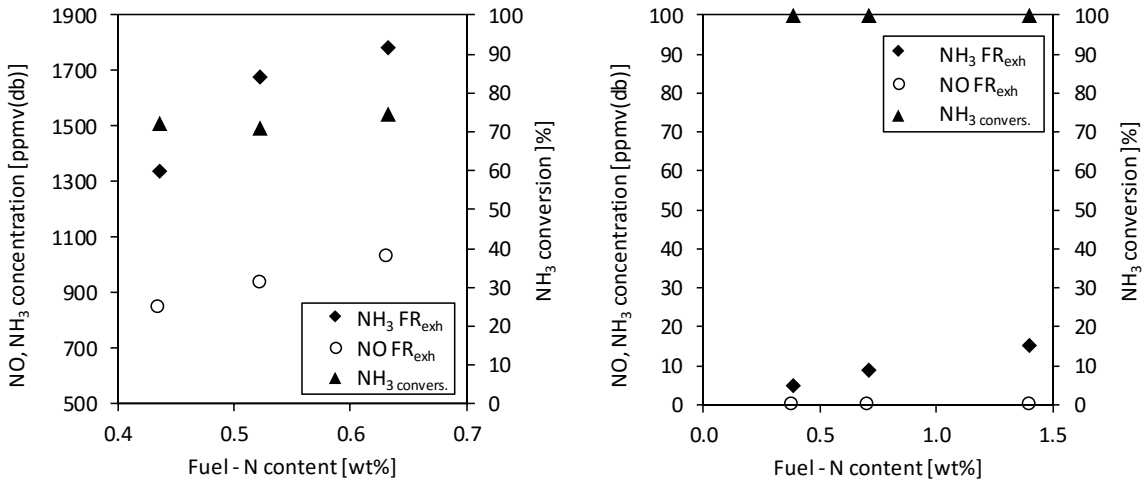

Figure 29: Effect of increasing N content in the fuel feed on NH3 conversion and NH3 and NO concentrations in FR exhaust gas, left with C28 and right with Cu15 as OC

Figure 30 shows the NH_3 conversions of all operating points with ammonia in the fuel feed and gives an overview of the different behavior of the two tested oxygen carriers. Operating points 2 to 4 are with C28 as OC and OP7 to OP9 are with Cu15 as OC.

During all experiments with ammonia, neither the wet chemical analysis according to VDI 3878 nor the online Rosemount NGA 2000 or CLD analysis showed any traces of NO_X leaving the AR. Only in the FR exhaust gas stream NO_X and NH_3 could be detected.

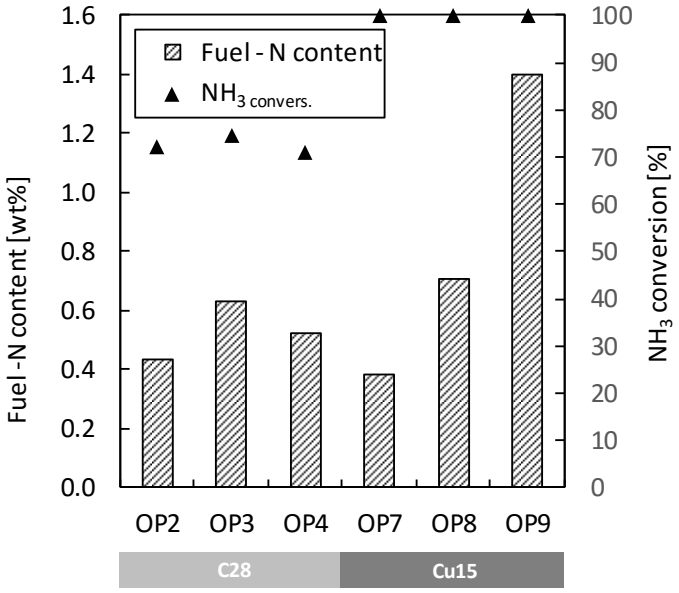

Figure 30: NH_3 conversion at various Fuel-N-contents in the FR feed (OP: Operating point)

With the CLOU OC (C28) the conversion of the introduced NH_3 was low, in contrast the fuel conversion and CO_2 yield remained unaffected from fuel N. Vice versa when using the

CLC OC (Cu15), where the CH_4 conversion and CO_2 yield have been unaffected from the presence of NH_3 and as the NH_3 conversion have been almost complete.

Based on these measurements, Figure 31 - Figure 32 show the mass balance for nitrogen components for AR and FR at two operating points. Due to the much larger amount of nitrogen entering the AR via the combustion air, the scaling for the two reactors is different. With Figure 31, it becomes obvious that with C28 as OC approximately one third of the introduced NH_3 slips through the FR, a small amount reacts to NO and the large part of the introduced NH_3 reduced to N_2.

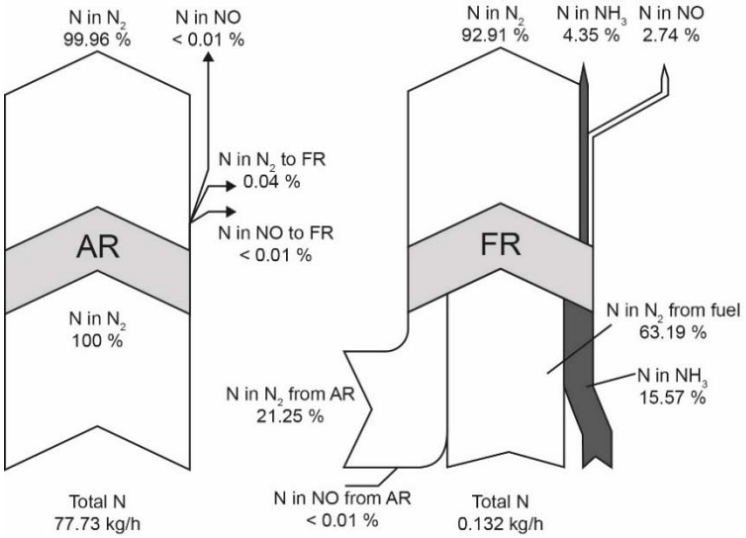

Figure 31: Mass balance for nitrogen components for both reactors (N content fuel of 0.44 wt %) with C28 as OC. Scaling for AR and FR is different. (OP2)

The picture is different for the Cu15 OC (Figure 32), where the largest amount of nitrogen in the FR exhaust gas comes from the gas leakage from the AR to FR via the upper loop seal and nearly the complete introduced NH_3 is reduced to N_2.

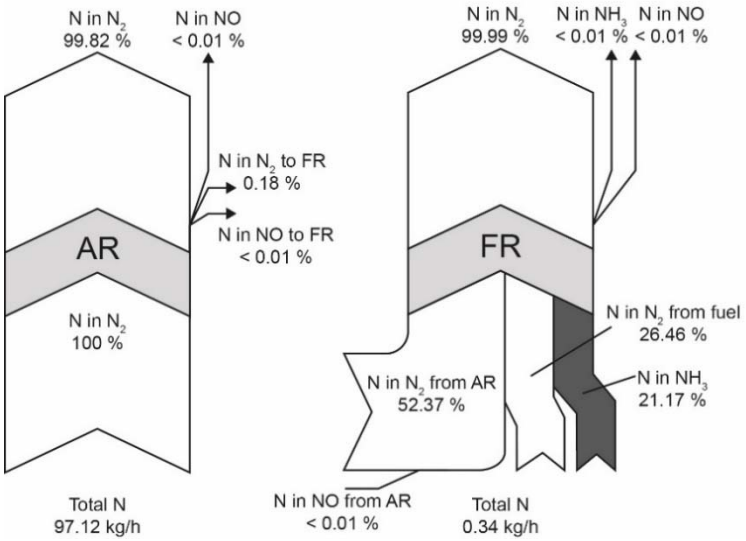

Figure 32: Mass balance for nitrogen components for both reactors (N content fuel of 1.4 wt %) with Cu15 as OC. Scaling for AR and FR is different. (OP9)

5.3. Path of sulfur

This chapter is a modification of:

Robert F. Pachler, Stefan Penthor, Karl Mayer, Hermann Hofbauer
Fate of sulfur in chemical looping combustion of gaseous fuels using a Perovskite oxygen carrier
Fuel, 241 (2019) 432-441
DOI: 10.1016/j.fuel.2018.12.054

Robert F. Pachler, Karl Mayer, Stefan Penthor, Mario Kollerits, Hermann Hofbauer
Fate of sulfur in chemical looping combustion of gaseous fuels using a copper-based oxygen carrier
International Journal of Greenhouse Gas Control, 71 (2018) 86–94
DOI: 10.1016/j.ijggc.2018.02.006

5.3.1. CLC operating conditions

To characterize the fate of sulfur, the operating conditions of the CLC system were kept constant for all investigated sulfur concentrations. The operating conditions are summarized in Table 9 including the air-to-fuel ratio λ, the fuel power P_{th}, the FR temperature T_{FR}, the OC inventory m_{total} and the concentration of H_2S in the fuel feed.

Table 9: Operating conditions with sulfur impurities

Parameter	Unit	C28	Cu15
P_{th}	[kW]	62 ± 2	73 ± 0.2
T_{FR}	[°C]	953 ± 1	800 ± 4 (850)*
λ	[-]	1.85	1.5
m_{tot}	[kg]	64	40
y_{H2S_feed}	[ppmv]	100 - 3000	500 - 2000
operating point	[-]	OP1-7	OP8-17

* with Cu15 as OC one operational point have been conducted with increased FR temperature (850°C).

Due to the different behavior of the two different OCs to sulfurous fuel impurities and the resulting other investigations and analysis, the results are presented in separate chapters.

5.3.2. Performance of the perovskite oxygen carrier

5.3.2.1. Effect on particles

To investigate the accumulation of sulfur on the OC material during operation, samples were compared with each other before and after H_2S was added to the fuel feed.

Figure 33 to Figure 35 represent SEM images of OC material samples embedded in epoxy, cross-sectioned and polished. All right images are showing sulfur highlighted by energy dispersive X-ray spectroscopy (EDS), colored in magenta. The higher the sulfur concentration in the sample is, the stronger the tone of magenta.

Figure 33 shows solid samples of the oxygen carrier out of the ULS without fuel impurities in the fuel feed.

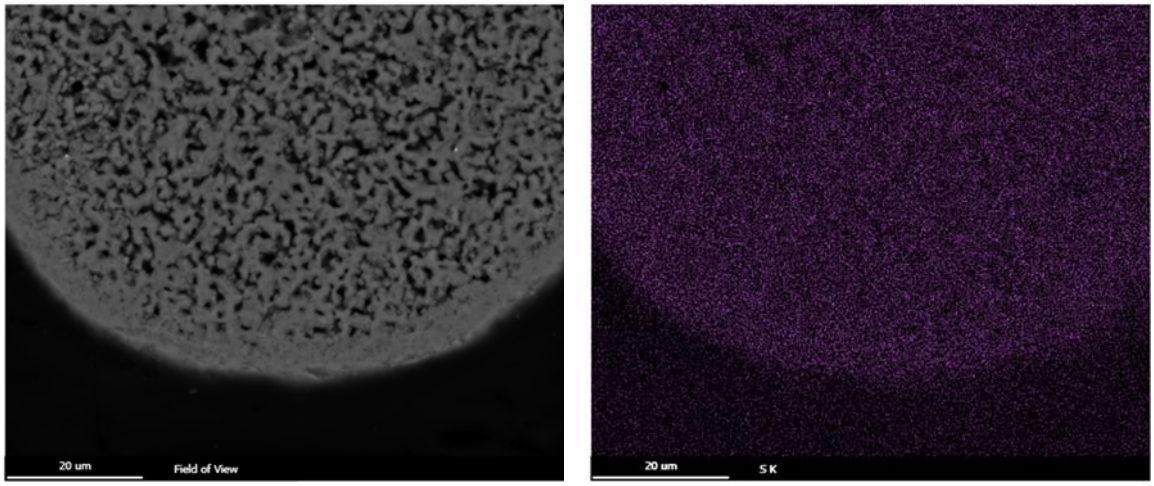

Figure 33: SEM image of the unpolluted perovskite oxygen carrier with sulfur EDS signal (magenta) on the right

When looking at cross-section images of the unpolluted material there are no traces of sulfur visible. Even when the signal amplification was drastically increased, only a signal noise could be detected. Compared to collected samples (Figure 34 and Figure 35) taken out of the upper loop seal (ULS), after 5.5 hours of operation under CLC conditions in the 120 kW pilot plant with up to 3000 ppmv H_2S in the fuel feed, a significant amount of sulfur could be measured (Figure 36). As can be seen in Figure 35 the sulfur forms a deposited layer on the surface of the oxygen carrier particles. This effect will cause a reduction of the active surface area, which leads to a worsening of the overall performance. Due to the fact that sulfur is very inhomogeneous dispersed on the particle surface a quantitative element analysis was not possible.

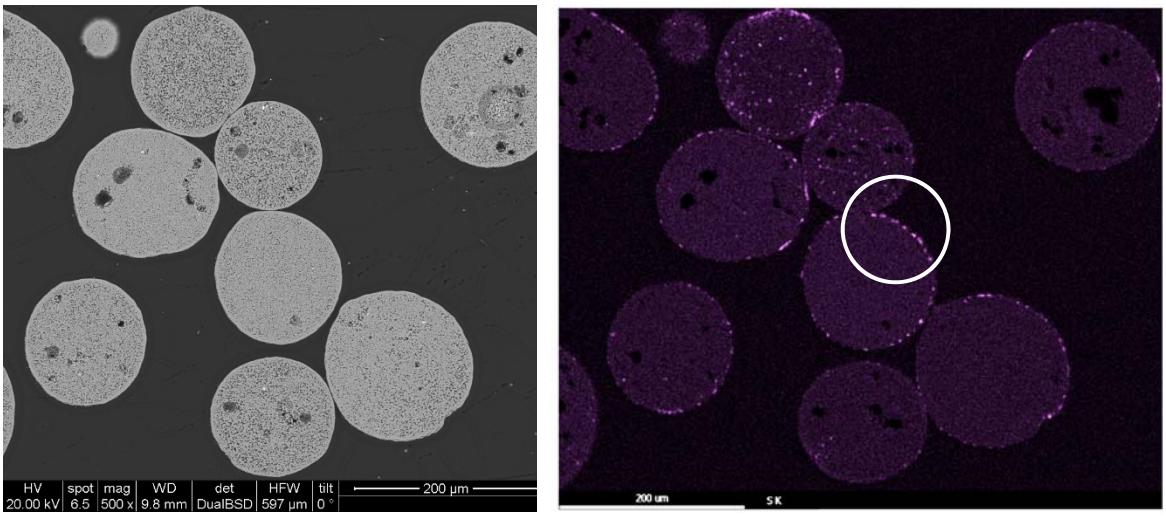

Figure 34: Cross-sectional SEM images of the used OC with sulfur EDS signal (magenta) on the right. Position of Figure 25 is marked with a circle.

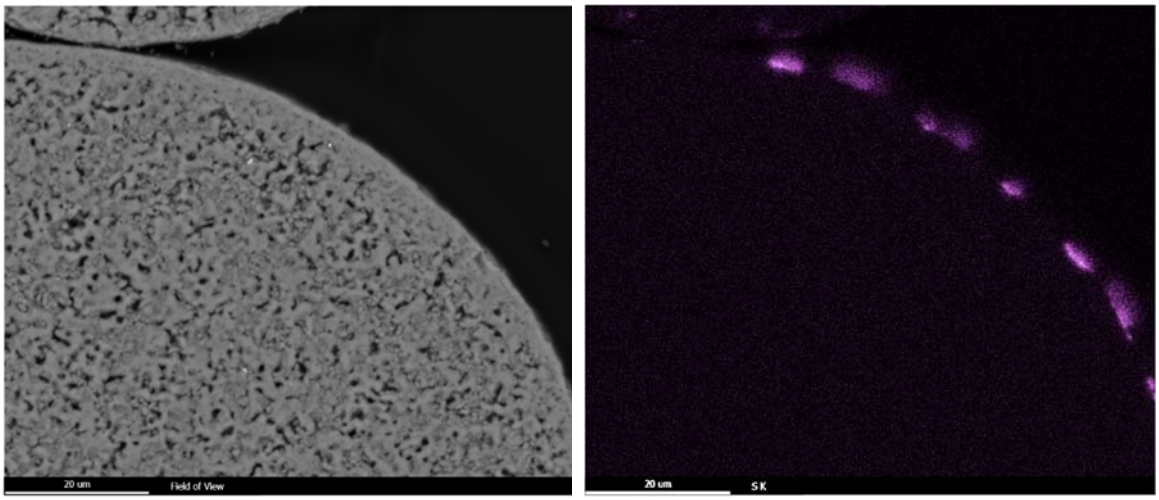

Figure 35: Cross-sectional SEM images of the used OC with sulfur EDS signal (magenta) on the right in detail

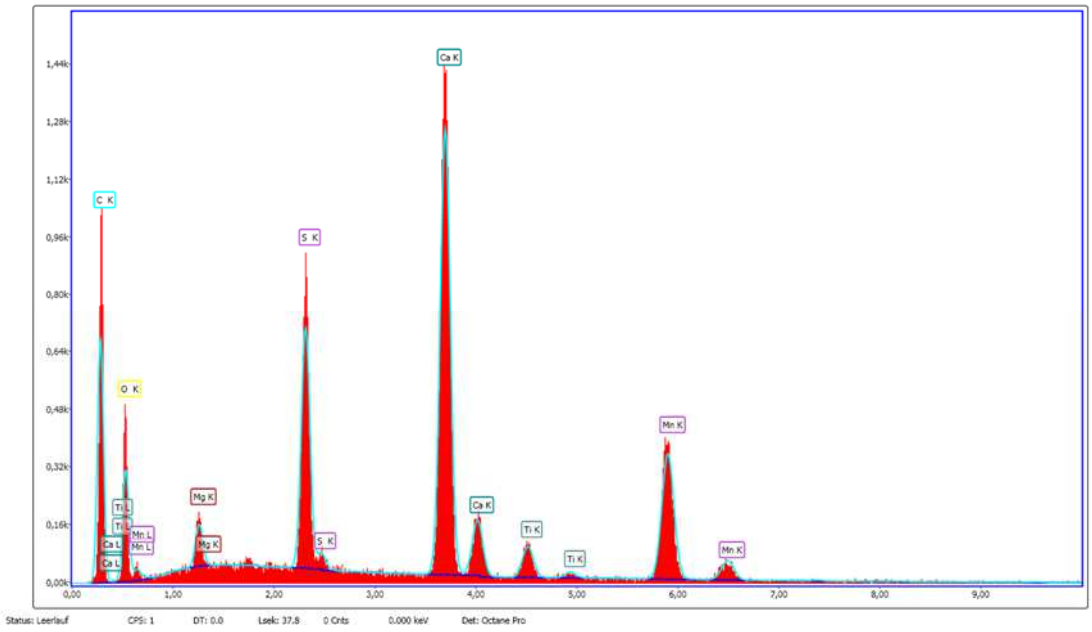

Figure 36: SEM element analysis

5.3.2.2. Effect on fuel conversion

Figure 37 shows online data of the overall performance of the 120 kW_{th} CLC pilot plant for five different concentrations of H_2S in the fuel feed at 950°C in the FR and 62 kW_{th} fuel power from one of the experiments.

The experiments with sulfur in the fuel feed have been started after more than 3.5 h (220 min) of operation at 950°C without any impurities and only natural gas in the fuel reactor. After 20min of operation with 100 ppmv H_2S in the fuel feed the CO_2 yield started to decrease. To investigate further effects, the H_2S dosing had been gradually increased up to 3000 ppmv (see dashed vertical lines in Figure 37). When increasing from 100 to 500 ppmv, an drop of CO_2 yield and an increase of CO in the FR were observed. With a little delay, the online gas analytic detected SO_2 emission in the FR exhaust gas. The lag of response was attributed to the saturation time of SO_2 in the upstream of the gas analysis located condensate trap (see Figure 21). This results in a reduced SO_2 concentrations in the FR exhaust gas measured by the gas analysis equipment. During the experiments the total active inventory in the pilot plant kept constant between 20 and 22 kg with a slightly decreasing tendency. Due to the fact that small amounts of material are permanently elutriated, at around 170 min 1 kg of OC have been added because of the deviation to the initial conditions. The fresh material caused a short stagnation in the CO_2 yield trend, but a few minutes later started to decrease again with the same gradient as before. The decrease of CO_2 yield correlates with the loss of active bed inventory.

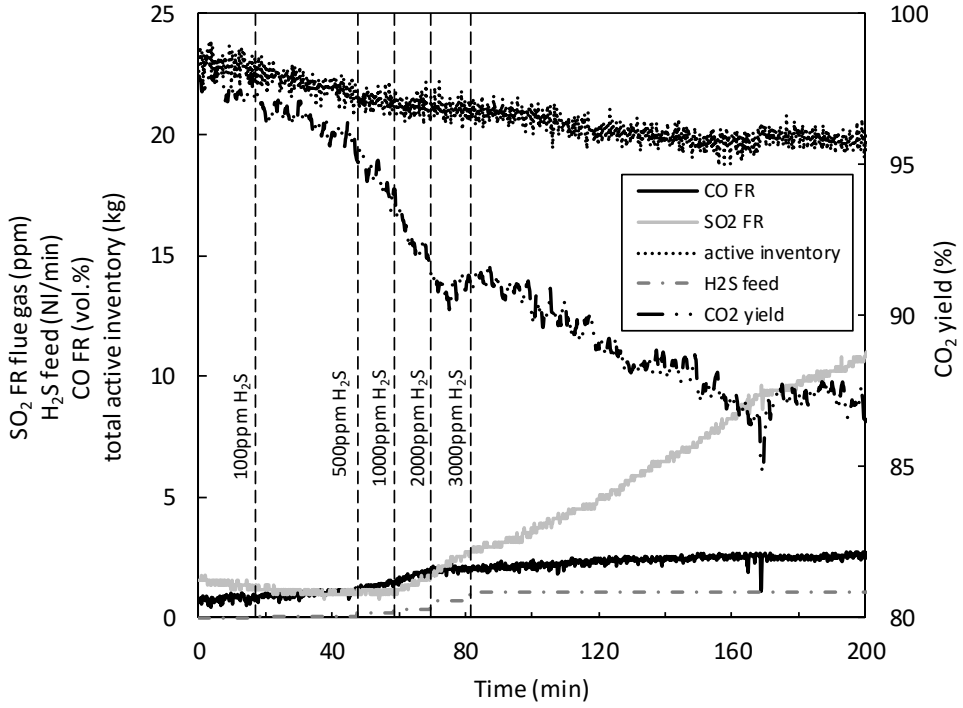

Figure 37: Online data composition of overall CLC performance with various S content in the FR feed

The course of reactivity of the oxygen carrier, expressed by the CH_4 conversion and CO_2 yield, decreased continuously during the presence of sulfur in the fuel feed (see Figure 38). For a better readability, the gradual increase of H_2S (100-3000 ppm) is omitted. Each symbol in the diagram stands for a validated operating point. Even with small quantities of H_2S in the fuel feed (100ppmv) the worsening of the reactivity could be observed. Unlike to experiments with other materials tested in this unit [67], the CH_4 conversion decreased continuously without reaching a steady state. Stable operation of the pilot plant was possible, even with high sulfur concentrations (3000ppmv) in the fuel feed. After switching off the H_2S supply, no immediate improvement in the CH_4 conversion became apparent (operating point at 330 minutes). Even after two hours of operation without sulfur in the fuel feed, SO_2 emissions could be still detected in the FR exhaust gas, which leads to the assumption that sulfur is accumulated on the particles and can be released again after time.

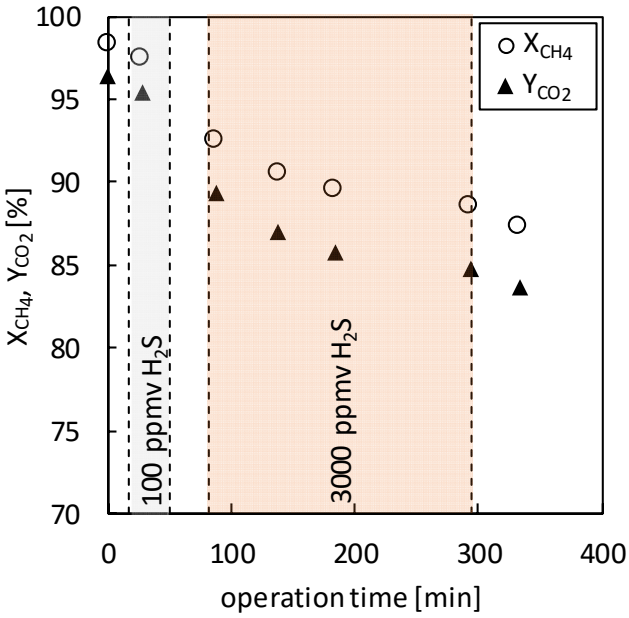

Figure 38: CH_4 conversion at 100 and 3 000 ppmv H_2S in the FR feed

Figure 39 shows the FR flue gas composition before (OP1), during (OP6, maximum sulfur feed) and after (OP7) operation with sulfur. Due to the presence of sulfur, the CH_4 conversion and CO_2 yield decreased. This results in a larger amount of CH_4 and a smaller amount of CO_2 in the FR exhaust gas stream. Further a higher amount of hydrogen was measured in the flue gas during operation with 3000 ppmv H_2S in the fuel feed. After switching off the sulfur supply, no significant regeneration could be observed.

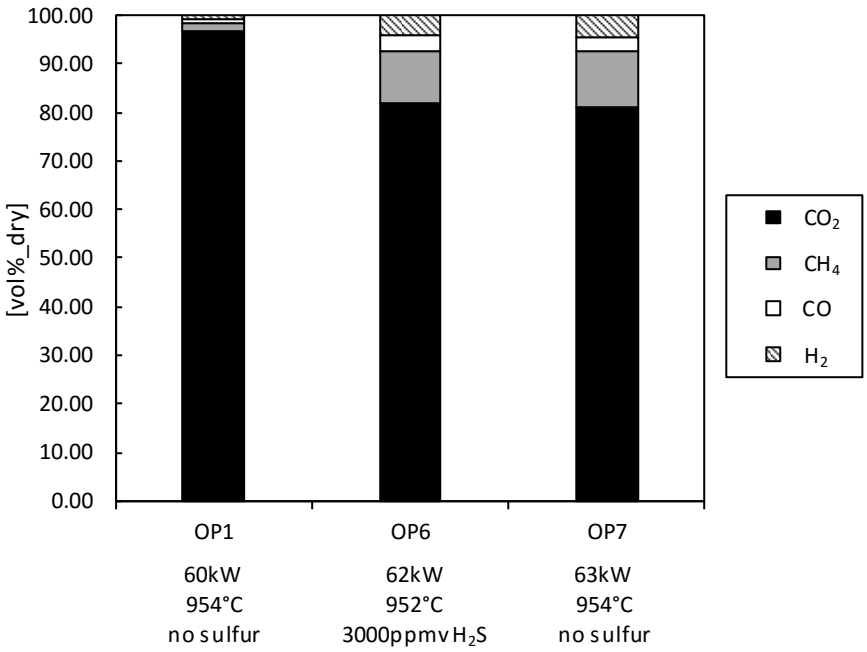

Figure 39: FR flue gas composition in subject to the sulfur fuel feed and temperature

Figure 40 shows the degree of oxidation (X_S) of the Perovskite oxygen carrier used in the 120 kWth CLC pilot plant. For a better readability, the gradual increase of H_2S is omitted.

Even though sulfur accumulation on the particle surface could be determined, the degree of oxidation in both, ULS and LLS, was not significantly affected by the sulfur.

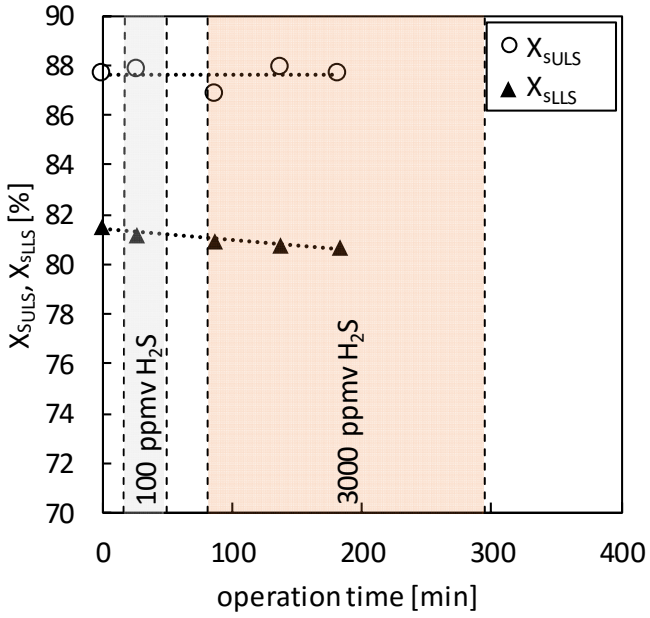

Figure 40: Effect of sulfur in the fuel feed on degree of oxidation in the ULS and LLS over time

Figure 41 represent the CH4 conversion as a function of the sulfur loading on the particle. Thereby three different measuring methods Inductively Coupled Plasma - Mass Spectrometry (ICP), X-ray fluorescence spectroscopy (XRF) and elemental analysis (CHNS) have been used. Although all three methods are showing the same behavior, the differences in the absolute amounts are partially significant (Figure 41). Due to the fact, that the amount of sulfur on the particles is very close to the lower detection limit of the CHNS analysis, this leads to irregularities. The difference between the two other methods (ICP, XRF) is most likely a combination of sampling errors and owed to the fact that the light element sulfur is hard to detect in the perovskite matrix. As shown in Figure 24 the sulfur is very inhomogeneous dispersed on the particle surface. This fact was taken into account during the sampling procedure but it seems that the homogenization was insufficient and needs to be improved in future experiments. All measurement methods are showing the same trend, a decrease of conversion with increasing sulfur loading. In order to not affect the readability negatively, the CO_2 yields are not included in the figure, which are shown in Table 10, for results obtained via XRF. CH4 conversion and CO_2 – yield are both decreasing with increasing sulfur loading. However, the difference between the two parameters, which is an indicator for unconverted CO in the FR exhaust gas, increases. Thus, conversion of CO becomes worse with increasing sulfur loading.

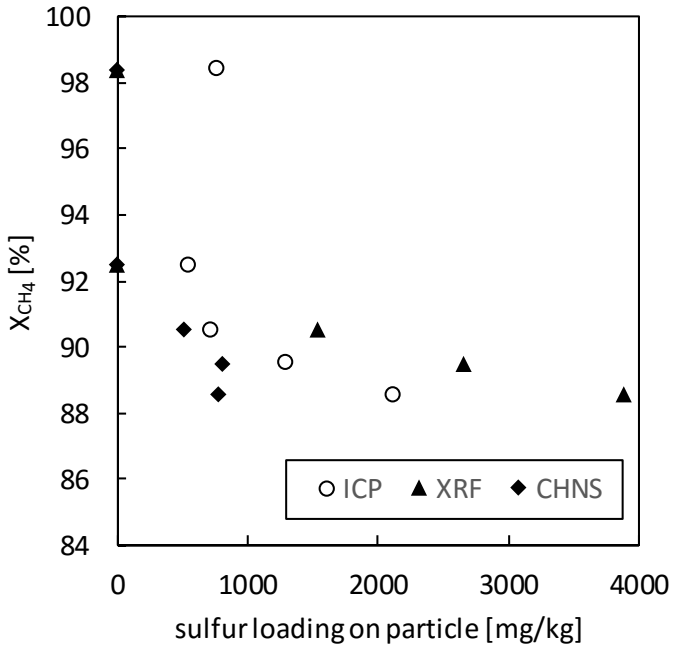

Figure 41: CH4 conversion as a function of sulfur loading on the particles measured with ICP, RFA and CHNS

Table 10: : CO_2 yield and CH_4 conversion in dependence of sulfur loading on particle measured with ICP, XRF, CHNS and accumulated sulfur feed

Sample	sulfur loading [mg/kg]			Accumulated sulfur feed	X_{CH4}	γ_{CO2}	X_{CH4} - γ_{CO2}
	ICP	XRF	CHNS	[g]	[%]	[%]	[%]
OP1; ULS	766	BDL	BDL	0	98.38	96.46	1.92
OP3; ULS	551	BDL	BDL	20.4	92.48	89.37	3.11
OP4; ULS	715	1540	509	37.9	90.52	86.97	3.55
OP5; ULS	1302	2662	808	80.6	89.51	85.79	3.72
OP6; ULS	2124	3889	782	96.1	88.56	84.79	3.77

BDL...below detection limit

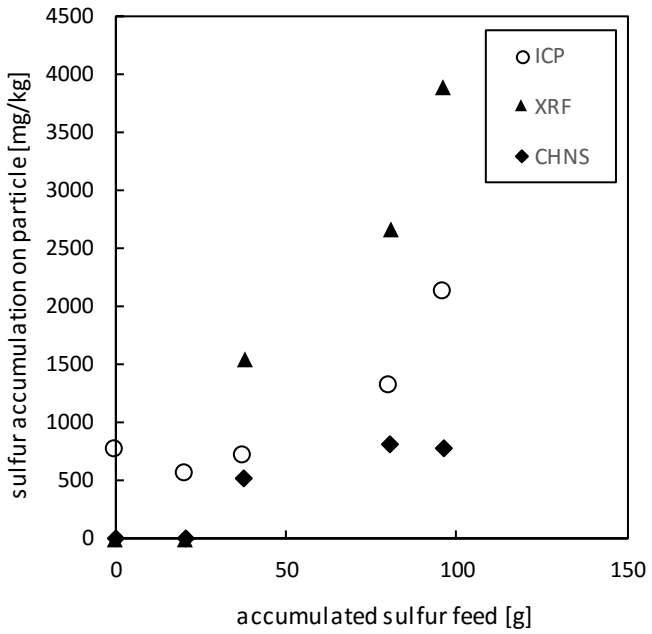

Figure 42: Sulfur accumulation on particle as a function of sulfur feed to the FR

5.3.2.3. Effect on emission

In Figure 43, the H_2S conversion for operation with sulfurous fuel feed is shown. During all experiments no H_2S slip was observed, therefore, the H_2S conversion was about 100%.

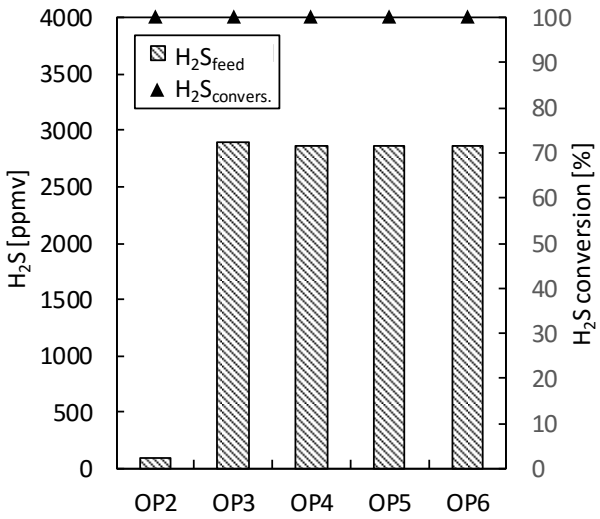

Figure 43: H_2S conversion at 100 and ~3000 ppmv H_2S in the FR feed with C28 as OC (OP: Operating point)

To observe the fate of sulfur in the CLC process, H_2S and SO_2 emissions were measured during the operation with the same experimental setup as in Pachler et al. [67]. Neither the wet chemical analysis according to DIN 14791 nor the online Rosemount NGA 2000 showed any traces of SO_2 leaving the AR. Only in the FR exhaust gas stream SO_2 could be detected. Based on these measurements, Figure 50 shows the sulfur balance for three operating points conducted with H_2S in the fuel feed. Unfortunately the measured wet chemical concentrations in the FR exhaust gas (S in SO_2) show significant differences to the measured amount of sulfur in form of H_2S fed to the FR (S in H_2S). The online measurement with the Rosemount NGA 2000 could not be used due to the lack of accuracy, caused by the saturation of SO_2 in the condensate trap of the analyzer. The differences of sulfur entered and exited the system are between 15 and 45 % (see Table 11).

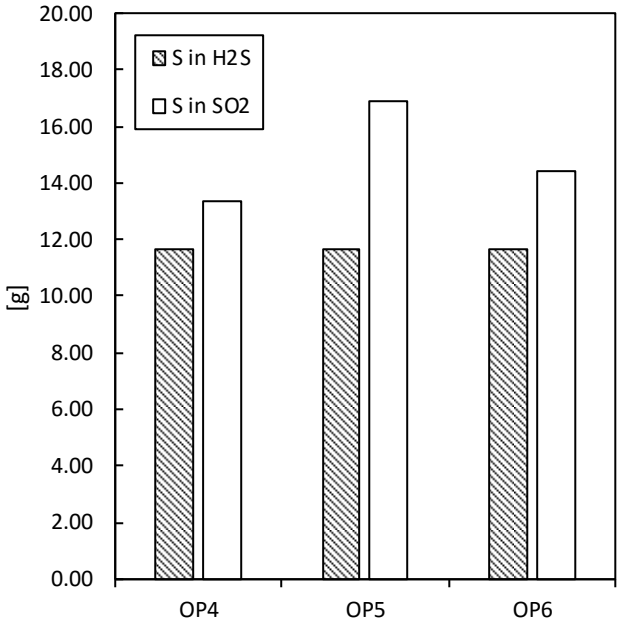

Figure 44: H_2S in the fuel feed and SO_2 concentration in the FR exhaust gas dependent upon the operation points (OP)

Table 11: Sulfur loading vs. sulfur measured at different operation points (OP)

OP [-]	**S in H_2S** [g]	**S in SO_2** [g]	**deviation** [%]
4	11.64	13.35	+14.7
5	11.66	16.89	+44.9
6	11.63	14.41	+23.9

To confirm the possible assumption of accumulation of sulfur on the particle surface as calcium sulfide, magnesium sulfide and manganese sulfide, powder X-ray diffraction (XRD) measurements in Bragg-Brentano configuration were conducted using equipment from PANalytical (X'Pert Pro) using a Cu-tube operating at 45 kV 40mA ($\lambda = 1.5406$ Å (CuKa1) and $\lambda = 1.5444$ Å (CuKa2)).

In almost all prepared samples crystalline phases of MgS were found due to H_2S in the fuel feed. Instead to the very well-defined pattern of the crystalline structures of perovskite, magnesium sulfide presents a weak XRD pattern with some overlapping reflections with different other phases. Hence, to determine the amount of the individual phases quantitatively, a pseudo-Voigt profile function was used to adjust the overall profile (Rietveld method). Further, an adaptation of the profile points was carried out based on a structural model after subtraction of the background or simultaneous adaptation of the background has been made [175]. Table 13 gives an overview of all crystalline phases that

could be identified. The highest concentration of MgS could be measured in the solid sample collected during operating point 3, 4 and 6. In the sample after the experiments with sulfur (after campaign), the lowest amount of MgS could be determined (Figure 45). These results are in accordance with the H_2S concentration in the fuel feed. However, it should be noted that the measured amounts of sulfur from MgS do not match the amounts of the three analysis methods (ICP, XRF, CHNS). As mentioned before it seems that the homogenization of the three analysis methods was insufficient and needs to be improved in future experiments. This leads to the assumption, that sulfur could be released again from the particles during the several hours lasting shut down procedure with no sulfur impurities feeding in the FR. The abbreviations ULS and LLS used in the table below stands for the location of solid sampling. Samples from the LLS representing reduced particles leaving the FR in the direction to the AR and ULS samples representing oxidizing particles out of the AR in the direction to the FR.

Table 12: Crystalline phases of analyzed oxygen carriers by powder XRD (OP: Operating point, E6: Experiment 6)

Sample	**XRD main phases**
OP1-6_ULS	$CaTi_{0.1}Mn_{0.9}O_{2.962}$, $CaMn_2O_4$, MgO, MgS
After E6 ULS/LLS	$CaTi_{0.1}Mn_{0.9}O_{2.962}$, $CaMn_2O_4$, MgO

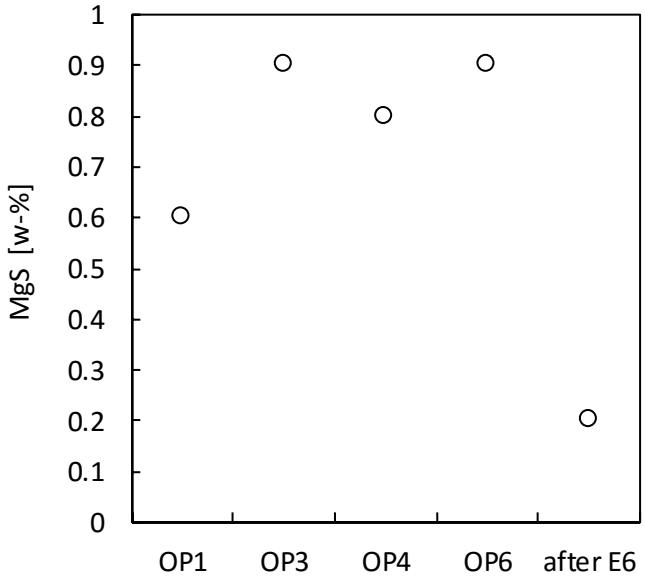

Figure 45: Concentration of MgS, measured by powder XRD analysis

5.3.3. Performance of the copper oxygen carrier

5.3.3.1. Effect on fuel conversion

Figure 46 shows the online data of the overall performance of the 120 kW_{th} CLC pilot plant at two different amounts of H_2S added to the fuel feed at 800 °C operation temperature and 73 kW_{th} fuel capacity.

Right after the amount of H_2S was increased from zero to 14 l/h (=2000 ppmv) an immediate drop of CO_2 yield was observed. With a little delay, SO_2 emission in the FR exhaust gas and subsequent FTB was detected in the Rosemount NGA 2000 online gas analytic. The lag of response was attributed to the saturation time of the SO_2 in the upstream located condensate trap (Figure 21). Condensate samples were collected during operation and the low PH value of around 2 indicates that SO_2 is dissolved. Due to the fact, the SO_2 concentrations in the FR and FTB exhaust gas are different, also the response times are varying. In addition an abrupt but also delayed ascent of CO in the FR exhaust gas was observed. Even after reducing the H_2S feed from 14 to 7 l/h (=1000 ppmv) the performance drop was clearly detectable.

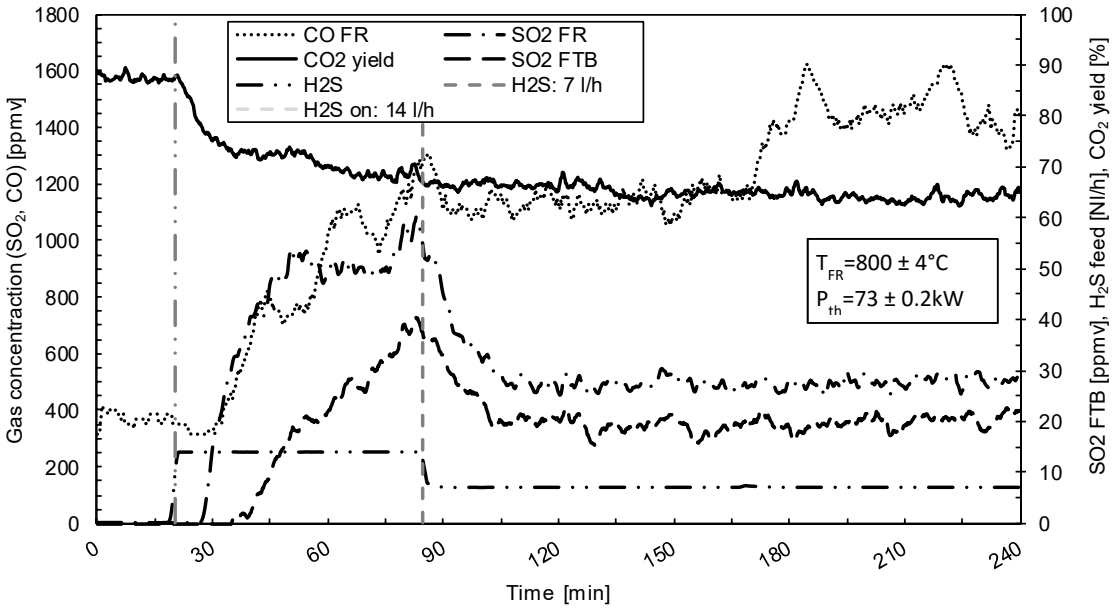

Figure 46: Online data composition of overall CLC performance with various S content in the FR feed

The reactivity of the oxygen carrier, expressed by the CH_4 conversion, also decreased significantly during the presence of sulfur in the fuel feed (see Figure 47). Every symbol in the diagram stands for a validated steady state operation point. Next to every mark the amount of H_2S, fed to the FR, is shown. The worsening of the reactivity shows digressive behavior. It could be observed that after approximately two hours of constant operation the CH_4 conversion was constant. Constant operation of the pilot plant was possible, even with sulfur impurities in the fuel feed. After switching off the H_2S supply the CH_4 conversion slowly increased again but the initial value could not be achieved any more. It must be

mentioned at this point, that the grey filled circle symbol represents an operation point at 850°C to investigate if the regeneration process of the oxygen carrier can be accelerated. Thereby the performance of the OC could be further increased but at the same time suffer a loss in lifetime caused by an increased attrition rate.

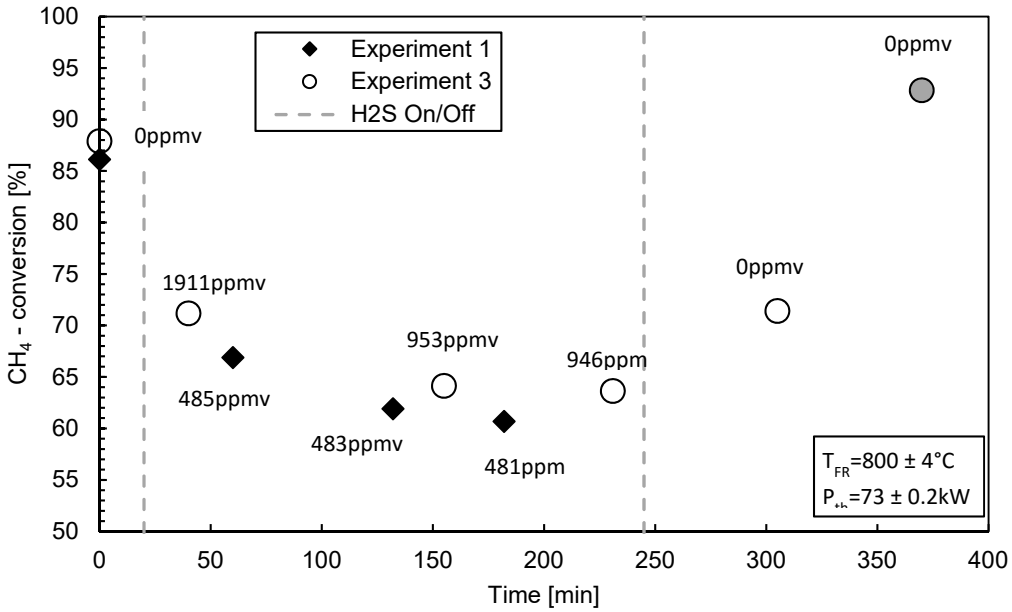

Figure 47: CH_4 conversion at 500, 1 000 and 2 000 ppmv H_2S in the FR feed

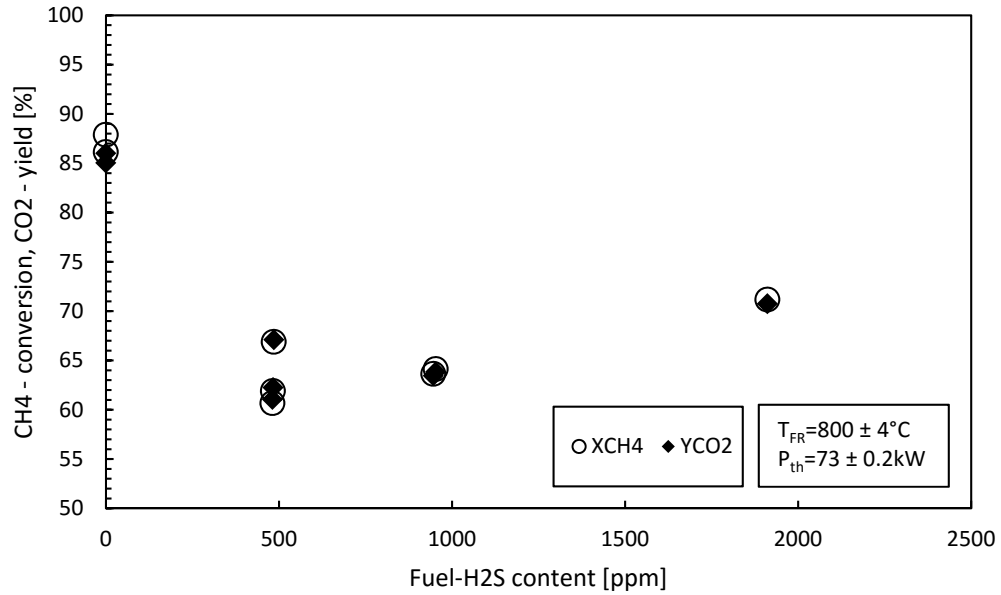

Figure 48: CH_4 conversion and CO_2 yield as a function of H_2S concentration in the fuel feed

Figure 48 represent the CO_2 yield and CH_4 conversion as a function of H_2S in the fuel feed. Due to the time-dependent performance decline a direct correlation with the sulfur in the

fuel feed is not possible. Since the deactivation symptoms of the oxygen carrier become visible only with a time delay, an interpretation of the results on the basis of the H_2S concentration is not feasible because there is a gradual sulfur loading on the particle. But it is clearly visible that the presence of sulfur adversely affects the performance.

Figure 49 shows the FR flue gas composition dependent on the sulfur feed and operation temperature. Due to the presence of sulfur, the CH_4 conversion and CO_2 yield decreased (OP17). This results in a larger amount of CH_4 and a smaller amount of CO_2 in the FR exhaust gas stream. Further a higher amount of hydrogen was measured in the flue gas during operation with 1000 ppmv H_2S in the fuel feed. After switching off the sulfur supply, a regeneration could be observed (OP18). To test the possibility to accelerate the regeneration process, the operation temperature was increased to 850°C (OP19). During this test all other operation parameters have been constant. As can be seen, the flue gas composition has returned to the initial level.

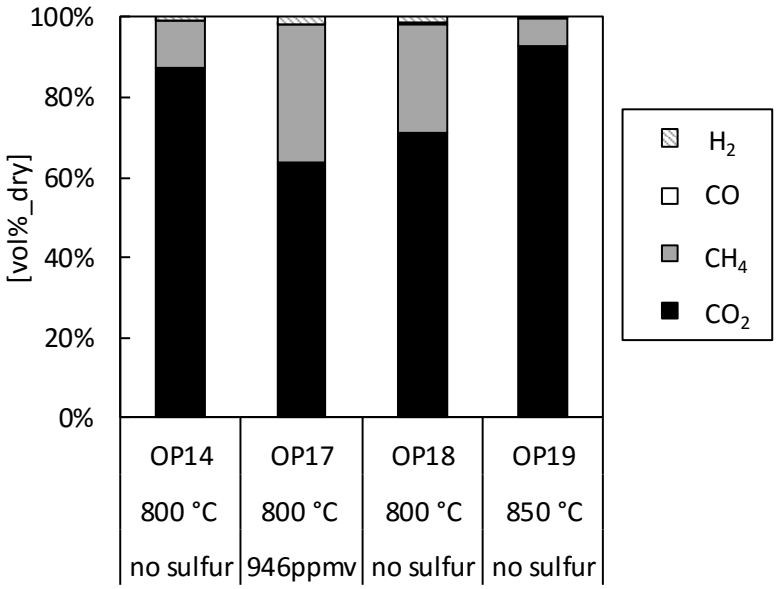

Figure 49: FR flue gas composition in subject to the sulfur fuel feed and temperature

5.3.3.2. Effect on emission

To observe the fate of sulfur inside the CLC process, H_2S and SO_2 emissions were measured during the operation. Neither the wet chemical analysis according to DIN EN ISO 14791 nor the online Rosemount NGA 2000 showed any traces of SO_2 leaving the air reactor. Only in the FR exhaust gas stream SO_2 could be detected. Resulting on the measurement data Figure 50 shows all operating points conducted with H_2S in the fuel feed and the theoretical SO_2 concentration in the FR exhaust gas in case all H_2S is converted to SO_2. The difference of the validated H_2S concentration to the calculated amount of SO_2 is mentioned as leakage. Unfortunately the measured online values as well as the wet chemical analysis of the SO_2 concentrations in the FR show significant differences to the calculated values. According to

our current knowledge, the lack of the online SO_2 amount can be the result of the mentioned, saturation time of the SO_2 in the upstream of the gas analysis located condensate trap. The difference of the wet chemical test according to DIN EN ISO 14791 to the calculated amount is clarified with further analysis explained below.

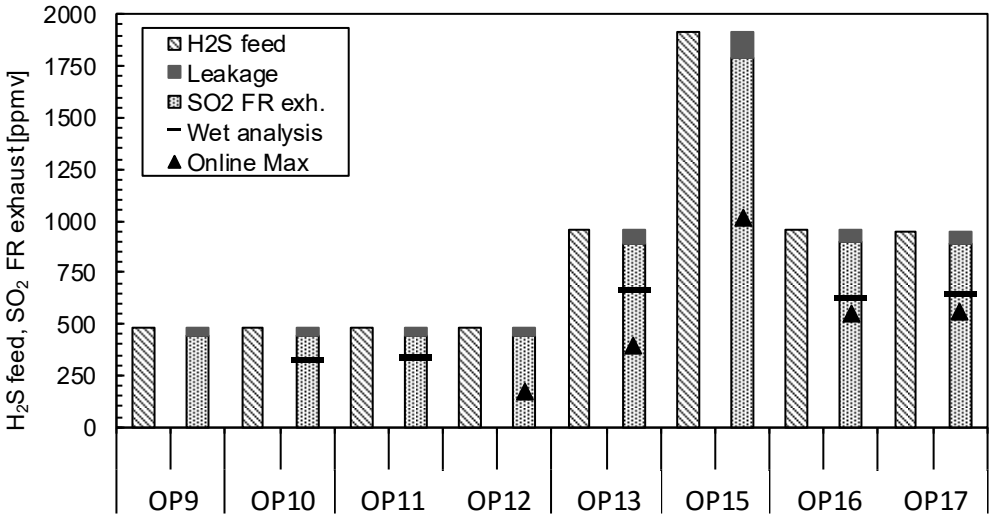

Figure 50: H_2S in the fuel feed and SO_2 concentration in the FR exhaust gas dependent upon the operation points

To confirm the possible assumption of accumulation of sulfur on the particle surface as copper sulfide and copper sulfate powder XRD analysis have been conducted. In two of the prepared samples crystalline phases of Cu_2S was formed due to H_2S in the fuel feed. Instead to the very well-defined pattern of the crystalline structures of Al_2O_3, $CuAlO_2$ and Cu_4O_3, copper sulfide presents a weak XRD pattern with some overlapping reflections with different phases. Hence, a quantitative determination was not possible. Table 13 gives an overview of all crystalline phases of some oxygen carrier samples that could be identified, listed by concentration. The highest concentration of Cu_2S could be measured in the solid sample collected after measurement campaign 7. The abbreviations LLS and ULS used in the table below stands for the location of sampling. Samples from the lower loop seal representing reduced particles leaving the fuel reactor in the direction to the air reactor and upper loop seal samples representing oxidizing particles out of the air reactor in the direction to the fuel reactor.

Table 13: Crystalline phases of analyzed oxygen carriers by powder XRD (OP: Operating point, E3: Experiment 3)

Sample	XRD main phases
OP9_LLS	Al_2O_3, $CuAlO_2$, Cu_4O_3
OP9_ULS	Al_2O_3, $CuAlO_2$, Cu_2S, Cu_4O_3
OP11_LLS	Al_2O_3, $CuAlO_2$, Cu_4O_3
OP11_ULS	Al_2O_3, $CuAlO_2$, Cu_4O_3
OP16_LLS	Al_2O_3, $CuAlO_2$, Cu_4O_3
OP16_ULS	Al_2O_3, $CuAlO_2$, Cu_4O_3
OP17_LLS	Al_2O_3, $CuAlO_2$, Cu_4O_3
OP17_ULS	Al_2O_3, $CuAlO_2$, Cu_4O_3
After E3	Al_2O_3, $CuAlO_2$, Cu_2S, Cu_4O_3

In Figure 51, the H_2S conversion for operating points with sulfurous fuel feed is shown. Hydrogen sulfide emission tests have been conducted according to DIN EN ISO 6326- 3 and additional with gas chromatography in combination with gas sampling bags. During all experiments no H_2S slip was observed, therefore, the conversion was about 100%.

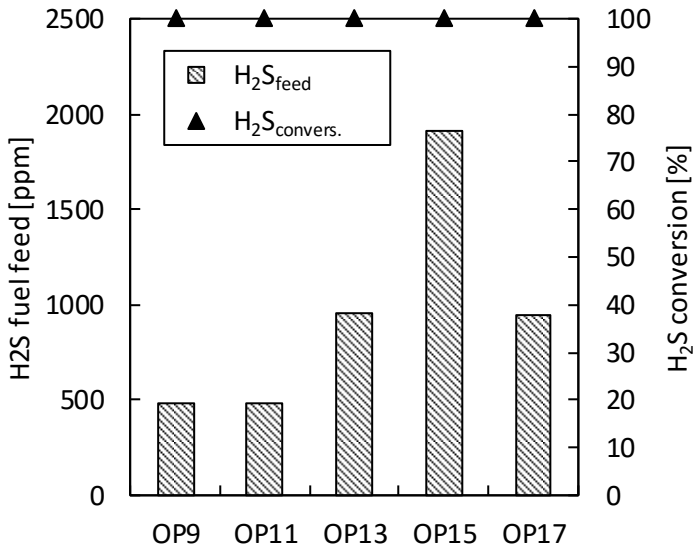

Figure 51: H_2S conversion at 500, 1 000 and 2 000 ppmv H_2S in the FR feed (OP: Operating point)

Chapter Six

6. Fluidized bed batch reactor

6.1. Concept

6.1.1. Rationale for a fluidized bed reactor system

When operating a pilot plant, the need for keeping as many parameters as constant as possible is a challenging task. In addition to the incoming and outgoing mass flows into the system, also process parameters like the solid circulation and bed inventory needs to be as constant as possible when using a dual circulating fluidized bed reactor. Especially with regard to reproducibility, a lab scale fluidized bed batch reactor has decent benefits and is a true complement to the existing 120 kW facility.

As a de-risking strategy, especially when screening a newly developed or sourced bed material, durability against impurities and cycle stability, a thermogravimetric analysis (TGA) or a batch reactor are preferred against a pilot plant. Personnel and operating expenses are a fraction when using a TGA or batch reactor, where one person alone is capable to operate the facilities. Additional a great variety of boundary conditions can be set to test the bed material for example in a wide range of degree of oxidation (X_S) when using a batch reactor or TGA. With a circulating fluidized bed pilot plant, the residence time of the particles cannot be set arbitrarily. Further no autothermic process operation is necessary and a solid fuel slip from the FR to the AR can be simulated easily when using a batch reactor. When it comes to fuel impurities like sulfur or nitrogen, the dosing and balancing is much more trivial than using a DCFB pilot plant.

6.1.2. Requirements

In contrast to the existing system, the new lab scale test rig should consist of a batch reactor, which is operated as a bubbling fluidized bed. Alternately, the oxidizing and reducing operation should take place and solid fuels as well as gaseous fuels should be able to be used.

To avoid a unnecessarily long heat up and switching time between the oxidizing and reducing cycles, the volume of the reactor system should be kept as compact as possible. To be able to investigate the influence of individual parameters on the process such as the bed temperature and the fluidization rate of the fluidized bed, constant boundary conditions must be ensured during the experiments. The bed temperature should be adjustable in the range of approx. 800°C to 950°C. To ensure a relatively constant temperature distribution

in the fluidized bed with fast heating rates, a gas preheater is inevitable. The preheater should be capable to operate in the oxidizing cycle with air as well as with steam when operated under reducing conditions.

In order to investigate the behavior of different oxygen carriers, solid sampling from the fluidized bed during operation should be possible. The resulting exhaust gas should be analyzed and the resulting data and other process data should be recorded for post processing. The exhaust gas of the pilot plant must be filtered from worn bed material, dust and ash which are transported via the exhaust gas from the reactor to the chimney. Further it must be ensured that no flammable components are left into the environment.

Besides that, the universally applicable fluidized bed batch reactor should be suitable for different types of bed materials. The nozzle plate of the reactor should be able to fluidize different kinds of oxygen carriers and be able to be operated in a large area of the bubbling fluidization regime of the Grace diagram. For the purpose of reproducibility, it must be ensured that the entire bed inventory participates in the process.

In Figure 52 the scheme of the built batch fluidized bed reactor is shown, which is capable to fulfill the requirements, mentioned before. All fluids, introduced into the system, are either controlled with a mass flow controller (MFC) like methane, nitrogen and air, or will be regulated with a rotameter (steam, purge for the oxidation catalyst). Air is needed to fluidize the fluidized bed in oxidizing operation and steam in reducing operation. In the reducing cycle, in addition to the steam, N_2 is also fed by means of an MFC via the solids metering.

With a 4/2-way ball valve (position 1) it is possible to change between the oxidizing and reducing cycles. As a result, either air or steam flows through the preheater (position 2). The preheated air or steam then flows into the airbox (position 4) where it will be evenly distributed over the cross section and then enters the reactor (position 5). The preheater and the reactor are each heated with heating furnaces (positions 3 and 6) and heating elements are additionally installed in the preheater (not shown in the figure). The fuel introduction into the system can be performed via two ways. Gaseous fuel is metered by means of an MFC and fed directly into the airbox below the nozzle plate where it then enters the fluidized bed. Solid fuels are transported to the fluidized bed with a screw conveyor via the top of the reactor.

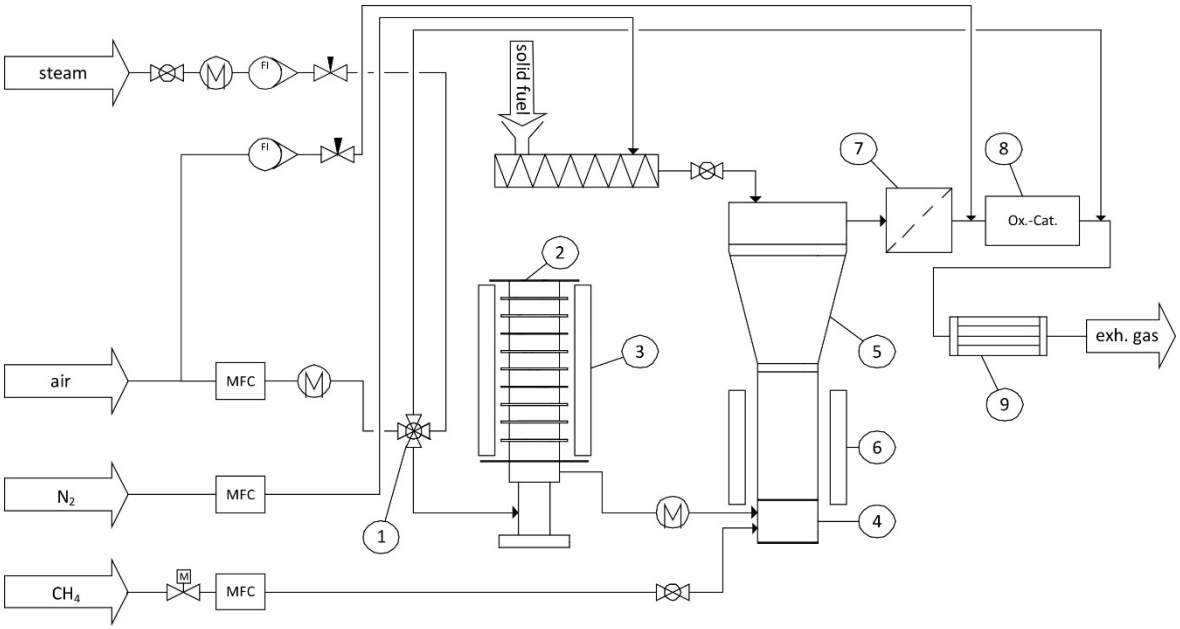

Figure 52: Scheme of the batch fluidized bed reactor

After exiting the reactor, the exhaust gas passes a sinter metal filter (position 7), where attrited oxygen carrier residues, ash or dust are filtered. A small amount of air, is fed via a bypass directly into the exhaust gas stream before the oxidation catalyst (OC) to ensure a sufficient oxidation during all operating conditions (position 8). Before the cleaned and non-flammable exhaust gas enters the chimney, it passes a condensation water/air cooler (position 9).

Table 14: main components

Pos.	**component**
1	4/2-way ball valve
2	preheater
3	heating furnace preheater
4	airbox
5	reactor
6	heating furnace reactor
7	sinter metal filter
8	oxidation catalyst
9	condensation cooler

Figure 53 shows a rendering of the CAD model, which was used to engineer the test rig as compact as possible.

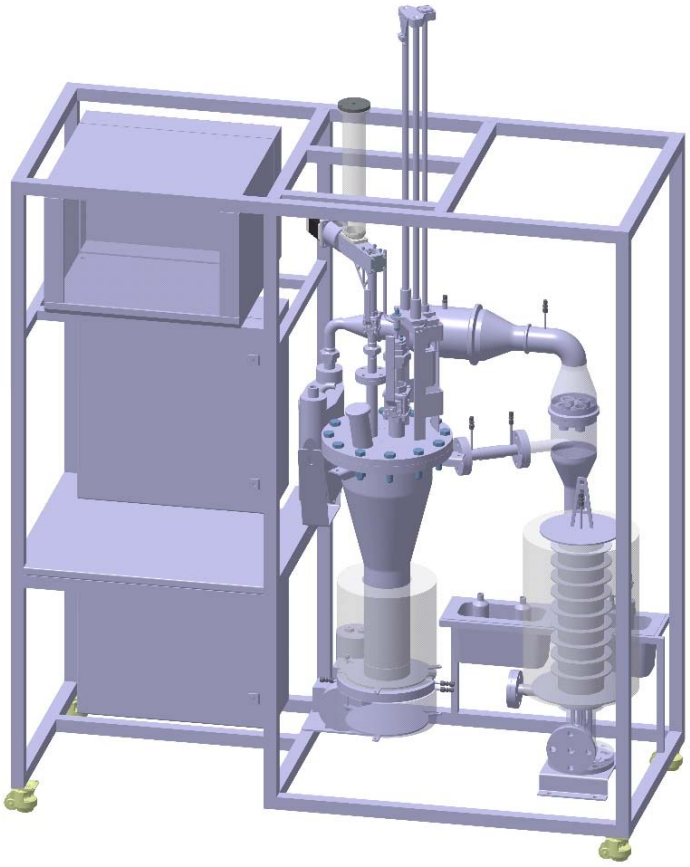

Figure 53: Rendering of the CAD model of the test rig

The finished reactor system can be seen in Figure 54, before insulating the hot parts of the test rig. The entire system is built into a moveable stainless steel frame with the dimensions of 1900 x 800 x 1960 mm. In the left area of the frame, the control cabinet with measuring equipment, measuring computer and the electrical system are housed. In the right area the reactor system with preheater, solid fuel screw conveyor, 4/2-way ball valve, steam rotameter and exhaust gas after treatment facilities are placed.

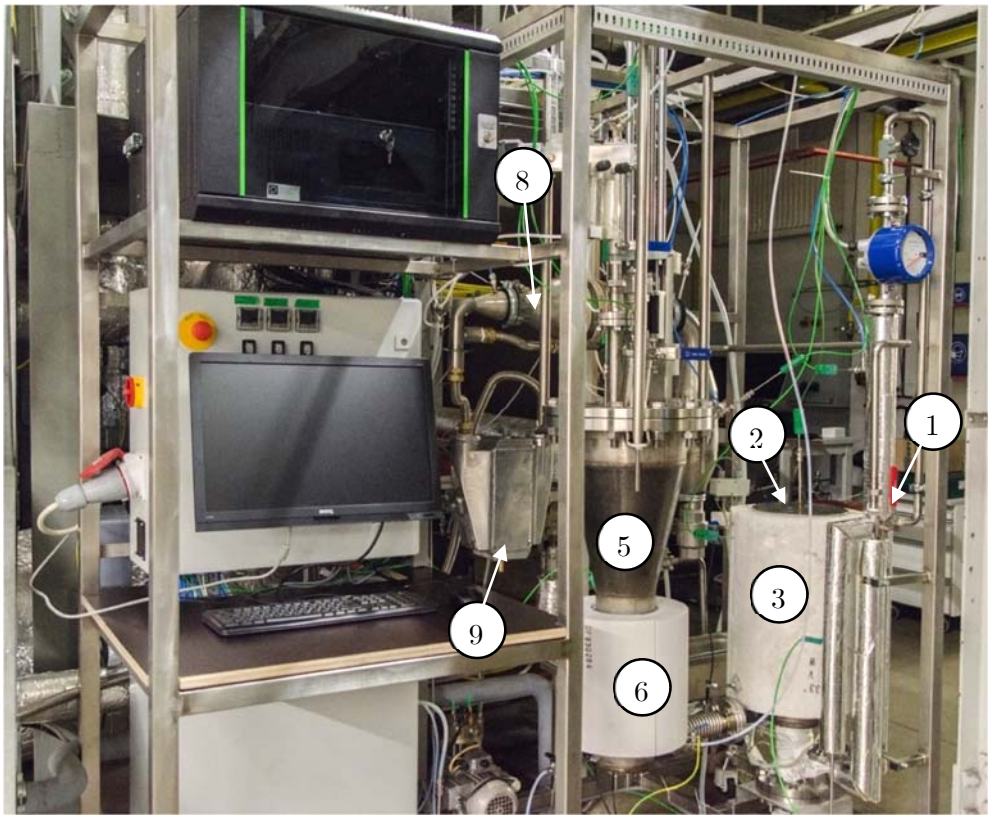

Figure 54: Finished test rig before insulation and commissioning

6.2. Design

6.2.1. General Specifications

To enable operation with different OCs, the reactor has to be usable in a wide operating range and a suitable gas distributor floor is needed to ensure that the entire bed inventory participates in the reaction. To prevent a loss of bed material from the reactor into the airbox during operation, between switching from one cycle to another or without fluidization, a suitable nozzle plate as gas distributor was used. To avoid a detachable connection in the hottest area of the test rig, right in between the heating furnace, and to reduce heat losses in this area, a welded-in nozzle plate design was chosen. In combination with the used nozzle heads, no bed material gets into the airbox. As a result, it cannot be easily opened again.

The division of the nozzle heads has a significant influence on the uniform fluidization. It should be ensured that the nozzle heads are distributed as evenly as possible on the nozzle plate, so that the entire bed material is fluidized.

In Figure 55, the layout of the nozzle heads is shown. To distribute the nozzle heads as evenly as possible on the gas distributer plate, starting from the centrally placed nozzle head, the remaining nozzle heads are arranged evenly around. In general, to maximize the gas residence time in the bed, it is desirable to introduce as much as small gas bubbles as

possible into the bed. This can be achieved by increasing the number of nozzles N within the existing constraints (manufacturability, costs, scalable). Compared to a square pitch, the holes per unit area are always more and equidistant in a grid with triangular pitch. The result is a number of 31 nozzle heads in triangular pitch.

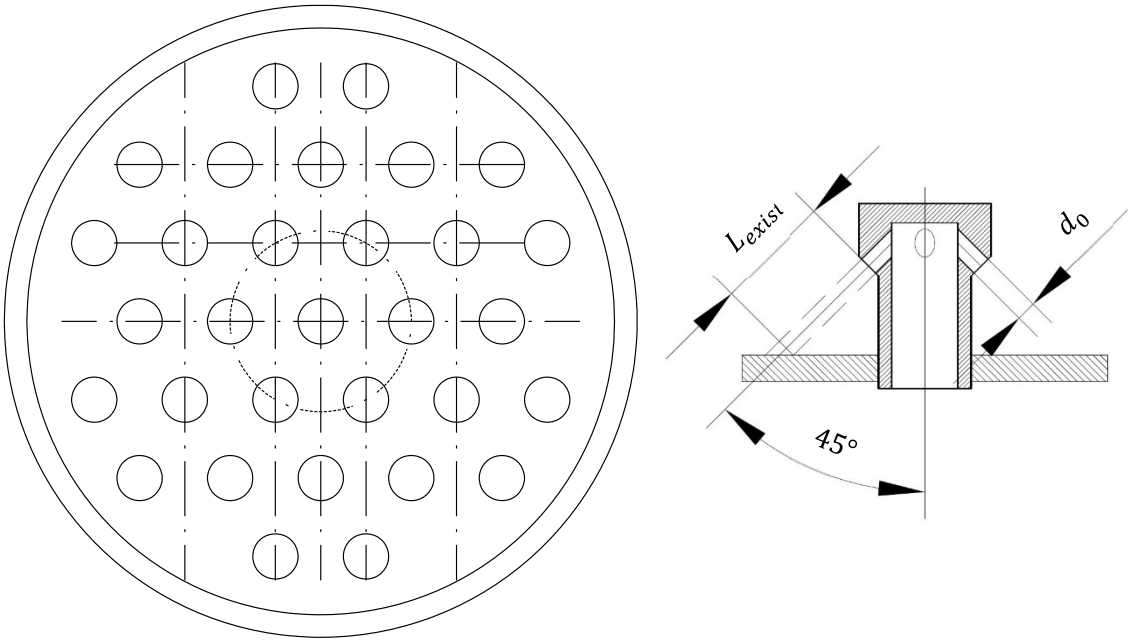

Figure 55: Illustration of the nozzle plate and nozzle head geometry

Each nozzle head has four nozzle openings which provide uniform fluidization (see Figure 55, right) over the cross section of the gas distributor. The openings are directed 45° downwards and the chosen ratio from jet diameter d_0 to borehole length prevent bed material from falling into the airbox.

An important criteria when using nozzle heads with laterally-directed flow, is the jet penetration length. To avoid damages caused by erosion, the jetting zone should not touch any surrounding components.
Knowlton and Hirsan [176] reported that the jet penetration for upwardly-directed jets L_{up} fluctuated greatly. Karri [177] noted that jet penetration can vary as much as 30% for upwardly-directed jets. However, the jet emanating from a downwardly-directed grid hole is stable and its penetration length L_{down} does not significantly fluctuate with time. According to Karri, the jet penetrations for various orientations can be approximately related by:

$$L_{up} \approx 2L_{hor} \approx 3L_{down} \tag{25}$$

There are numerous jet penetration correlations [176, 178-184] in literature. Massimilla [185] and Karri [177] have shown that the jet penetrations predicted by these correlations can

vary by a factor of 100 or more. Among them, Merry's correlation for horizontal jets was shown [177, 184, 186] to give reliable predictions. Merry's correlation to calculate the penetration of horizontal jets is:

$$\frac{L_{hor}}{d_0} = 5.25 \left(\frac{\rho_{g,h} * U_h^2}{\rho_p (1 - \varepsilon_{mf}) * g * d_p} \right)^{0.4} \left(\frac{\rho_{g,b}}{\rho_p} \right)^{0.2} \left(\frac{d_p}{d_0} \right)^{0.2} \quad (26)$$

Where L_{hor} is the jet penetration for a horizontally directed jet, U_h is the gas velocity through the nozzle opening, d_0 is the jet diameter, $\rho_{g,h}$ is the density of gas entering the nozzle jet hole (plenum conditions) and $\rho_{g,b}$ is the density of gas at bed operating conditions. Due to the deviations mentioned in literature and the fact owed the openings are directed 45° downwards, the jet penetration have been estimated including generous reserves.

The following parameters were used to design the fluidized bed (Table 15).

Table 15: Fluidized bed main design parameters

bed material		**Ilmenite**	**Cu15**
particle sieve diameter	d_P	$180\ \mu m$	$146\ \mu m$
particle density	ρ_P	$3800\ kg/m^3$	$1561\ kg/m^3$
bulk density	ρ_B	$2310\ kg/m^3$	$841\ kg/m^3$
void fraction	ε	0,392	0,461
shape factor	ϕ	0,8	0,8
Sauter mean diameter	d_{SV}	$144\ \mu m$	$116{,}8\ \mu m$
fluidizing agent			
density of air at standard conditions	$\rho_{L,N}$	$1{,}292\ kg/Nm^3$	
operating density air	$\rho_{L,B}$	$0{,}331\ kg/m^3$	
dynamic viscosity air	$\mu_{L,B}$	$4{,}6 * 10^{-5}\ Pa\ s$	
operating density steam	$\rho_{D,B}$	$0{,}206\ kg/m^3$	
dynamic viscosity steam	$\mu_{D,B}$	$1{,}24 * 10^{-5}\ Pa\ s$	
dimensions of fluidized bed			
fluidized bed diameter	d_W	$0{,}1297\ m$	
cross-sectional area of the bed	A_W	$0{,}01321\ m^2$	
bed height at minimum fluidization	h_{mf}	$0{,}1\ m$	
void fraction at minimum fluidization	ε_{mf}	0,5	

nozzle head design		
number of nozzle heads	N	31
jets per nozzle head	$-$	4
jet diameter	d_0	$1{,}5\ mm$
cross-sectional area of jet	a_0	$1{,}767 * 10^{-6}\ m^2$
calculated jet penetration lenght	L_{down45}	$4\ mm$
existing distance to nozzle plate	L_{exist}	$8{,}8\ mm$

Based on the assumption of the dimensions and number of nozzle heads, the required pressure drop of the gas distributer have to be determined, in order to control the operating range of the fluidized bed. The ratio of gas distributor pressure drop Δp_V to bed pressure drop Δp_B should be between 0.1 and 0.3. For the existing gas distributor the assumption of 0.2 has been made. The pressure drop across the bed can be calculated using equation (27).

$$\Delta p_B = \rho_P * h_{mf} * \varepsilon_{mf} * g \tag{27}$$

$$\Delta p_V = 0{,}2 * \Delta p_B \tag{28}$$

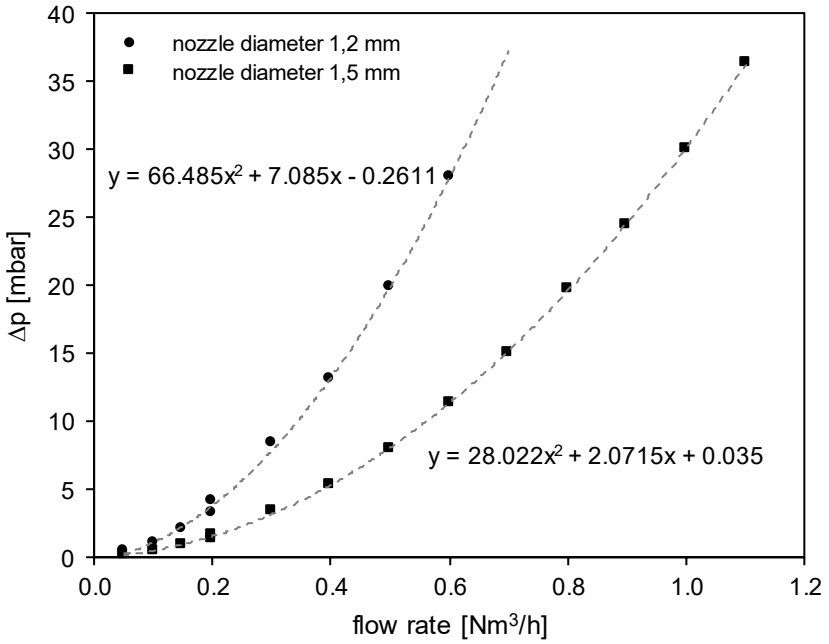

Figure 56: pressure drop of a single nozzle head in dependence of the flow rate, fuid: air

Figure 56 shows the pressure drop in dependence of the volume flow at standard conditions for a single nozzle head determined experimentally using air as fluid. The measurements have been conducted using a jet diameters of 1.2 mm and 1.5 mm. In the final design of the nozzle heads, a nozzle diameter of 1.5 mm was selected.

With the required pressure drop of the gas distributor, the volume flow in a nozzle head has been calculated using Figure 56. This volume flow is than converted to operating conditions and multiplied with the number of nozzle heads N to get to the total volume flow of the gas distributer. In a next step the superficial gas velocity has been calculated.

Because only data with air as fluid are available, the following relationship was used to calculate the velocity in the nozzle U_0 when using steam as fluid.

$$U_0 = \sqrt{\frac{2*\Delta p_V}{\xi_D * \rho_{g,B}}} \tag{29}$$

Where ξ_D represents the drag coefficient of the nozzle head and was assumed to be 1.8. The nozzle velocity U_0 was used to calculate the superficial gas velocity with the following relationship.

$$U = \frac{N * a_0 * U_0}{A_W} \tag{30}$$

To check the appropriate operating range, the operating points for the heavy more dense Ilmenite and the much lighter Cu15 have been plotted in the Grace diagram (see Figure 57). For this, the Archimedes and Reynolds number and then the dimensionless particle diameter $d_p{}^*$ and gas velocity U^* have been calculated for the oxidizing and reducing cycle and for both bed materials.

To have a wide range of applications, the reactors fluid dynamics have been designed for the very different properties of the bed materials. The fluid dynamic properties can be found in Table 16 and the chemical compositions have been described in section 2.2.

Table 16: Fluid dynamic properties

Cycle:		Oxidizing (air)		Reducing (steam)	
Bed material:		Ilmenite	Cu15	Ilmenite	Cu15
Δp_B	[mbar]	18,64	7,66	18,64	7,66
Δp_V	[mbar]	3,73	1,53	3,73	1,53
$\dot{V}_{D,N}$	[Nm³/h]	0,328	0,197	-	-
$\dot{V}_{D,B}$	[m³/h]	1,282	0,770	1,142	0,732
$\dot{V}_{ges,B}$	[m³/h]	39,74	23,88	35,41	22,69
U	[m/s]	0,835	0,502	0,744	0,477
Ar	[-]	17,38	3,81	149,81	32,84
$d_p{}^*$	[-]	2,59	1,56	5,31	3,20
Re	[-]	1,080	0,527	0,963	0,500
U^*	[-]	0,417	0,337	0,181	0,156

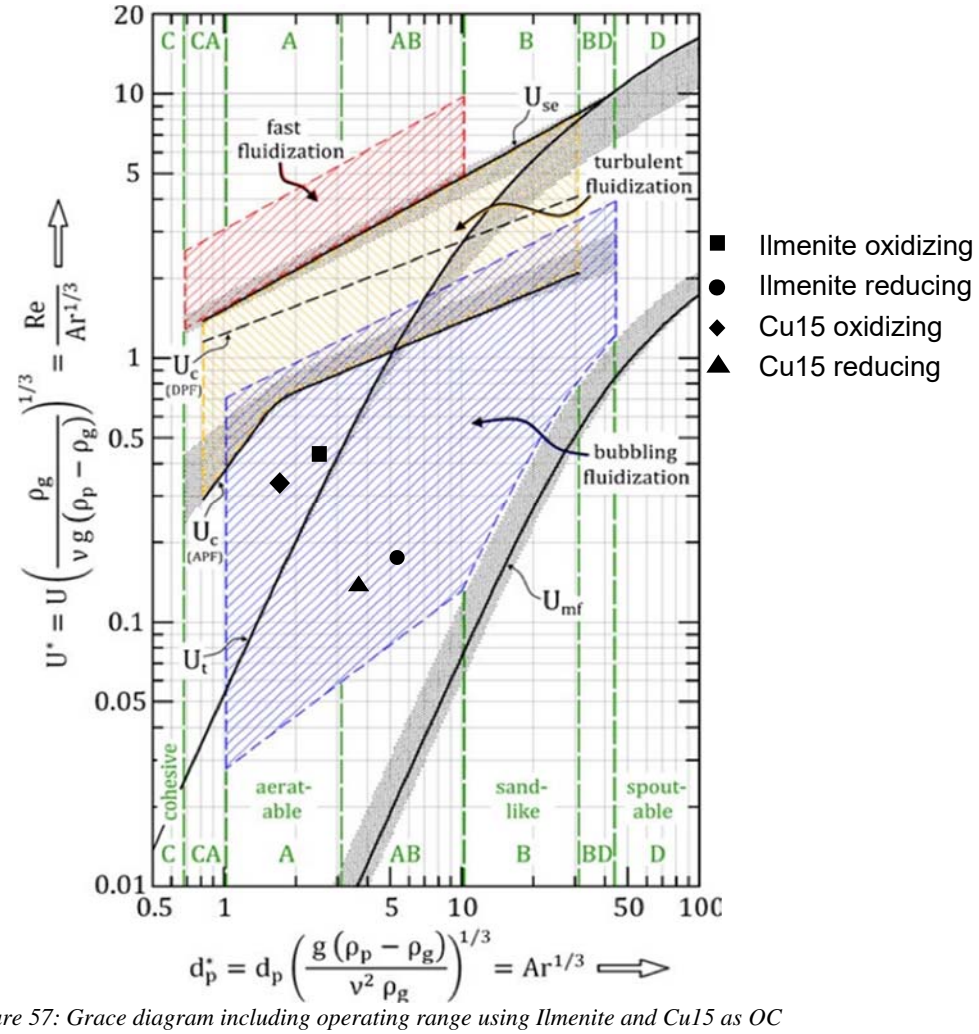

Figure 57: Grace diagram including operating range using Ilmenite and Cu15 as OC

6.2.2. Single components

In order to withstand the temperatures, a variety of the following components are made of high temperature resistant stainless steel. Table 17 gives an overview of the used pipe dimensions and material. Additional, all moveable auxiliary units like the fuel dosing, solid sampling and sensible temperature measurement equipment have been top mounted on the reactor flange to prevent it from contact with heat and to keep the design as simple and less fault-prone as possible.

Table 17: Dimensions and material of the main components

Component	Dimensions	Material
Preheater	DN 25/40/80/125	1.4841
Compensator preheater - reactor	DN 40	1.4841
Reactor	DN 25/125/250	1.4841
Compensator reactor – sinter metal filter	DN 25	1.4841
Sinter metal filter	DN 25/50/65	1.4404/1.4541
Solid fuel dosing	DN 20/25	1.4841/1.4404
Solid sampler	DN 10/40/50	1.4841

6.2.2.1. Preheater

In order to ensure the required temperatures in the reactor bed and to keep it constant, a preheating of the fluidization medium is necessary. Because no commercially design have been available, a preheater have been developed which enables to heat up air when operating in oxidation cycle as well as steam when operating in reducing cycle up to 950°C. This have been realized using a two-stage counter-current layout, which is shown in Figure 58.

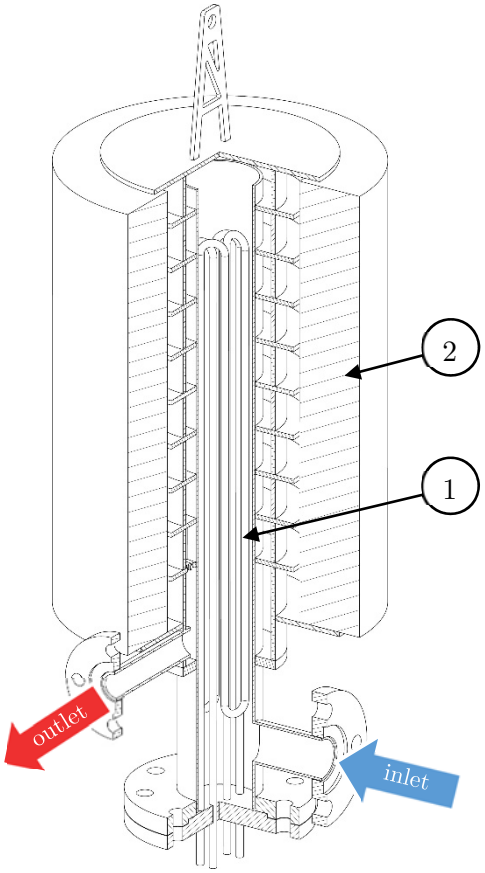

Figure 58: Cross section of the preheater layout

The incoming fluid (blue arrow) has to flow upwards through a central tube, where two heating elements (position 1), each has a power input of 3 kW, are placed to ensure fast and efficient heating. The heating elements are made of incoloy nickel iron chromium alloy and bend to our specification to fit into the central tube. Figure 59 shows the bended and flange mounted heating elements. To durably seal the four endings from the surroundings, 6 mm Swagelok fittings have been used (Figure 60). Additionally all flanges in high temperature zones have been executed with a step to improve sealing.

After the fluid reaches the upper part of the preheater, it has to pass ten chambers connected in series before exiting the preheater. On the way down, the fluid is heated a second time indirectly by a heating furnace (Figure 58, Position 2) with an electric power input of 5 kW.

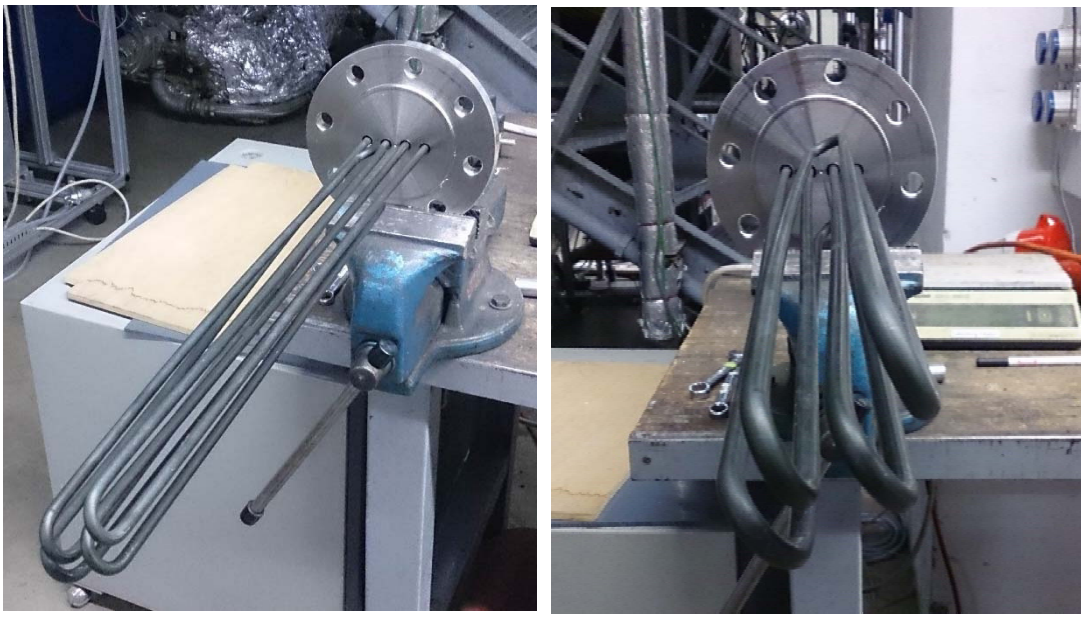

Figure 59: Heating elements flange mounted on the gas side

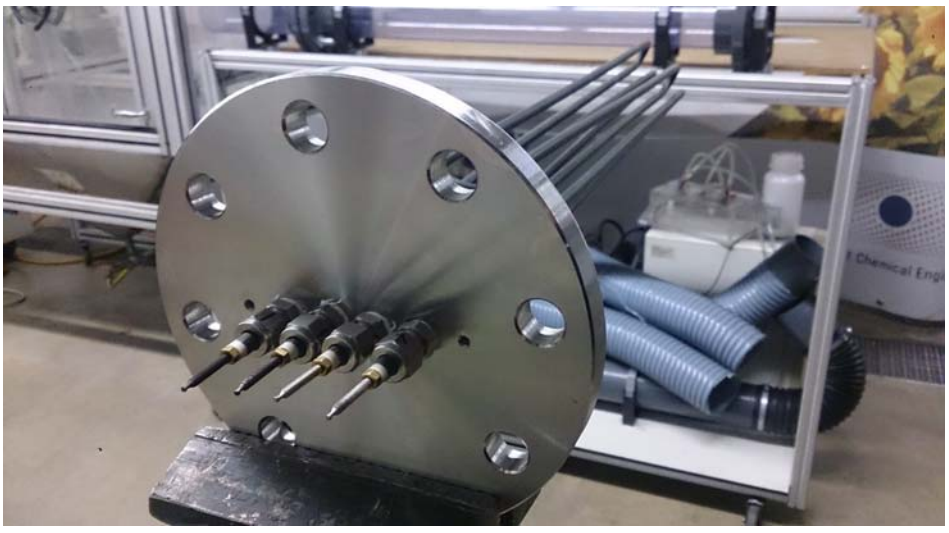

Figure 60: Heating elements with flange feedthrough on the outside

.

For an optimized heat transfer, the chambers are designed on the one hand to increase the residence time in between the heating furnace and on the other hand the dimension is set so, that the flow is turbulent in almost every operating condition, which significantly increases the heat transfer. A positive side effect of the chamber design is the significantly increased surface area, which also helps to increase the heat influx and to keep the design as small as possible. The preheated fluid exits the preheater (red arrow) via a flange connection twisted 90° to the entrance flange.

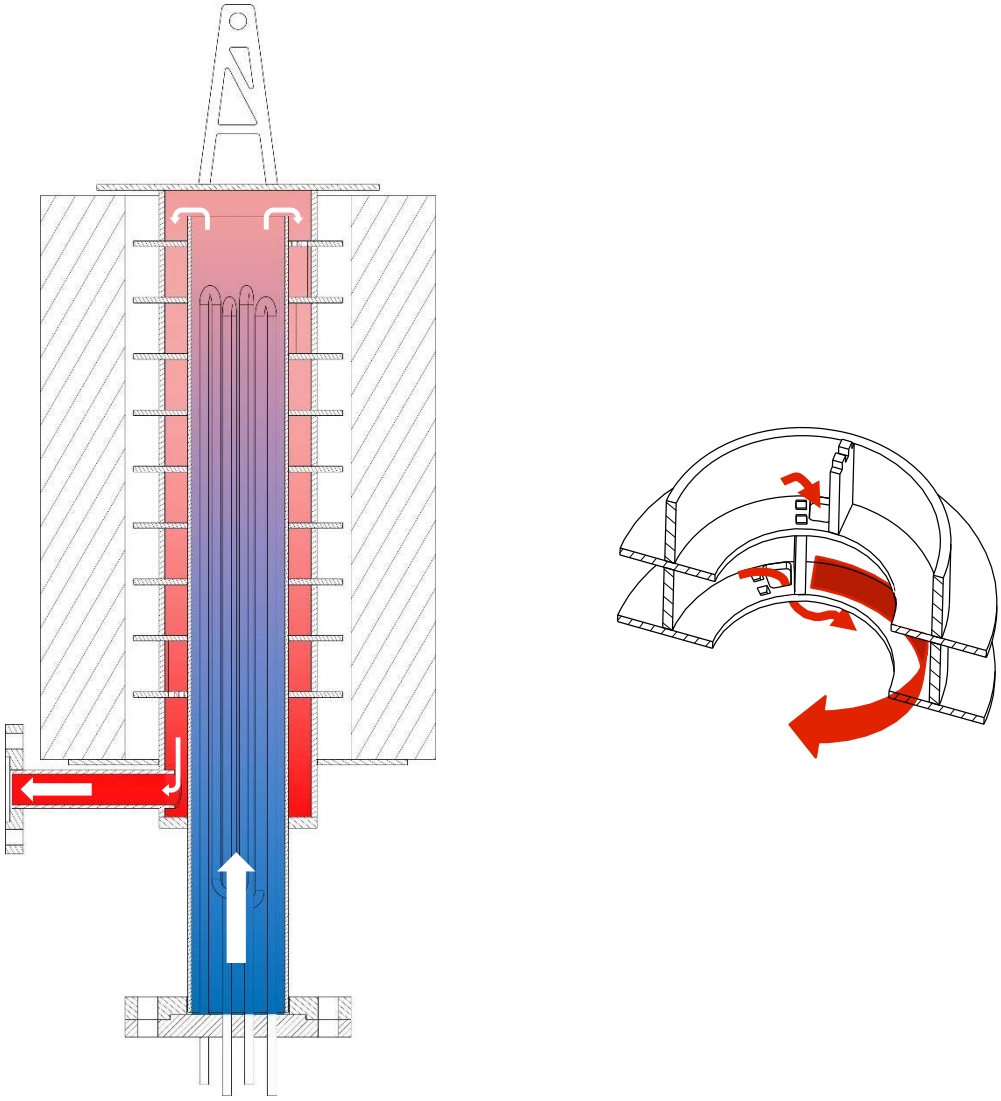

Figure 61: Flow pattern through the preheater (left) and detail of a single chamber (right)

Figure 61 left, shows the flow pattern through the preheater with indicated temperature profile. On the right side of the figure the flow direction in one of the series-connected chambers is shown. The increase in residence time has been achieved using baffles and openings from one to another chamber in special positions. In the upper area, the fluid flows outwards into the first chamber. There the baffle forces the fluid to flow around the central pipe before entering the next chamber. This is repeated nine times before exiting the preheater in direction to the reactor. The preheater is self-supported and standing executed.

6.2.2.2. Reactor

The reactor has a bed diameter of 129.70 mm and is connected via a compensator to the preheater to enable thermal expansions. In contrast to the preheater, the reactor is suspended into the frame. Figure 62 shows the dimensions of the reactor.

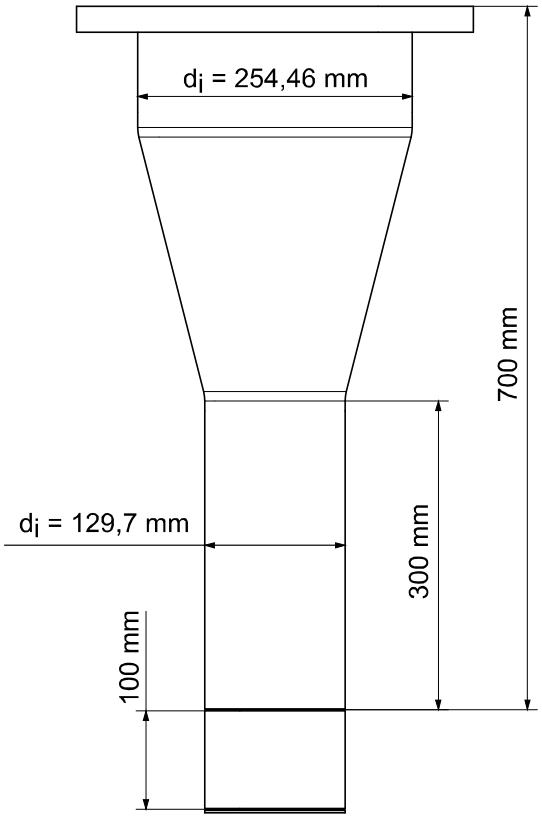

Figure 62: Reactor dimensions

Before the fluidization agent enters the reactor, it has to pass the airbox with a height of 100 mm and afterwards the gas distributor plate. The fluidization zone and the lower part of the freeboard have a height of 300 mm, then the freeboard expands to 254.50 mm to minimize the particle discharge due to entrainment. The exhaust outlet of the reactor is laterally at a height of 600 mm (not shown in Figure 62). On the very top, the reactor is sealed by a flange. To keep the design as user-friendly and maintainable as possible, all the measuring equipment, solid sampling and solid fuel feeding are lead through the flange using pressure and temperature resistant fittings (Figure 63). After exiting the reactor, a part of the flue gas is directed to the gas analysis equipment while the main amount is filtered, post oxidized and cooled before entering the chimney.

Figure 63: Preheater and reactor in detail before insulating

6.2.2.3. Solid fuel dosing

As already mentioned, the pilot plant can be operated with gaseous and solid fuels. While the gaseous fuel is introduced into the airbox and mixed with the fluidizing agent before entering the fluidized bed, the solid fuels require a different setup (see Figure 64). Through the top mounted flange of the reactor, a guiding tube with connection flange is tightly welded. A second flange mounted coaxial tube, holds the remaining components. Three different long tubes have been manufactured to be able to simulate three different solid fuel application heights. The solid fuel is introduced via a screw conveyor, which transports the fuel from a reservoir into the reactor. The drive is done with a stepper motor, mounted directly on the screw conveyor.

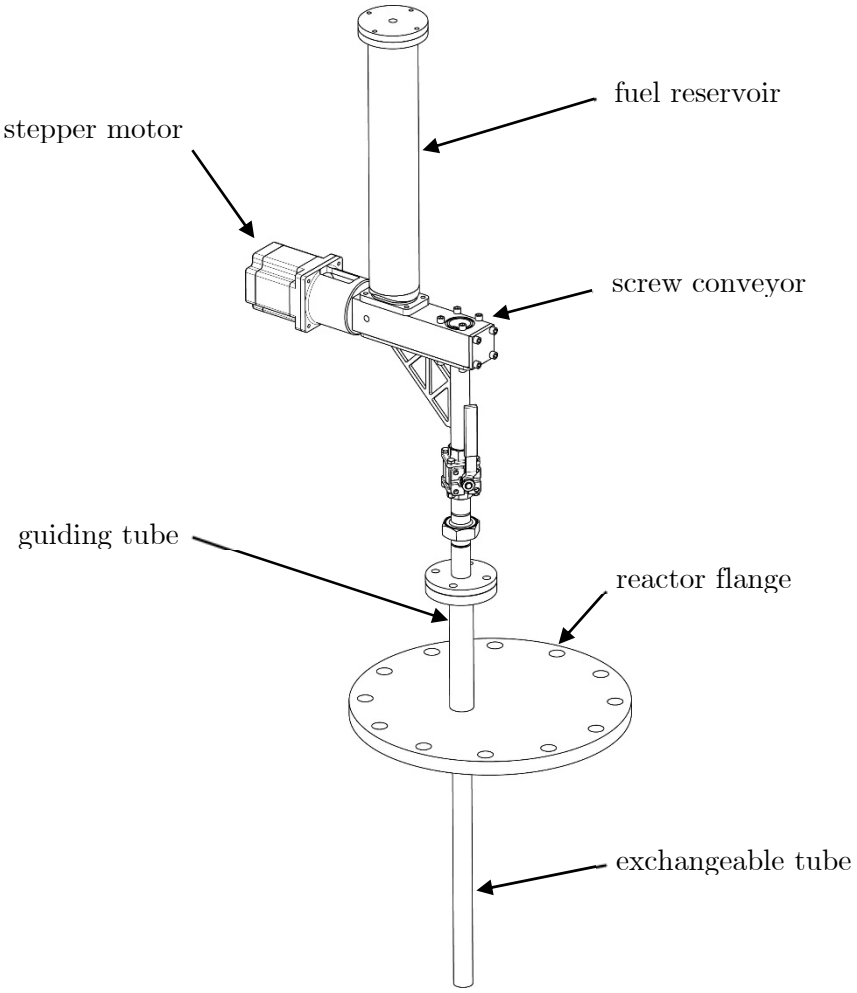

Figure 64: Flange mounted solid fuel dosing system

6.2.2.4. Solid sampler

In Figure 65 the newly developed solid sampling device is shown. Thus it is possible to take samples directly from the fluidized bed during operation. The complete sampler is placed on the reactor flange. This design was chosen mainly to protect the construction from heat and secondly to have easy access in case of failure. To ensure that only a small amount of bed material is sampled, a sample basket with a volume in relation to the bulk density of the lightest OC has been designed. The sample basket runs through a guiding tube, which is welded on the reactor flange and separated with a ball valve from the surroundings, when the sampling device is not in use. The sample basket is welded to a tube which is connected to a custom made linear axis. The linear axis consists of two linear guides and a ball screw spindle driven by a stepper motor. The entire construction is mounted on a laser cut and bent bracket welded on the reactor flange.

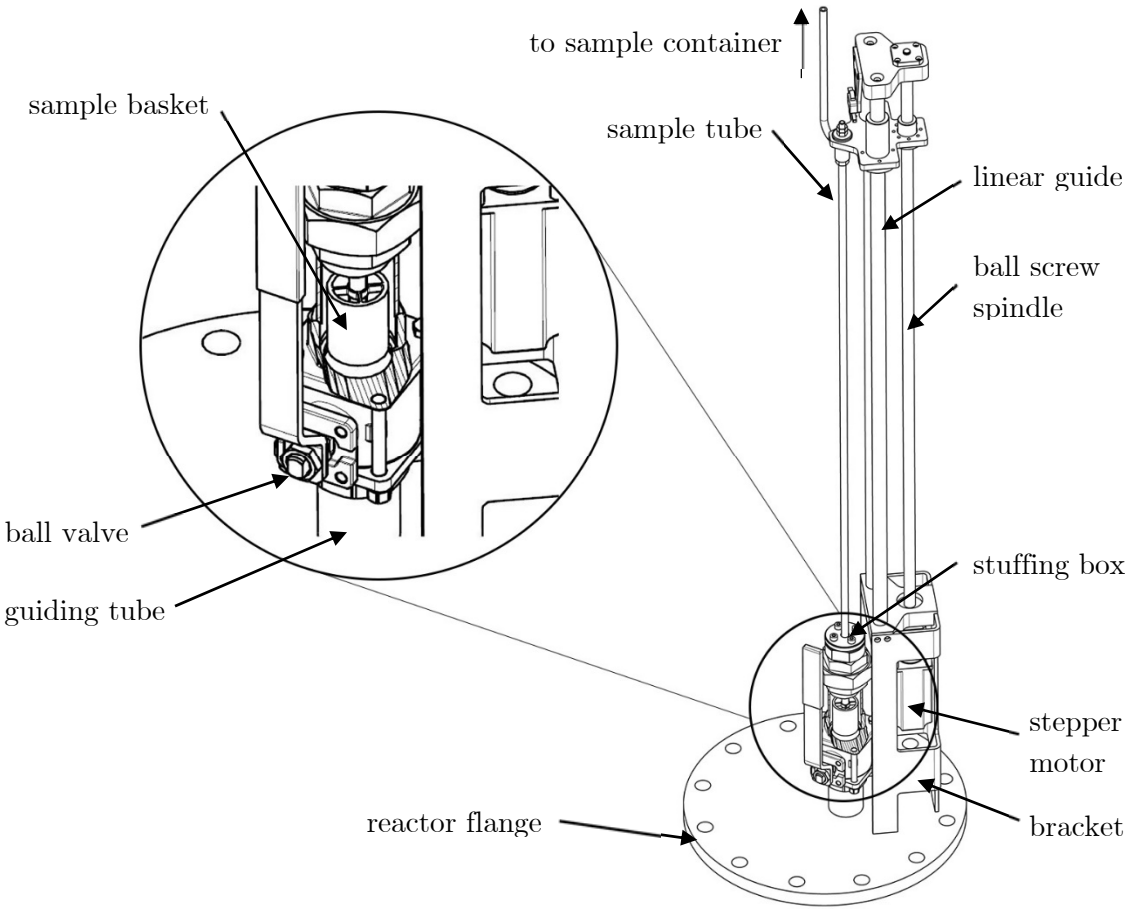

Figure 65: Solid sampling mechanism

When sampling, the sample tube and the connected basket is moved down, from the parking position between ball valve and a stuffing box, into the reactor. During this process, the ball valve is opened and the stuffing box prevents a leakage from flue gases. The adjusting range in height is predefined by means of a microcontroller and can be adjusted via LabVIEW. In default setting the sample basket dives completely into the fluidized bed.

When the basket reaches the lowest point, the position is held for 4 seconds before moving back up into the parking position. During the motion of the sample basket, the moving velocity is stepped due to mechanical oscillations. When the parking position is reached again, the ball valve has to be closed manually and the position has to be confirmed in LabView. In a next step, a vacuum pump is started automatically for 8 seconds and the sampled bed material is transported from the basket through the sample tube and flexible pipes into the sample container (Figure 66).

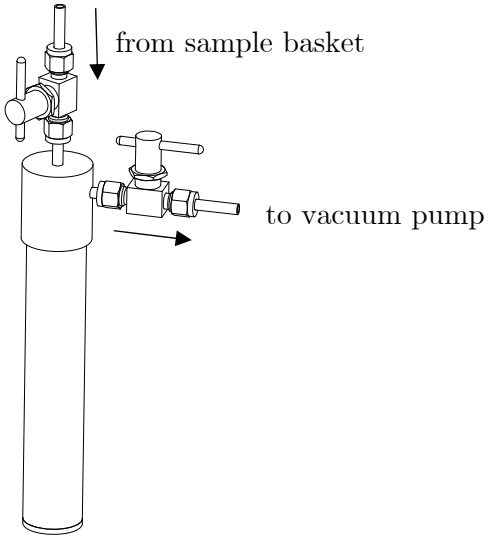

Figure 66: Sample container

The volume between ball valve and stuffing box is purged with N_2 during the sampling procedure to prevent hot sticky bed material and flue gases to contaminate this area. In addition, the sample container is cooled from the outside to prevent further reactions of the hot solid sample.

Additional it is possible to sample also during the reducing cycle. Thereby, the reactor must be fluidized with N_2 instead of steam. Otherwise vapor condenses in the sample basket and tube of the device and thus a promotion of the bed material is no longer possible. As a result, sampling during fluidization with steam is not feasible.

6.2.2.5. Sinter metal filter

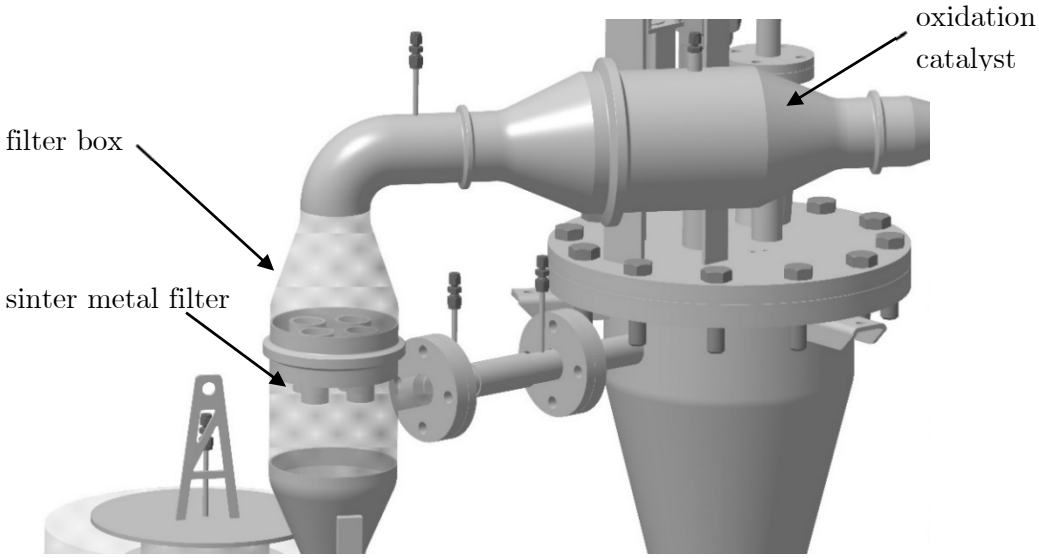

Figure 67: Sinter metal filter and oxidation catalyst

To prevent attrited bed material, ash or dust from getting into the upstream located oxidation catalyst, a filter has been designed and mounted after the reactor and before the oxidation catalysts (Figure 67).The exhaust gas is tangentially introduced into the filter box, where a first centripetal separation of larger fractions takes place. Before the exhaust gas exits the filter box, it has to pass four screwed filter cartridges, made of sinter metal (Figure 68), where the fine fractions are filtered.

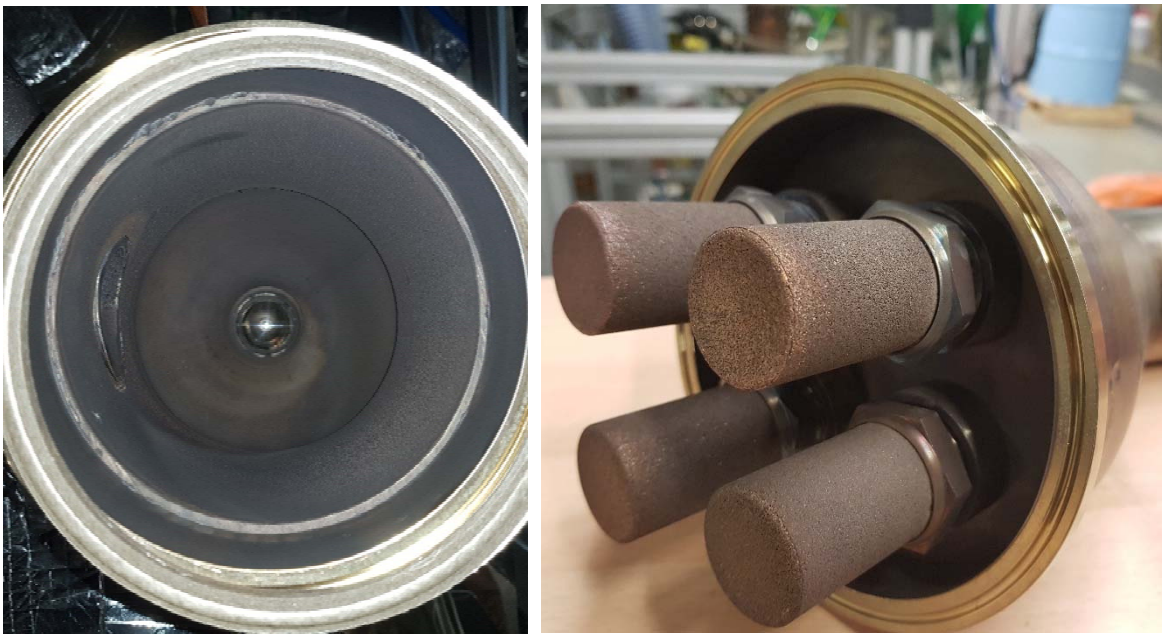

Figure 68: Sinter metal fitler box (left) and cartridges (right)

For an easy access and change, the filter box and the oxidation catalysts have been executed with four stainless steel v-band flanges and clamps (Figure 69). Additional temperature resistant graphite gaskets have been used. In the lowest part of the filter box, a ball valve have been placed for easy discharge.

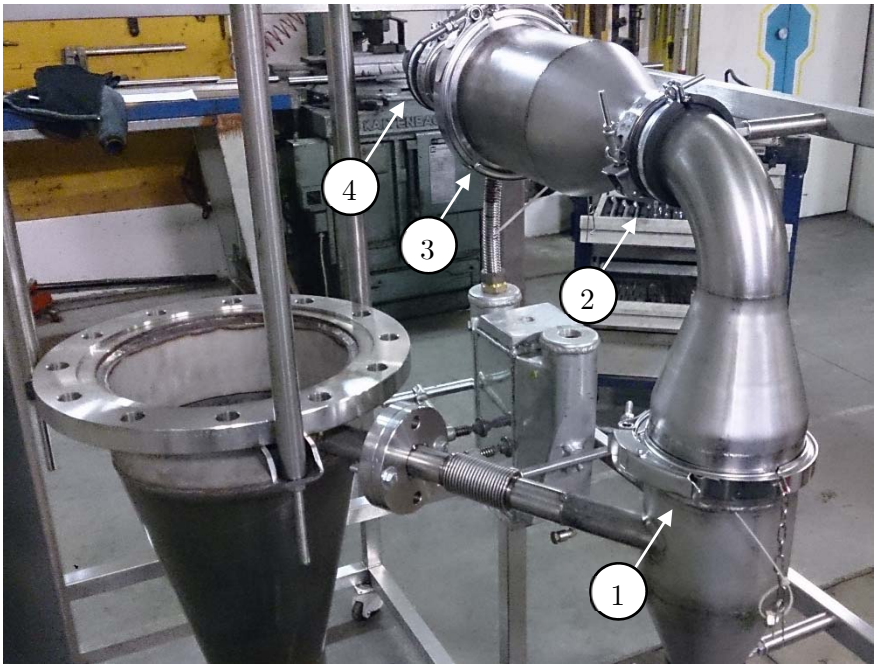

Figure 69: Location of v-band flanges

6.2.2.6. Oxidation catalyst

During the experiments, incomplete fuel conversion is very likely. To prevent unburned fuel from getting into the chimney, a post-treatment is necessary. In this case, an oxidation catalyst was used, which is located after the filter and before the condensation cooler.

Oxidation catalysts are mainly used for the exhaust gas treatment of internal combustion engines. Thereby partially oxidized components (e.g.: CO) and unburned hydrocarbons are completely oxidized. Conversion rates depends largely on the available oxygen (excess air) and the temperature of the flue gas. Figure 70 shows the conversion rate of CO and hydrocarbons as a function of temperature. It can be seen, that CO is almost completely converted at 300°C, while hydrocarbons however are converted only at higher temperatures. In addition, the conversion rate is influenced by the concentration of the educts. A higher initial concentration means a higher driving force. [187]

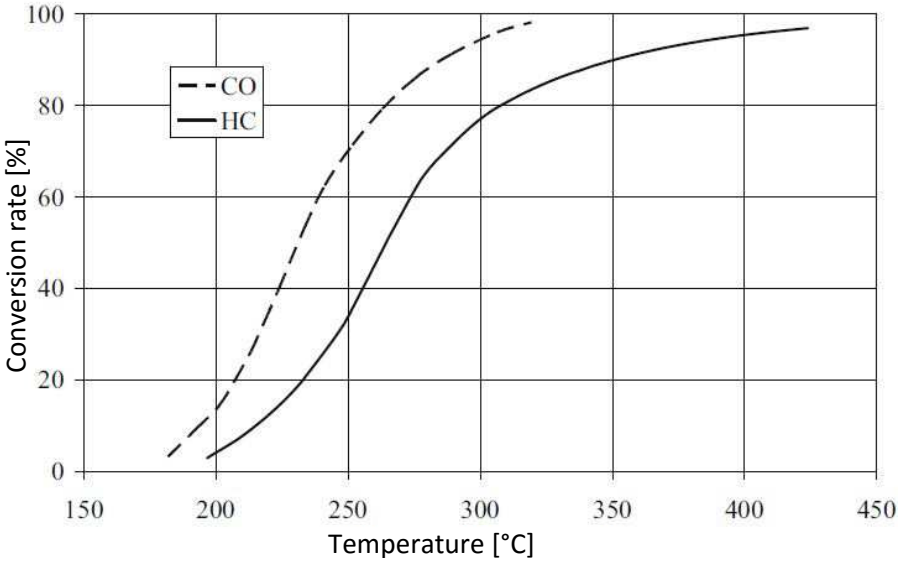

Figure 70: Temperature related conversion rate [187]

To permanently ensure the reaction, air is introduced into the exhaust stream upstream of the oxidation catalyst. To guarantee a sufficient temperature of the catalyst, it is electrically heated with a superficially mounted trace heating.

6.2.3. Measuring equipment

The entire control system as well as the data recording was realized with LabVIEW®. For the integration of temperature, pressure and flow rate signals, a "NI PCIe 6343" measurement board with two "NI TBX 68" connection boxes from National Instruments has been used. For the temperature measurements "type K" thermocouples have been used and integrated into LabVIEW® using a "RedLab TC" converter from Meilhaus. Additional temperature transmitters have been used due to the limited inputs of the "RedLab TC".

Pressure transmitters "Type DS2" from Kalinsky were used and the amount of steam was measured using a “Type H250” flowmeter from Krohne. To measure the input streams, mass flow controllers from Bürkert have been used for the regulation of air, N_2 and CH_4. For controlling the air flow a “Type 8626" was used, the “Type 8711" was used for N_2 and the “Type 8710" for measuring CH_4 has been used. Table 18 summarizes all measuring points and Figure 71 shows all the temperature and pressure measuring points inside the reactor.

Table 18: Summary of temperature and pressure measuring points and mass flow controllers

Measuring point	**Description**
TI_rotameter_steam	Steam temperature before rotameter
TIR_airbox	Temperature inside airbox
TIR_reactor_bed	Temperature inside reactor (5 mm above nozzle plate)
TIR_reactor_middle	Temperature inside reactor (inside the freeboard extension)
TIR_reactor_top	Temperature inside reactor (exit height)
TIR_reactor_outlet	temperature of the exhaust gas after the gas sampling position
TI_OC	Temperature oxidation catalyst
TIR_screw_conveyor	Temperature in the solid fuel screw conveyor
TIR_outside_heater_preheater	Temperature of the heating furnace of the preheater
TIR_inside_heater_preheater	Temperature of the heating elements of the preheater
TIR_heater_reactor	Temperature of the heating furnace of the reactor
PIR_steam_inlet	Pressure inside steam line in front of the rotameter
PIR_reactor_inlet	Pressure in the airbox
PIR_reactor_outlet	Pressure after the gas sampling position
PIR_fuel_pipe	Pressure in the solid fuel screw conveyor
PIR_fuel_bunker	Pressure in the fuel tank
PIR_DOC_inlet	Pressure between filter and oxidation catalyst
PIR_DOC_outlet	Pressure after the oxidation catalyst
FIR_rotameter_steam	Mass flow steam rotameter
MFC_Air	Mass flow controller air
MFC_N2	Mass flow controller N_2
MFC_CH4	Mass flow controller CH_4

In order to prevent condensation of vapor during the reducing cycle, a small nitrogen purge was used in the pipes to the pressure transmitter. For this reason, the pressure measuring points "PIR_reactor_inlet" in the airbox and "PIR_reactor_outlet" at the exit of the reactor were flushed with N_2.

Additionally, N_2 is introduced into the reactor via the solid fuel metering. This has been made firstly as a safety aspect, to inert the screw conveyor and secondly due to the fact, that during the reducing cycle when fluidizing with steam, the gas analysis must not fall

below a minimum dry exhaust gas flow. The N_2 volume flow is chosen so, that regardless of the fuel application, a sufficiently high exhaust gas flow is available.

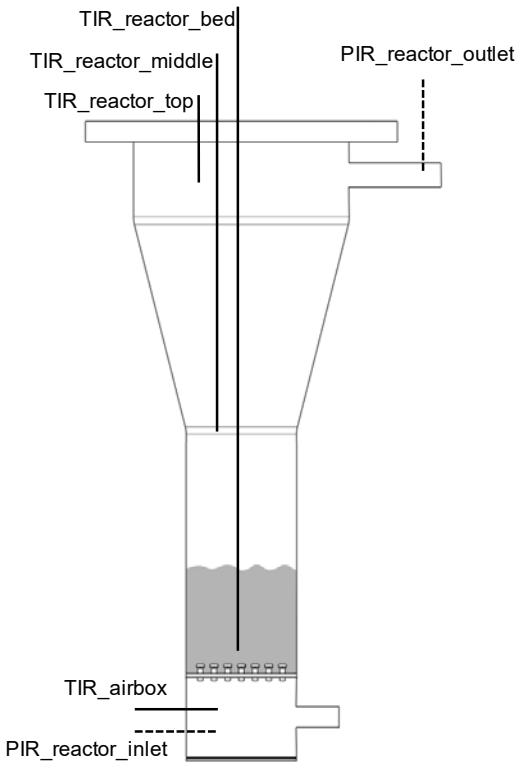

Figure 71: Position of the temperature and pressure measuring points inside the reactor

The exhaust gas used for the analysis is sampled after the reactor and before the filter and fed to the gas analysis equipment (see Figure 72).

Before the flue gas enters the analyzer, the sampled gas is dehumidified using three serially connected impinger bottles, filled with rapeseed methyl ester. The three bottles were cooled down using a cryostat ("Thermo Haacke C41") to 2°C. In a next step, the gas was filtered and a suitable volume flow was adjusted with the needle valve on the suction side of the pump. To decouple the gas analytic from pressure fluctuations in the system, the measuring device was fed separately after the pump. The exhaust gas stream was continuously analyzed with respect to CO, CO_2, H_2, CH_4 and O_2 using a Rosemount NGA 2000 infrared gas analyzer including a paramagnetic analyzer for O_2. The resulting signals have then been imported into LabVIEW® using a "NI USB 6000" connector box from National Instruments.

After each reduction cycle, the impinger bottles were emptied to prevent species in the exhaust gas to be dissolved.

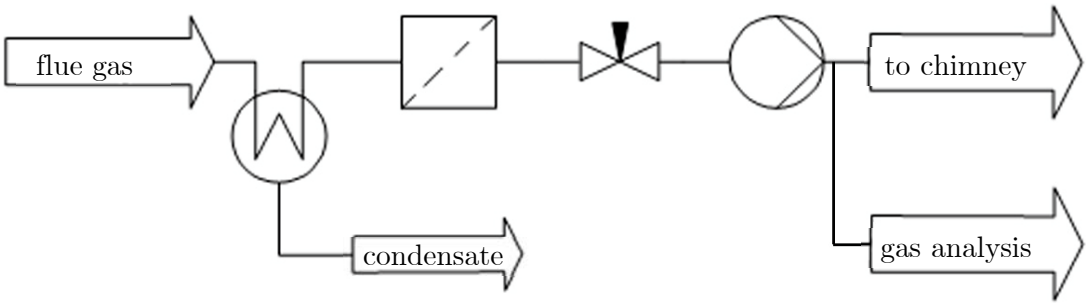

Figure 72: Gas analysis equipment

6.3. Commissioning

6.3.1. Used oxygen carrier

For the commissioning and first experiments in the fluidized bed batch reactor, ilmenite with Norwegian origin was used, which has compared to several natural ores and industrial products the benefit of higher reactivity for both gaseous and solid fuels [57]. The OC has been pretreated before start of the campaign in order to avoid agglomerations during CLC operation, by calcining at 600°C for 6 hours in an oxidizing atmosphere. A detailed composition of the fresh ilmenite can be found in Table 19.

Table 19: Composition of the Norwegian ilmenite (components >0.1 wt%)

mass fraction [wt.-%]			
TiO_2	44.08	MnO	0.301
Fe^{2+}	25.93	CaO	0.32
Fe^{2+}	9.14	V_2O_3	0.171
O mit Fe	11.36	S	0.136
MgO	3.58	Cr_2O_3	0.1
SiO_2	1.99	Balance	2.25
Al_2O_3	0.64		

6.3.2. Start up

6.3.2.1. Electric system

The first start-up of the lab scale pilot plant was conducted to test the complete electric system including all types of heaters. Thus, the system was heated to a temperature of 900 °C without bed material in the reactor. The set temperature for the controller is called "T_reactor_bed" and is located just above the nozzle plate. The temperature in the airbox (T_airbox) was set to 800 ° C.

Figure 73 gives an overview of the temperature distribution during start-up with 2.5 kg ilmenite as bed material. The installed heaters were able to reach the set point temperature in the bed after approx. 160 minutes. Up to a bed temperature of 700 °C the heating rate was between 10-15 K/min. Above 700 °C the system have been heated manually due to safety reasons.

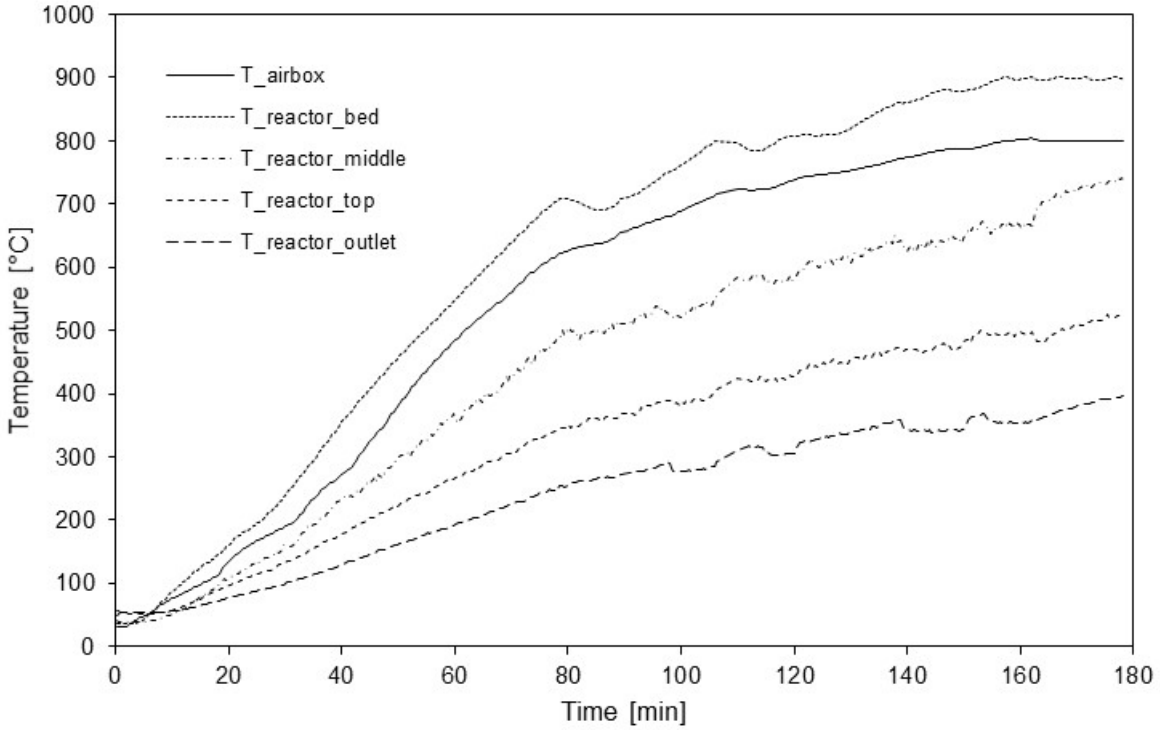

Figure 73: Temperature gradients during heat up to 900°C bed temperature

In Figure 74, the temperatures inside the reactor system during CLC operation are shown. During the first experiments, the bed temperature was set to 900 °C and the remaining temperatures arises automatically according to the heat losses in the system. Due to the endo- or exothermic reaction during CLC operation, a temperature deviation between cycles occurred. Figure 74 additionally represents the largest positive and negative deviation during operation at 900 °C bed temperature. The fluctuations occur cyclically with the switch between oxidizing and reducing operation, due to the inertia of the system.

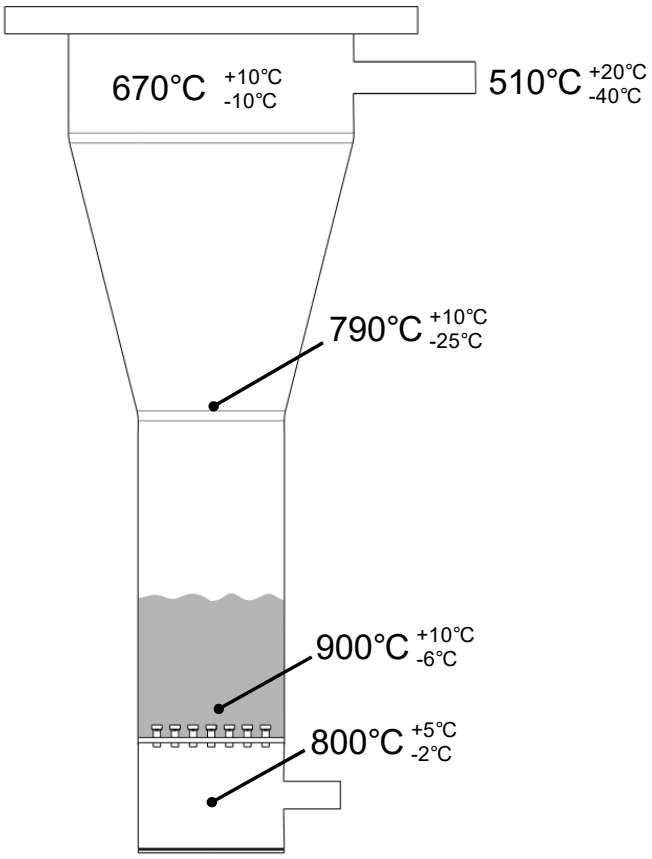

Figure 74: Temperature profile inside the reactor during CLC operation at 900°C bed temperature

6.3.2.2. Pressure drop over the gas distributor and bed

In a next step the pressure loss of the nozzle plate without bed material was measured. The tests have been conducted under four different temperatures and the volume flow varied between 3 and 16 Nm^3/h (see Figure 75). The pressure drop have been calculated using the measuring points in the airbox (PIR_reactor_inlet) and at the reactor outlet (PIR_reactor_outlet). This process was then carried out at 750, 800, 850 and 900°C. Unfortunately at 800, 850 and 900°C the operating points with low volume flows could not be measured due to the poor cooling of the heating elements in the preheater, they already reached the maximum operating temperature of 800°C. As it turned out later, this problem is reduced in cyclic operation, because of the higher heat capacity of steam, when operating in reducing cycle.

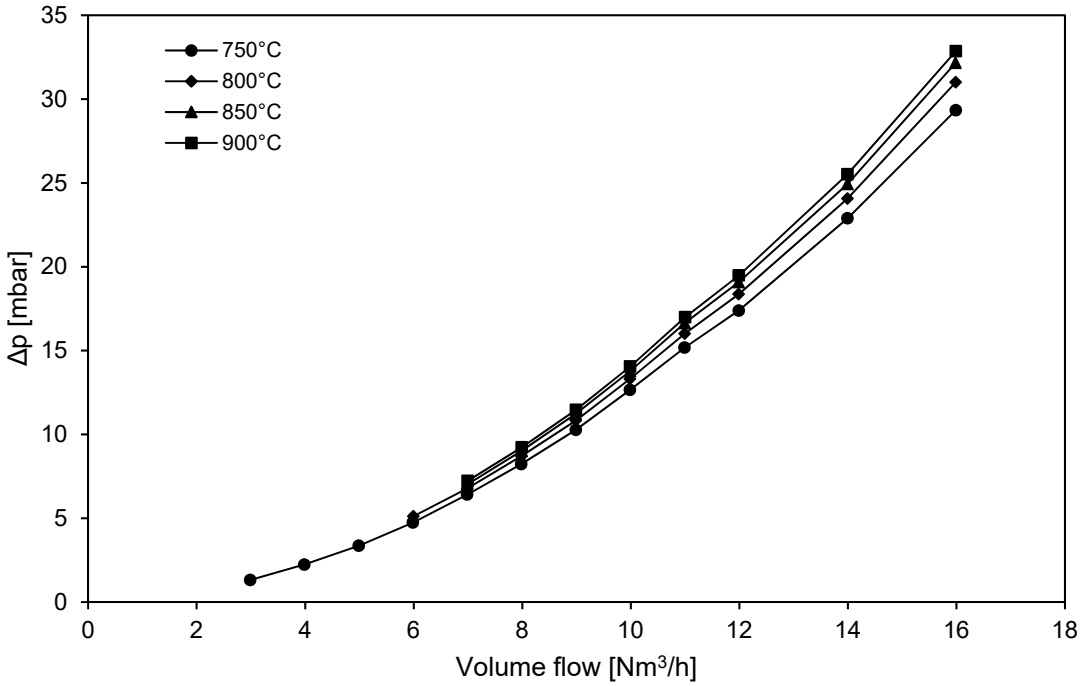

Figure 75: Pressure drop of the gas distributor without bed material in the reactor in dependence of the volume flow and temperature

Figure 76 shows the pressure drop over the fluidized bed including the gas distributor in dependence of the volume flow. The experiment was carried out under ambient temperature and with air as fluidization agent. Starting at a volume flow of 1 Nm^3/h, the fluidization was increased stepwise up to 16 Nm^3/h. The same measurements have been conducted with decreasing volume flow starting at 8 Nm^3/h down to 1 Nm^3/h. This resulted in slightly different patterns. Especially at around 3 Nm^3/h when the fluidization is close to minimum fluidization there are differences. This results from a different fluid dynamic behavior. When approaching from below, friction and adhesion forces between the particles must first be overcome before bubbles are formed. As a result, the pressure drop decreases shortly before it rises again. If approached the state of minimum fluidization from higher volume flows, this effect does not dominate and the fluidized bed is uniformly compressed.

Other than expected, the pressure drop after exceed minimum fluidization does not stay constant as shown in Figure 76. The reason for this is that in this experiment the pressure drops over the bed and over the gas distributor were measured simultaneously. The pressure drop of gas distributor increases continuously with increasing volume flow. Unfortunately, a measurement of only the pressure drop of the gas distributor was not carried out at ambient temperature. Thus the corrected pressure drop profile of only the fluidized bed cannot be determined.

The pressure drop measurements were also used to check the pressure transmitters. For this purpose, the pressure measurements have been cross-checked by external pressure sensors and compared for deviations.

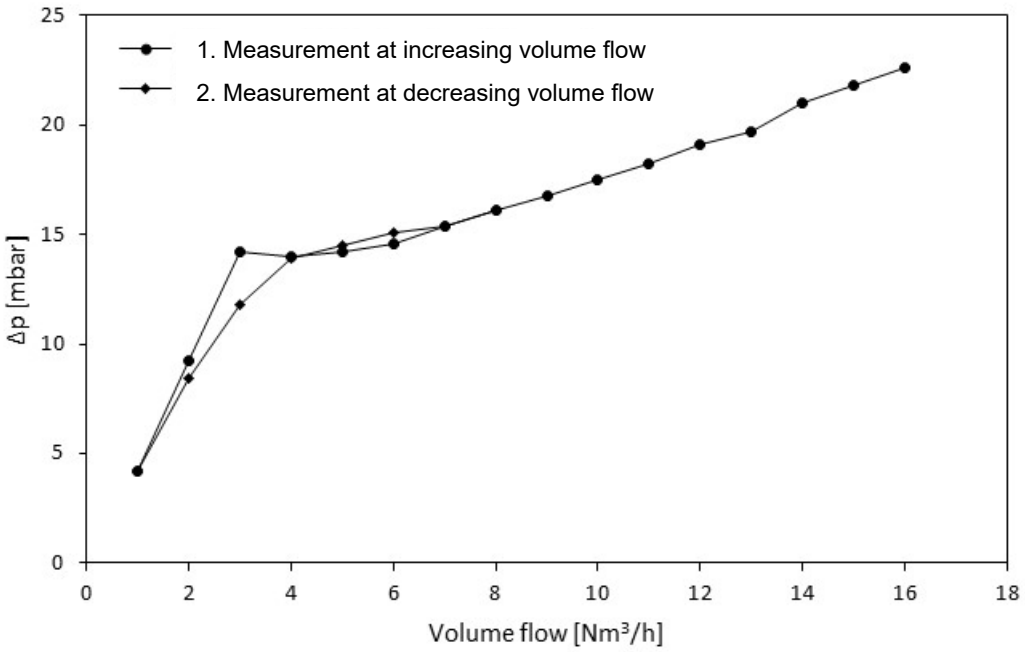

Figure 76: Pressure drop over the fluidized bed in relation to the volume flow under ambient conditions

6.3.2.3. Solid fuel dosing system

For a defined solid fuel dosing, the amount of fuel delivered through the screw conveyor has been measured and validated. This was determined using wood pellets with different dosing velocities (Figure 77). It was found, that the delivery rate varies strongly at constant screw speed. One reason for this are the pellet properties, as they are quite hard and greatly different in length and tend to block the screw, thus interrupting promotion. Additionally, the larger pellets block the screw inlet and thus leads to an unsatisfactory loading of the screw.

To take the problems into account, fresh pellets have been conveyed once through the screw conveyor, before they have been used for experiments. With this pretreatment, the dosing was much more constant, resulting in fewer deviations (see Figure 77).

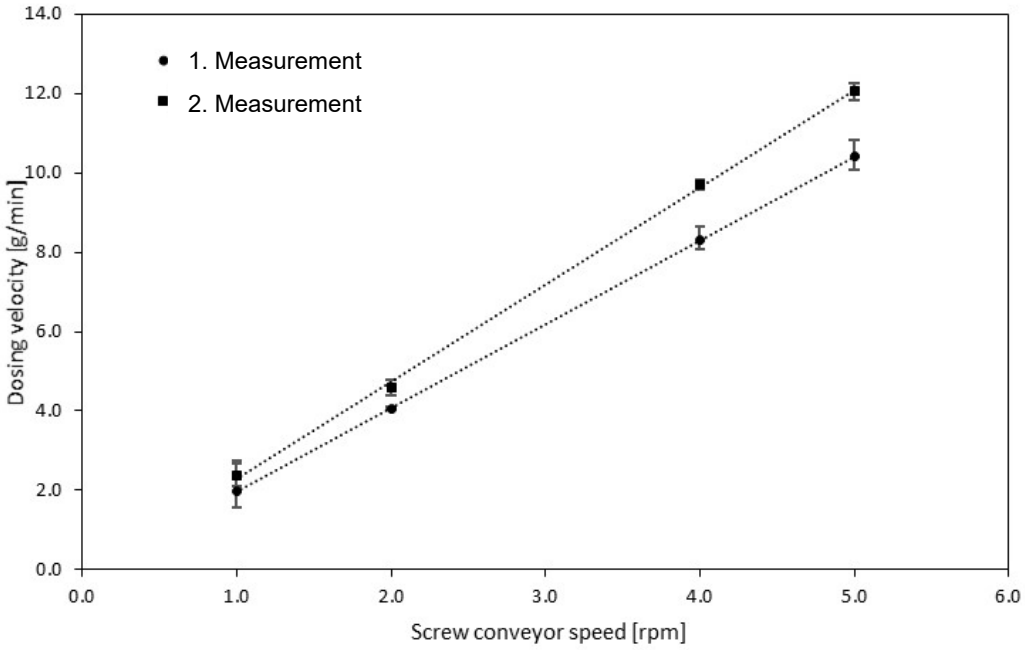

Figure 77: Dosing velocity in relation to the screw conveyor speed

6.3.2.4. Verification of the post oxidation catalyst

One important safety precautions is the commissioning and correct function of the oxidation catalyst. For this purpose, experiments have been carried out at a bed temperature of 950°C. As fuel, 9.7 g wood pallets, the same amount like in the experiments, have been fed at a dosing velocity of 4.83 g/min. The batch reactor has been fluidized with steam and the resulting exhaust gas composition was measured online. For comparison reasons, this procedure has been repeated three times and the sampling gas was taken once before and twice afterwards the oxidation catalyst. Figure 78 shows the effectiveness of the oxidation catalyst. Due to the different air purge streams and for comparison reasons, the recorded volume concentrations were converted into volumetric flows. It can be clearly seen, that there are significant amounts of CO in the exhaust gas before the oxidation catalyst (see Figure 78, above). CH_4 and H_2 are also clearly perceptible. In comparison with the two lower diagrams, the amount of CO_2 is significantly increased and the remaining amounts of combustable species are drastically reduced. Increasing the oxidation catalyst heat tracing temperature from 370°C to 390°C and increasing the amount of air purge, increases again the conversion (see Figure 78, below). CO and H_2 have been almost completely removed and CH_4 is reduced to a very low limit.

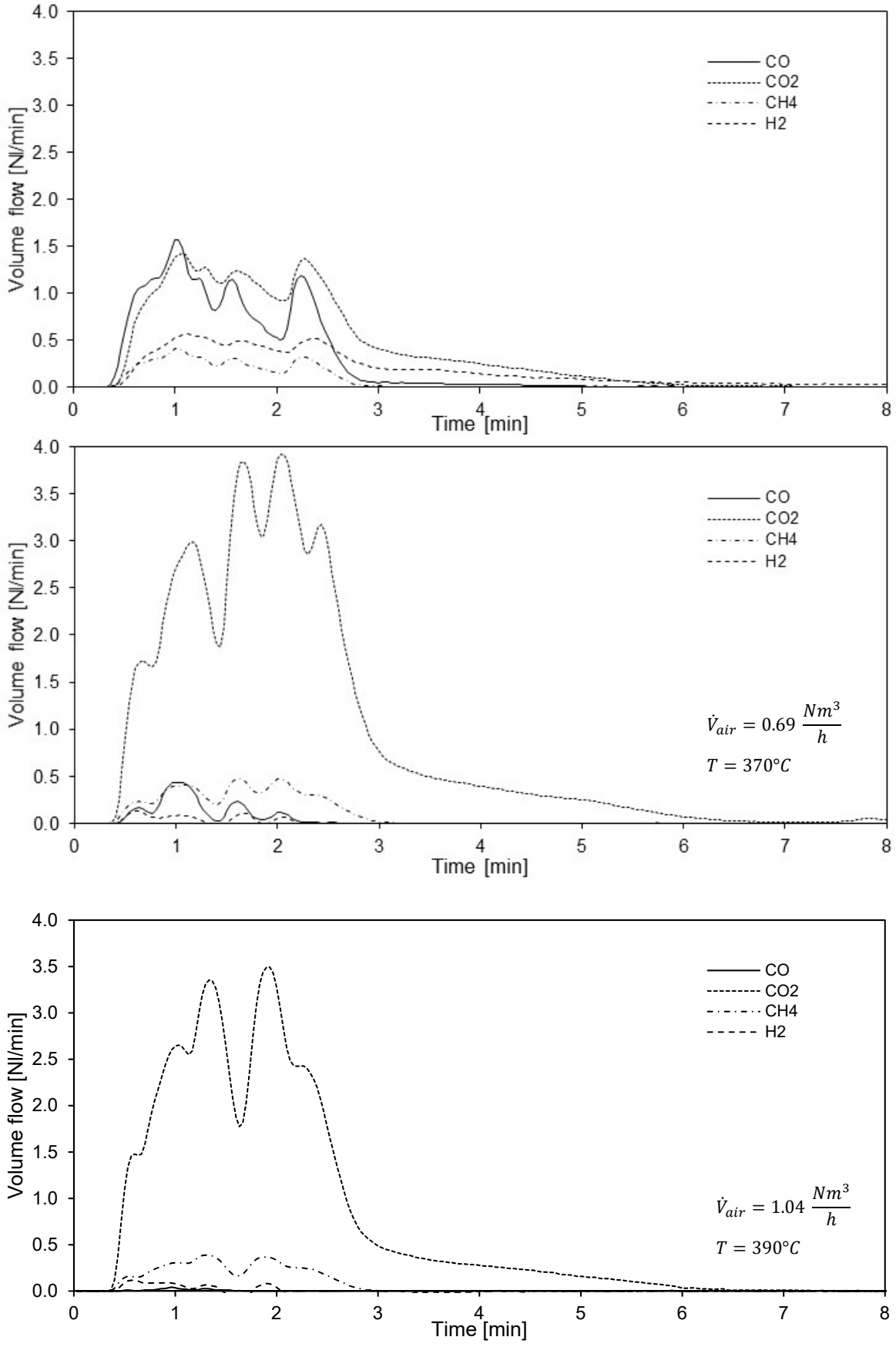

Figure 78: Verification of the function of the oxidation catalyst, above: before OC, middle and below: after OC

6.4. CLC experiments

6.4.1. Data evaluation

6.4.1.1. Carbon balance

For the determination of the converted carbon, a carbon balance is necessary. This requires calculating the exact amounts of CO, CO_2 and CH_4 leaving the reactor and set it in relation to the carbon input.

The used gas analysis equipment measured the volume fractions φ_i of the individual components, but the total exhaust gas volume flow $\dot{V}_{EG}$ is unknown. As a result, the direct calculation of the molar flow of the individual components is impossible. Under the simplified assumption, that the exhaust gas consists exclusively of CO, CO_2, CH_4, H_2, O_2 and N_2, the following balance can be made.

$$\dot{V}_{EG} = \dot{V}_{CO} + \dot{V}_{CO_2} + \dot{V}_{CH_4} + \dot{V}_{H_2} + \dot{V}_{O_2} + \dot{V}_{Rest} \tag{31}$$

$$\dot{V}_{EG} = \dot{V}_{EG} * (\varphi_{CO} + \varphi_{CO_2} + \varphi_{CH_4} + \varphi_{H_2} + \varphi_{O_2}) + \dot{V}_{Rest}$$

In the reducing cycle N_2 was used as carrier gas, thus the volume flow $\dot{V}_{N_2}$ is known and can be equated with $\dot{V}_{Rest} = \dot{V}_{N_2}$ to:

$$\dot{V}_{EG} = \frac{\dot{V}_{N_2}}{1 - (\varphi_{CO} + \varphi_{CO_2} + \varphi_{CH_4} + \varphi_{H_2} + \varphi_{O_2})}$$

With the following relationships, the mass flow rates of the individual components can then be calculated.

$$\dot{V}_i = \dot{V}_{EG} * \varphi_i \tag{32}$$

$$\dot{n}_i = \frac{\dot{V}_i * \rho_i}{M_i} \tag{33}$$

By using the trapezoidal rule for numerical integration of the time course of the individual components, the total molar amount of a species was calculated.

$$n_i = \int_0^x \dot{n}_i(t)\, dt \sum_{y=1}^{x} (t_y - t_{y-1}) * \left[\dot{n}_i(t_{y-1}) + \frac{\dot{n}_i(t_y) - \dot{n}_i(t_{y-1})}{2} \right] \tag{34}$$

In order to achieve a uniform evaluation, the integration limits have been set according to a specific procedure. The start time of the reduction cycle was set ten data points, i.e. 18 seconds before the first increase in CO_2 concentration occurred. The end time for integration was set, when the exhaust gas concentrations returned to the initial values before the reduction cycle.

To compare the individual operating points with each other, the mass of carbon in the exhaust gas has been related to the mass of carbon in the fuel feed.

$$m_{C,i} = n_i * M_C \tag{35}$$

$$m_{C,EG} = m_{C,CO} + m_{C,CO_2} + m_{C,CH_4}$$

Thus, the ratio of mass fraction of carbon in the exhaust gas in relation to the fuel carbon can be calculated in wt.-%.

$$w_C = \frac{m_{C,EG}}{m_{C,Fuel}} * 100\% \tag{36}$$

$$C_{loss} = 1 - w_C \tag{37}$$

6.4.1.2. Oxygen balance and conversion level

Because of the possibility to take solid samples from the reactor during operation, the degree of oxidation (conversion level, X_S) of the oxygen carrier can be determined. Hence a sample has been taken after the oxidizing and reducing cycle of the same OP. After the initial weight has been determined, both samples have been placed in a muffle furnace, for complete oxidation and the weight gain was documented.

The degree of oxidation X_S can be calculated as follows [188].

$$X_S = \frac{m_{ox} - m}{m_{ox} * R_O} \tag{38}$$

$$R_O = \frac{m_{ox} - m_{red}}{m_{ox}} \tag{39}$$

Where, R_O is the oxygen transport capacity of the used OC, m_{ox} is the mass of the fully oxidized OC and m is the initial weight of the OC. For the used ilmenite, the calculation of Mayer [189] have been used.

$$R_O = 0{,}05008 \frac{kg}{kg}$$

The first solid samples were taken during OP5 (Table 21). In a next step the degree of oxidation X_S has been compared to the fraction of oxygen in the exhaust gas relative to the total oxygen capacity of the oxygen carrier.

For this purpose an oxygen balance has been calculated with the assumption, that all the oxygen released by the OC leaves the reactor in the form of CO, CO_2 and H_2O. The total mass of oxygen in the exhaust gas can be calculated as follows.

$$m_O = m_{O,CO} + m_{O,CO_2} + m_{O,H_2O} \tag{40}$$

$$m_O = n_{CO} * M_O + n_{CO_2} * 2 * M_O + n_{H_2O} * M_O$$

The entire available oxygen can be calculated with R_O and the mass of bed material m_{OC}.

$$m_{O,OC} = m_{OC} * R_O \tag{41}$$

$$w_O = \frac{m_{O,OC} - m_O}{m_{O,\mathrm{OC}}} * 100\% \tag{42}$$

The ratio of the amount of oxygen that remains after the reduction cycle on the OC w_O can be compared with the X_S of the solid sample.

Where $O_{2\,OC}$ is the theoretical maximum possible amount of oxygen delivered by the OC, $O_{2\,fuel}$ is the amount of oxygen delivered by the fuel, $O_{2\,exhaust\,gas}$ is the oxygen concentration measured with the gas analysis and $O_{2\,steam}$ is the amount of oxygen that reacts with hydrogen from the fuel to form water vapor. For the calculation, following assumption have been made:

$$O_{2\,steam} = \frac{1}{2} n_H M_O = \frac{1}{2} \frac{m_{H,fuel} - m_{H\,in\,H_2EG} - m_{H\,in\,CH_4,EG}}{M_H} M_O = \tag{43}$$

$$= \frac{1}{2} \frac{m_{fuel} * x_{H,fuel} - n_{H_2} * 2 * M_H - n_{CH_4} * 4 * M_H}{M_H} M_O$$

6.4.2. Fuels

In a first experiment, methane and wood pellets have been used. In a second step pellets made of chicken manure have been used as solid fuel and introduced into the fluidized bed via the screw conveyor.

The used methane with a purity of 99,9 % has been delivered from a gas bottle and was introduced into the airbox, where it was mixed with steam before entering the fluidized bed through the gas distributor.

The wood pellets are certified according to "ENplus A1" and corresponds to DIN EN ISO 17225-2 and have following specification (see Table 20):

Table 20: Specification of wood pellets according DIN EN ISO 17225-2

Properties	**Unit**	**ENplus A1**
Diameter	mm	6 ±1
Lenght	mm	3.15 < L ≤ 40
Water content	wt%	≤ 10
Ash content	wt%	≤ 0.7
Mechan. Strength*	wt%	≥ 98.0
fine elements (< 3.15 mm)	wt%	≤ 1.0

Lower heating value H_U	kWh/kg	≥ 4.6
Bulk density	kg/m³	600 – 750
Additives*	wt%	≤ 2**
Nitrogen	wt%	≤ 0.3
Sulfur	wt%	≤ 0.04
Chlorine	wt%	≤ 0.02

* as delivered **The amount of additives in production is limited to 1.8w%, the amount of additives used after production (e.g., coating oils) is limited to 0.2w%

To reduce the variations of the screw conveyor feeding rate, only pellets, which already passed the screw once, have been used for the experiments. This kind of pretreatment homogenized the length of the pellets and leads to a constant dosing with fewer deviations (see section 6.3.2.3). Figure 79 shows the pretreated wood pellets which have been used for the experiments. The used chicken manure pellets are in similar size like the wood pellets. Because the mechanical strength and dosing deviation are much lower compared to the wood pellets, no pretreatment was necessary.

Figure 79: Pretreated wood pellets

6.4.3. First results and raw data evaluation

For the first series of experiments with solid fuels, 9.7 g of wood pellets per operating point were used. This amount of fuel was calculated to consume about 10 % of the oxygen available on the oxygen carrier, if full conversion is assumed. In the 120 kW pilot plant, approximately the same amount of oxygen is consumed from the OC in the FR per circulation.

The dosing velocity, bed temperature and the mass flow of steam for fluidizing in the reducing cycle were varied. The volume flow of air, which has been adjusted for fluidization in the oxidizing cycle, has no influence on the results but is also shown in Table 21.

Table 21: Process parameters of the operating points

Operating point	**Number of cycles**	**Dosing velocity**	**(set) Bed temperature**	**Mass flow steam**	**Volume flow air**
[-]	[-]	[g/min]	[°C]	[kg/h]	[Nm^3/h]
OP1	5	9.67	900	5.0	3.0
OP2	5	4.83	900	5.0	3.0
OP3	5	1.67	900	5.0	3.0
OP4	2	1.67	900	3.5	2.5
OP5	3	9.67	900	3.5	2.5
OP6	4	9.67	950	5.0	2.5
OP7	5	1.67	950	5.0	2.5
OP8	3	9.67	950	3.5	2.5

During all reducing cycles, a volume flow of 15 Nl/min of N_2 was fed into the reactor through the screw conveyor. The N_2 volume flow was not varied in the experiments. Each OP has been repeated 2-5 times to absorb fluctuations.

Figure 80 illustrates the temperature deviation during a cycle switch from reducing conditions to oxidizing conditions and vice versa. As can be seen, the airbox (grey line) and bed (black line) temperatures are almost constant, while the remaining temperatures (T_{outlet}, T_{top}, T_{middle}) slightly increase. Due to the large mass of the reactor and flange, even after a few hours of operation, there is still no steady state. Since the measurement points are downstream of the reaction zone, this has no influence on the results. The compared to the bed temperature by approximately 100°C lower airbox temperature can be attributed to the heat losses of the reactor because the airbox is only insulated and has no heating furnace.

The immediate changes in the temperatures at the reactor outlet, top and middle is because of changing fluid dynamic conditions due to the abruptly declining volume flow, when fluidizing with air instead of steam and additionally purge with the small amount of nitrogen. The reduced amount of air has been chosen according to operating experiences, because the exothermic reactions during the oxidizing cycle caused a strong heat release inside the bubbling bed, which can be slow downed with a decreased fluidization rate. To avoid excessive overshooting of the bed temperature, approx. 2 min before switching from reducing to oxidizing cycle the heat furnace of the reactor has been switched off manually. This explained the temperature decrease (approx. 5-8°C) in the bed temperature in Figure 80, shortly before switching the cycles. The airbox temperature is only slightly influenced by that. This manner of switching cycles was retained in the subsequent experiments.

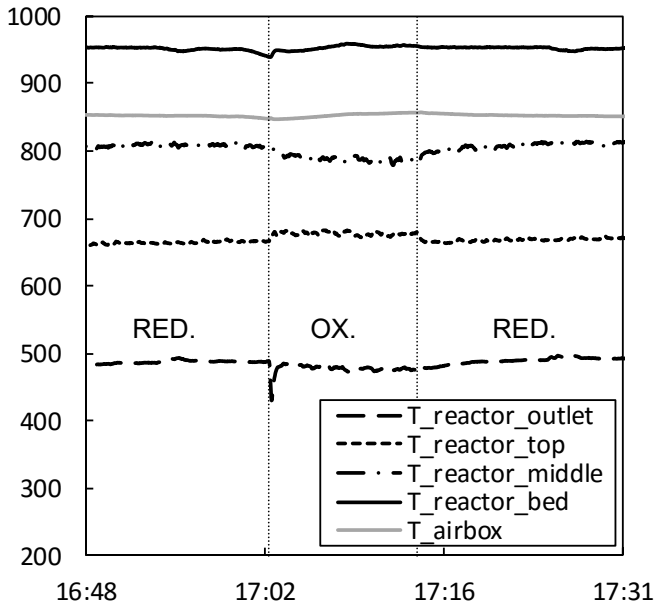

Figure 80: Temperature deviation during a cycle switch

Figure 81 shows the exhaust gas concentrations of five cycles of OP2. As can be seen, the fluidization was switched alternately from oxidation to reduction cycle. First the OC has been fully oxidized. An indicator for this is, when the OC is not further oxidized and the O_2 concentration of the depleted air from the reactor system reaches again 21 vol.%. Then, the fluidization was switched to steam and additionally N_2 was fed to the reactor via the screw conveyor. From the moment, when no more O_2 was measured in the exhaust gas, the fuel metering started and associated emissions were measured.

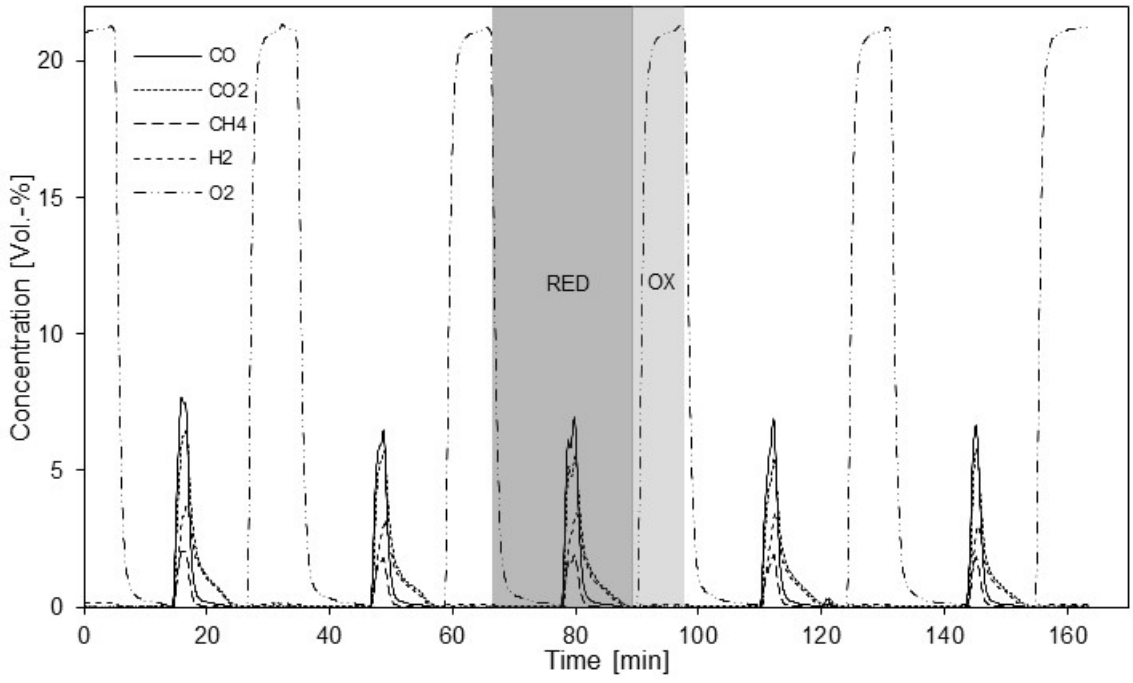

Figure 81: Exhaust gas concentration during five cycles of OP2

In order to expand the knowledge of how to operate the pilot plant, the fuel feeding rate was varied in the first step. Figure 81 shows the medium conveying speed of 4.83 g/min. The further experiment was then carried out at a higher and a lower conveying speed.

The following three diagrams in Figure 82 show cycles conducted with the same bed temperature and fluidization but with different fuel delivery rates. Even though in each case, the same amount of fuel (9.7 g) was fed into the reactor, the difference in flue gas composition is clearly visible. At a conveying speed of 9.67 g/min, the measured concentrations in the exhaust gas rise much faster than with slower dosing and also the peak values are different. The influence of the conveying speed on conversion will be discussed later in section 0.

Regardless of the fuel dosing velocity, the CO concentration consistently reaches the highest values, followed by the CO_2 concentration. The concentrations of H_2 and CH_4 are in a smaller range. It can be clearly seen, that the CO_2 and H_2 concentrations are the most enduring species in the exhaust gas. This is similar at all three dosing speeds and can be explained by the fact that after the first occurring pyrolysis is completed, in a second step the gasification of the leftover char inside the bed takes place. The resulting CO can still be oxidized to CO_2, while the gaseous H_2 cannot be oxidized in the freeboard above the fluidized bed due to a lack of present oxygen and therefore leaving the reactor unconverted.

At a conveying speed of 1.67 g/min, local extremes are clearly visible. These are due to the conveying behavior of the screw conveyor. The slowest conveying speed corresponds to approximately one revolution per minute and thus almost every emptying of the screw is seen in the gas analysis of the exhaust gas. The varying heights of the peaks can be attributed to the different degree of filling of the screw thread. At higher conveying speeds, this fluctuating promotion is no longer recognizable.

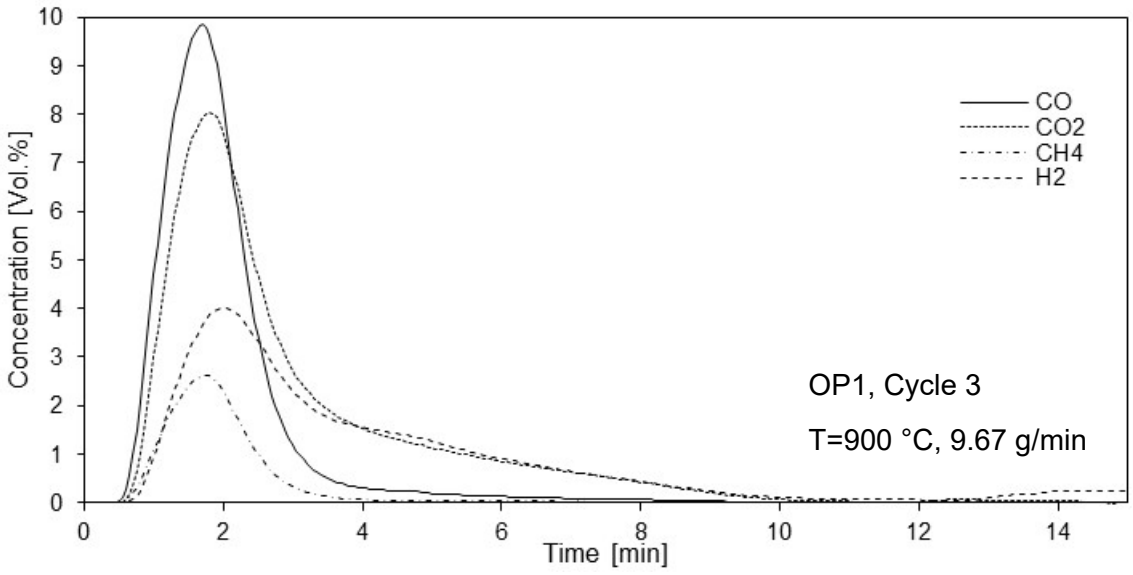

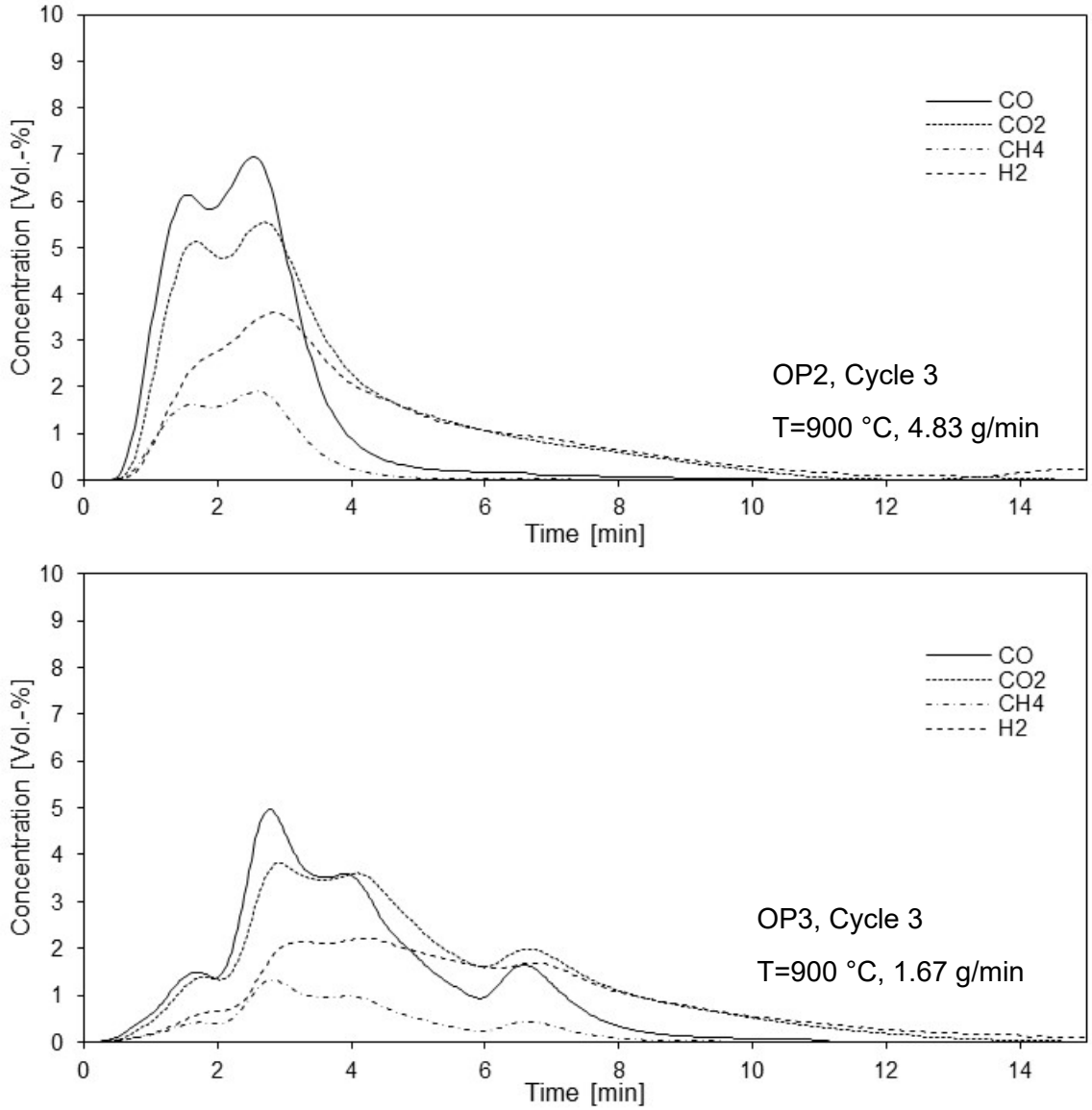

Figure 82: Exhaust gas concentration at three different dosing speeds

In Figure 83 the exhaust gas concentrations of the individual components of all five cycles of OP1 are superimposed. For further evaluation, the cyclical fluctuations have to be evaluated and a suitable method found, to create an average of the measured five cycles. In a first step, the mean value of each species was calculated and used for further investigations. At this OP the fit was satisfying due to the very low cyclical fluctuations.

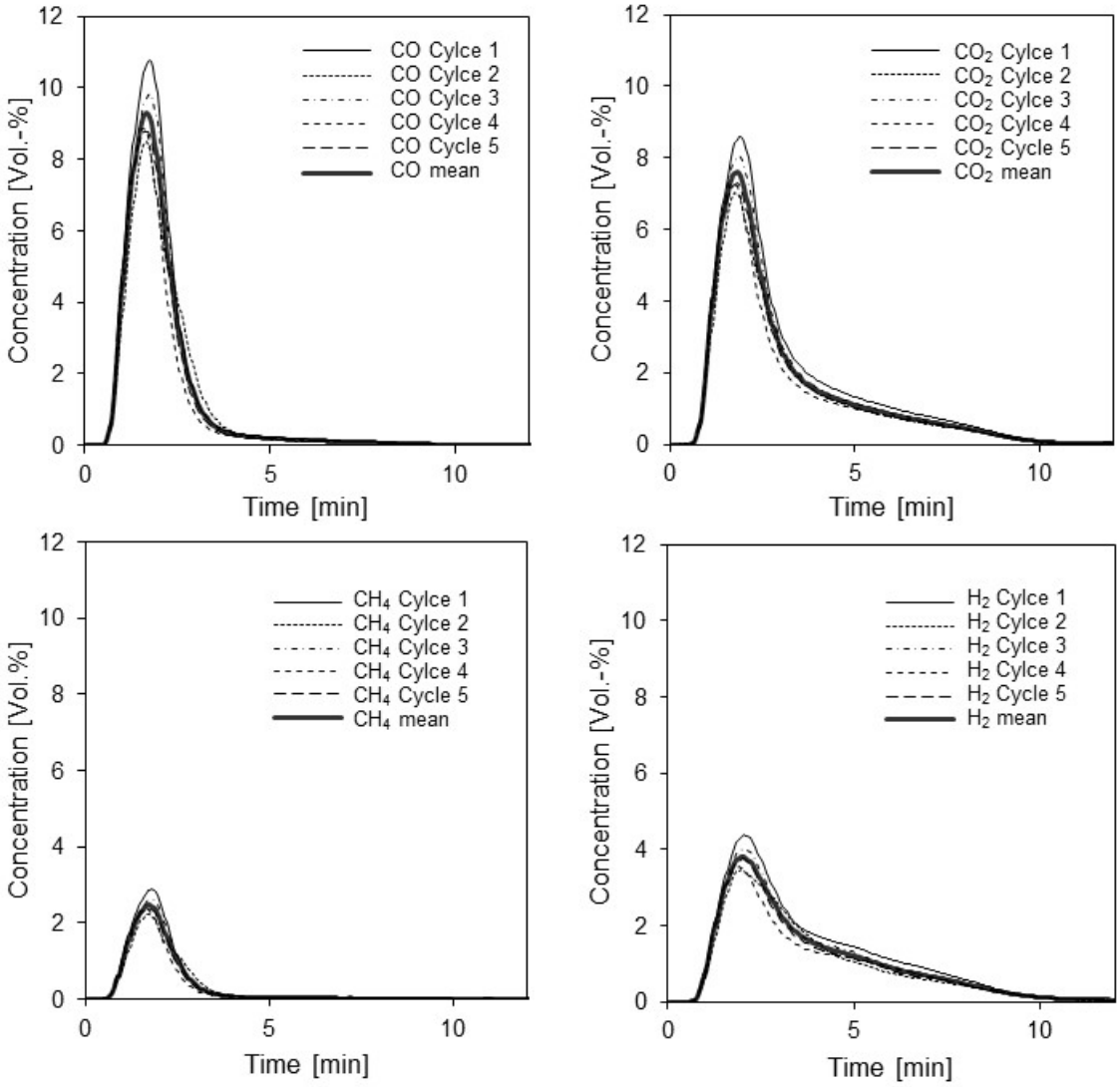

Figure 83: Exhaust gas concentration of the individual components of OP1 superimposed

There have also been operating points where the cyclical fluctuations were bigger and did not fit together properly. Especially at the very first attempt with wood pellets, there were clear differences between cycle 1 and cycle 2 and especially between cycle 3 and cycle 4 (see Figure 84). The area under the curve of cycle 3 is significantly larger than in cycle 4, thus the amount of CO is strongly different. Additional to the total mean value (5 values), the mean (3 values) of cycle 1, 2 and 5 is shown. The comparison of these two means shows that the deviations of the 3rd and 4th cycle have almost no influence on the mean. The deviations are thus equalized. The reason for the cyclical fluctuations are most likely the fuel dosing system. Depending on the position of the screw at the end of the conveying cycle, the thread pitch will be emptied or not. As a result, it may happen that in one cycle too little fuel is fed into the reactor, and in the subsequently cycle too much fuel is transported into the reactor. This makes it important to control the experiments manually and if a significantly cyclical fluctuations is determined, another repetition has to be performed to have at least three representative cycles per OP.

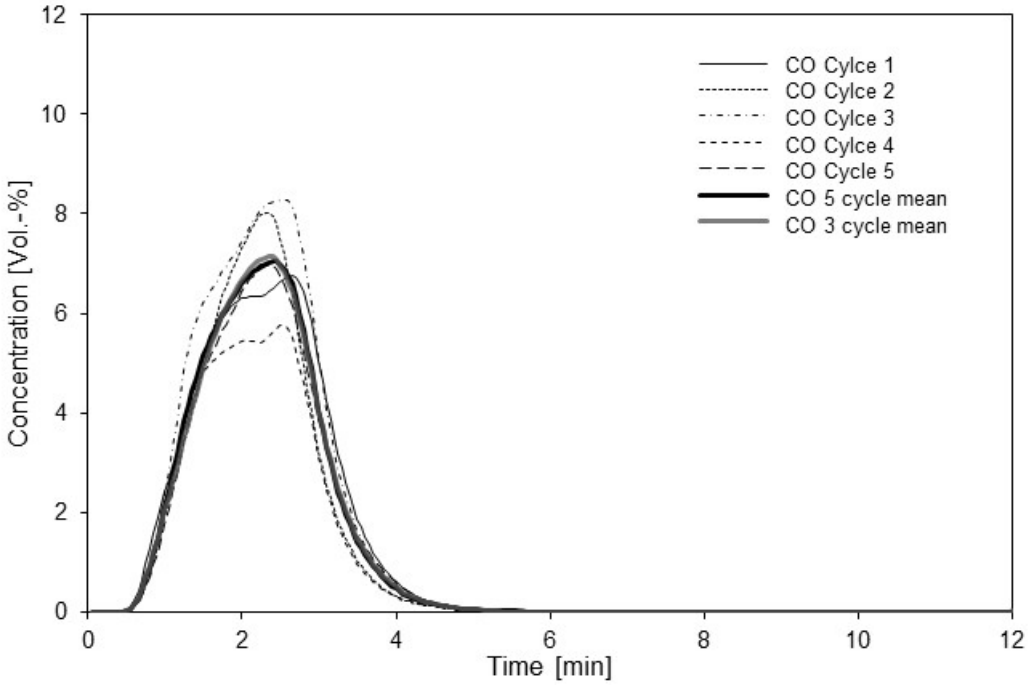

Figure 84: CO concentration using 9.7g wood pellets at 4.83g/min, 850°C bed temperature

Figure 85 shows the carbon mass fraction w_C in the exhaust gas in relation to the fuel dosing. The amount of fuel per cycle, either solid or gaseous has been constant. As can be seen in the left diagram, when using methane as fuel, w_C clearly increases with a faster dosing speed. But when looking on the exhaust gas composition in relation of carbon (Figure 86 left), an obvious CH_4 slip is visible in all three operating points. In terms of fuel conversion, the OP with the lowest methane dosing (0.88 Nl/min) has the best methane conversion, while the mass fraction of CO stays almost constant and the amount of CO_2 slightly decreases with increased dosing speed. It further appears that some of the methane is being lost due to a measurement error or converted into different hydrocarbon species that cannot be measured by the gas analyzer equipment. Due to this fact, the amount of lost or non-measurable gas components (named as "Rest") decreases at higher dosing speeds, which in turn leads to a lower carbon loss.

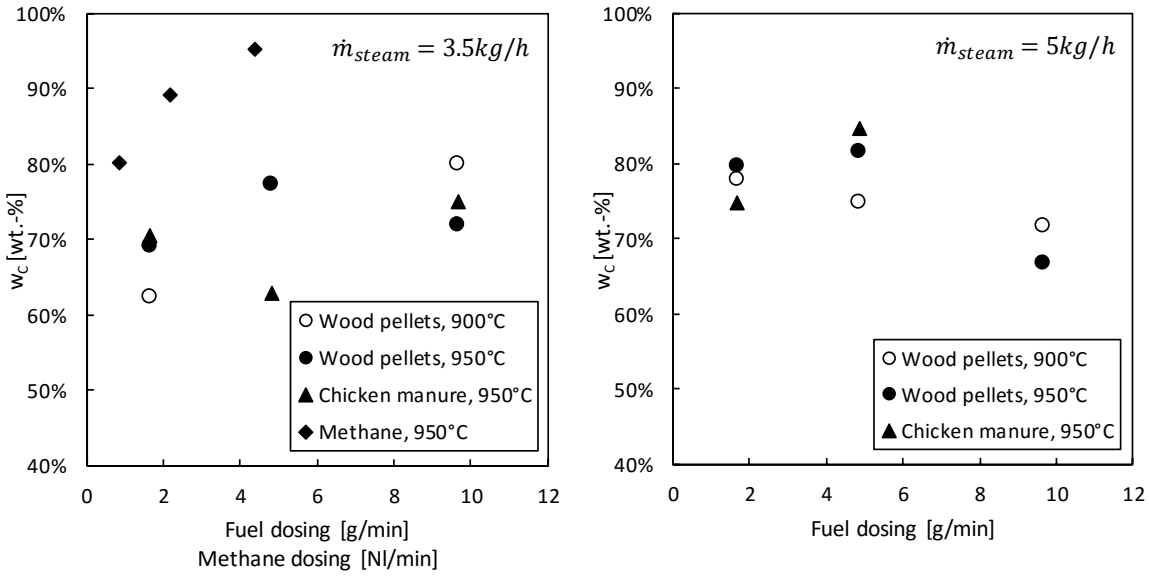

Figure 85: Mass fraction of carbon in the exhaust gas in relation to fuel dosing and fluidization rate, left with 3.5 kg/h and right with 5 kg/h steam

When using solid fuels, the correlations are much more complex. Due to the much higher amount of lost or unmeasurable gas components, the comparison of the carbon mass fraction in relation to the dosing speed at two different fluidization rates is difficult. Especially at higher dosing speeds and fluidization rates (Figure 85 right diagram), the uncertainties due to lost or indefinite gas components increases to over 30%.

In summary, it was found that approximately 70-80% of the carbon, fed to the reactor could be measured during the experiments. There are different errors that falsify the measurement results. In addition to the aforementioned fluctuations in fuel transportation, the assumption was made that beside CO, CO_2, CH_4, H_2, O_2 and N_2 the exhaust gas may consists of hydrocarbon species higher than C_1, but cannot be measured with the existing measuring equipment. In addition, unreacted char is discharged from the reactor, which is not recorded in terms of quantity and thus does not enter the balance either. All this has an impact on the carbon balance, making it difficult to make concrete statements.

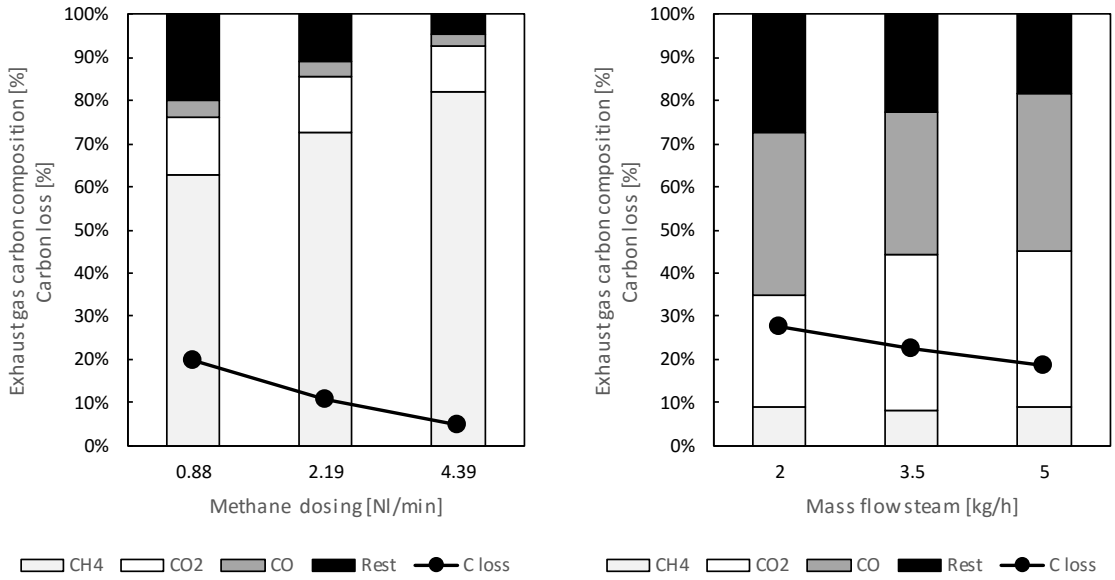

Figure 86: Exhaust gas carbon composition at 950°C bed temperature in relation to methane dosing at 3.5 kg/h steam fluidization rate (left) and with wood pellets as fuel at 4.83 g/min dosing speed in relation to the fluidization rate (right)

When using wood pellets as fuel, a complete different exhaust gas compositions occurs (Figure 86, right diagramm). The main component in the exhaust gas is CO, followed by CO_2, unknown components and very low mass fraction of methane. It should be noted that the amount of methane is almost identically at all three fluidization rates. With increasing fluidization rate, there is a shift to increased CO_2, almost constant CO and decreased amount of unknown components. Further it must be mentioned, that the relative amount of lost or unknown species is much higher when using solid fuels than with methane as fuel.

Figure 87 shows a comparison of carbon conversion at two different solid fuel dosing speeds in relation to the fluidization rate. When using wood pellets with a dosing speed of 4.83 g/min, an increased fuel conversion could be observed with increasing fluidization (left diagram). The associated exhaust gas carbon composition can be seen in the right diagram of Figure 86. A significantly more pronounced but similar behavior could be detected with chicken manure as fuel. At a higher dosing speed (Figure 87, right diagram) a contrary behavior could be observed with increasing fluidization rate.

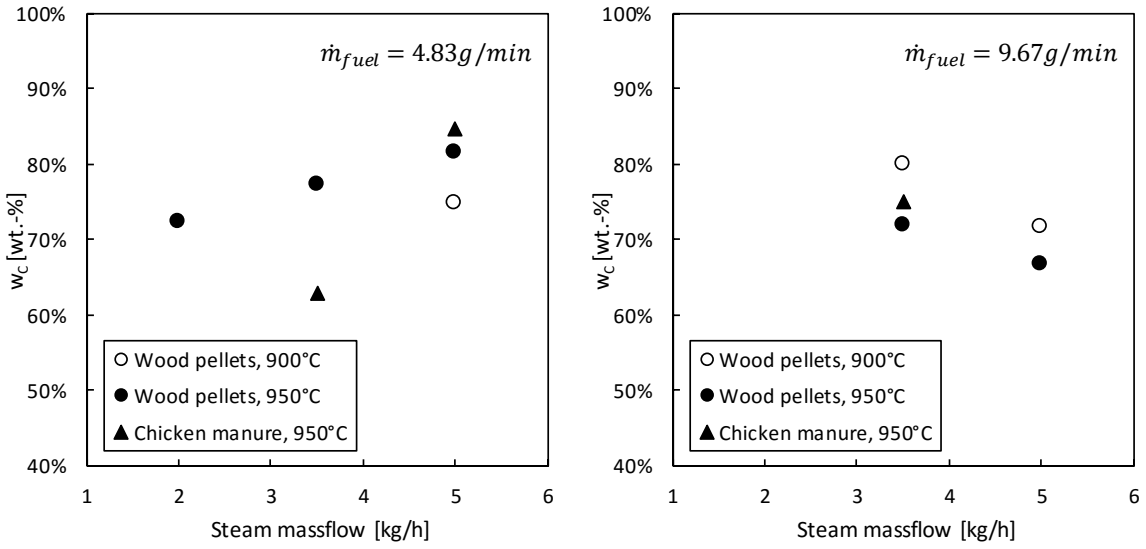

Figure 87: Converted carbon in relation to fluidization rate and dosing speed

When looking on an exemplarily carbon mass balance of all three tested kind of fuels (Figure 88) with very similar operating conditions, the amount of C loss varies from 11 % when using methane, up to 15 % with chicken manure and 18 % with wood pellets as solid fuel. A medium dosing speed, of 4.83 g/min and fluidization rate of 5 kg/h was chosen when using solid fuels. While with methane as fuel, a medium dosing speed of 2.19 Nl/min and a fluidization rate of 3.5 kg/h have been chosen for further investigations. Presumably, the mechanical strength of the solid fuel also has an impact on fuel conversion. While the wood pallets stay in shape even after passing one-time the screw conveyor, the chicken manure pellets are much softer and crush in the fuel dosing to very fine particles. The bigger surface and lower variations of the screw conveyor feeding rate of the chicken manure promotes the combustion in the fluidized bed substantially.

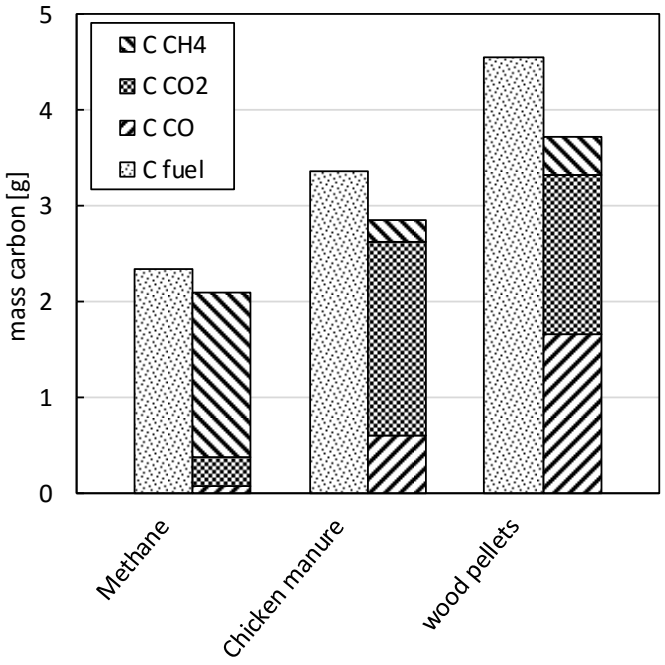

Figure 88: Carbon mass balance with ilmenite as OC using methane (left), chicken manure (middle) and wood pellets (right) as fuel

For a better understanding of the carbon mass balance, additional measurements of higher hydrocarbons during a few operating points have been conducted. Because the used Rosemount NGA 2000 infrared gas analyzer was only capable of measuring methane, carbon mono- and dioxide additionally a gas chromatograph (GC) have been used.

The used GC has a measuring interval of approximately 15 min, where a sample is drawn from the exhaust gas stream. Due to the fact, the batch operation is not continuous, the exhaust gas composition resembles a plug flow with a short transition zone when switching cycles or start/stop the fuel dosing. In combination with the punctual measurement of the GC, the timing of the measurement is crucial. For this reason the GC measurement have been manually timed in the first step to match the exhaust gas flow peak emissions. Figure 89 exemplarily shows an exhaust gas composition during a cycle using ilmenite as bed material and chicken manure pellets as fuel.

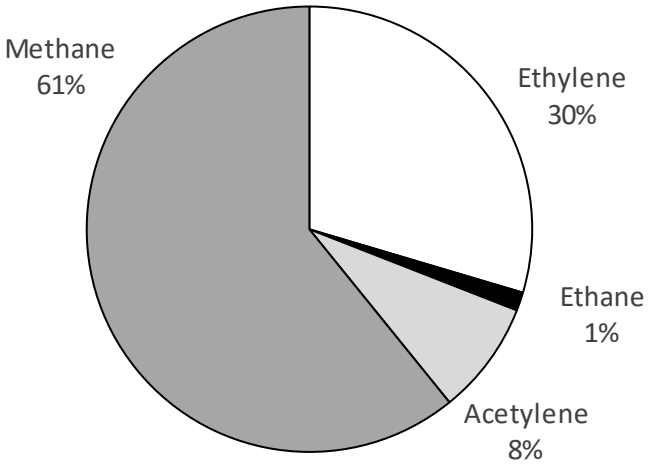

Figure 89: Exhaust gas composition of hydrocarbons higher than C_1 with ilmenite as OC and chicken manure as fuel

Beside methane, also species like ethylene, ethane and acetylene have been found, which is most likely a reason for the missing carbon. Approximately one third of the exhaust gas consist of hydrocarbons higher than C_1, the rest is methane. Because of the challenging and difficult GC sampling procedure, there were strong fluctuations in the measurements caused by imprecise sample timing in combination with variations of the fuel screw conveyor. This makes a comparison of different operating points not possible. In a further step a discontinuous gas analysis method have to be developed. Thus it should be possible to compare the results, especially the amount of methane, obtained from the GC with the online infrared gas analyzer to be able to make a statement about the measurement quality of the GC.

Further char could be found inside the filter box after five cycles of operation with an ilmenite OC and wood pellets as fuel (see Figure 90). Beside attrited bed material (grey particles) also an organic residue (black particles) has been found. Ignition loss measurements confirmed that it is unreacted coke. Due to the fact, the coke residues stuck to walls of the filter box and the piping, they did not occur continuously and made an exact balancing of carbon not possible.

Figure 90: Filter content after five cycles, using ilmenite as OC and wood pellets as fuel

In summary, it was found out that approximately 70-80% of the carbon fed to the reactor could be measured in the exhaust gas during the experiments. There are different errors that falsify the measurement results. In addition to the aforementioned fluctuations in fuel transportation, the assumption was made that beside CO, CO_2, CH_4, H_2, O_2 and N_2 the exhaust gas may consists of hydrocarbon species higher than C_1, but cannot be measured with the existing measuring equipment. With exemplarily conducted GC measurements, the assumptions could be confirmed. In addition, unreacted char is discharged from the reactor, which is not recorded in terms of quantity and thus does not enter the balance either.

Figure 91 compares the two determined values of degree of oxidation X_S and w_O. Both values are in the range of approximately 95 %, with only small differences. While the margin of error of X_S is negligible small, the deviation of w_O.is much higher due to the error chain of cyclical fluctuations and gas analysis. Nevertheless this means that solid sampling provides plausible results, and the mass of oxygen released by the OC is approximately equal to the mass of oxygen used for oxidation of the fuel.

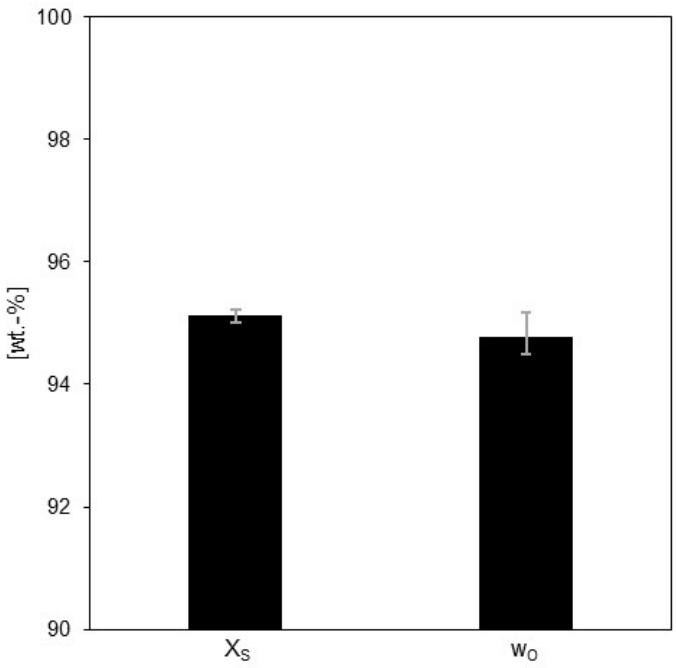

Figure 91: Comparison of X_S and w_O

Figure 92 shows the oxygen mass balance using ilmenite as bed material with 950°C in the reactor bed. The fluidization rate during the reducing cycle has been 5 kg/h of steam when using solid fuels and 3.5 kg/h of steam when using methane as fuel.

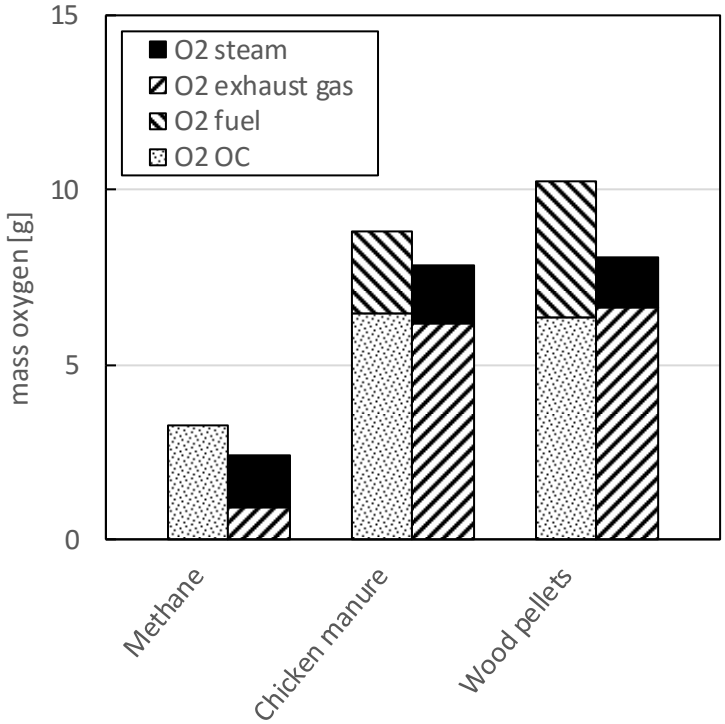

Figure 92: Oxygen mass balance at 950°C bed temperature with ilmenite as OC using methane (left), chicken manure (middle) and wood pellets (right) as fuel

The deviation in the oxygen mass balance varies between 25 % with methane, 11 % with chicken manure and 21 % when using wood pellets as fuel. It can be assumed, that a part is dissolved in rapeseed methyl ester filled impinger bottles, which are used as condensate trap, before entering the gas analysis equipment. Another part is most likely used for oxidation of metals in the ash and the formation of tar. Further an early release of oxygen of the OC cannot be excluded.

6.4.3.1. Solid Sampler

When sampling bed material from the reactor, this may lead to preferential removal of certain particle sizes and thus to a shift in the particle size distribution. Because the particles are expected to participate differently in the gas-solid reaction depending on the particle size and the associated specific surface area, a selectivity of the sampling device with respect to the particle size would result in a falsification of the solids samples analysis. In order to ensure that the drawn solid samples have a representative particle size distribution, a variation of sampling tests have been conducted during cold operation.

At four different operating conditions, samples have been compared with each other and with the initial bed material (Figure 93). All experiments have been conducted at ambient conditions and in fluidized state of operation.

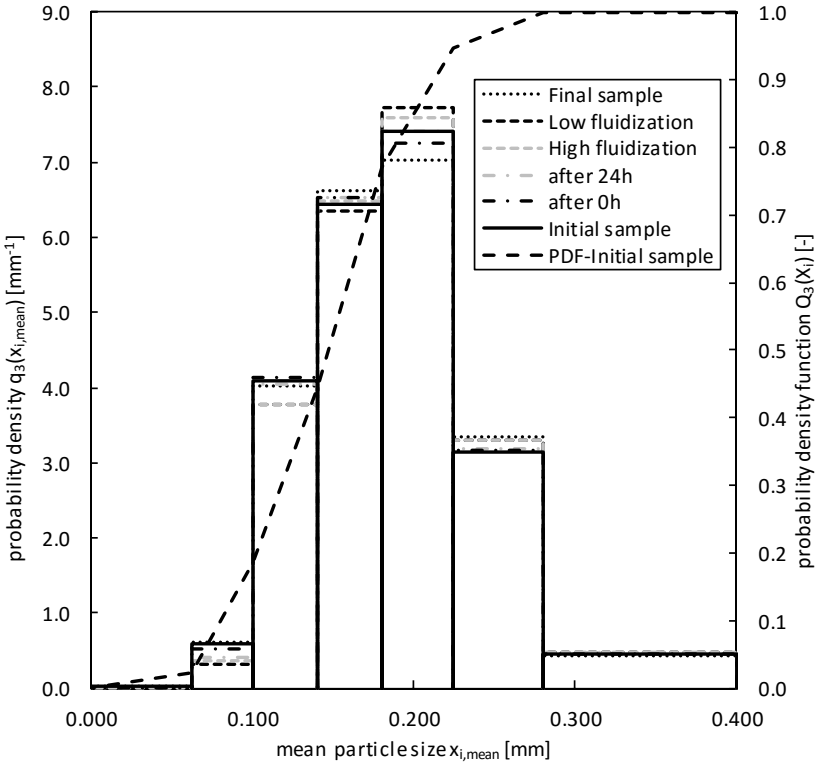

Figure 93: Comparison of probability density function at different states of operation with ilmenite as OC and under ambient conditions

The first sample have been drawn immediately after filling the reactor (after 0h) and the second sample after 24 hours of constant operation (after 24h). In a next step, the fluidization rate has been varied to verify the effect of bed expansion on the selectivity of the solid sampler. The third operating point have been conducted at minimum fluidization (low fluidization) and the fourth sample was drawn at a very high fluidization rate (high fluidization). As a comparison, samples of the fresh material (initial sample) and the used material after the test campaign (final sample) have been used.

It should be noted that only the probability density function of the initial sample is shown in Figure 93, because no significant differences during the campaign were determined. The designed solid sampling device shows no selectivity in particle size distribution. The maximum deviations of 2.88 % in particle size have been measured at low and high fluidization rates. *Table* 22 shows the total and percentage deviation during the campaign.

Table 22: Selectivity of solid sampling device

sample [-]	d_{SV} [mm]	Δd_{SV} [mm]	Δd_{SV} [%]
initial	0.139	-	-
after 0h	0.140	0.001	0.72
after 24h	0.141	0.002	1.44
low fluidization	0.143	0.004	2.88
high fluidization	0.143	0.004	2.88
final	0.139	0.000	0.00

A detailed study of the sampling behavior of the solid sampler, a detailed description of the operating conditions and the used measuring devices and the influence of the purge of the solid fuel dosing system can be found in the master thesis of Arlt [46].

Chapter Seven

7. Conclusions and outlook

7.1. Conclusions

In this thesis various CLC experiments have been conducted, using a 120 kW_{th} DFCB pilot plant for gaseous fuels and a new designed batch reactor, capable for gaseous as well as for solid fuels.

In the first test campaign, a perovskite based (C28) and copper based (Cu15) oxygen carrier were tested in the 120 kW_{th} CLC pilot plant using nitrogenous fuel impurities. Gaseous ammonia (NH_3) has been used as a model precursor into the natural gas fuel feed to investigate the pathways of nitrogen and formation of NO_X inside the DCFB system. The fuel N content varied between 0 and 0.63 wt% with C28 as OC and 0 and 1.4 wt% with Cu15 as OC.

Based on the experimental results, the following conclusions may be drawn:

- Constant long-term operation is possible with both oxygen carrier materials at the presence of significant amounts of fuel N.
- Fuel conversion and CO_2 yield remained unaffected from fuel N when using C28 or Cu15 as OC.
- Fuel conversion and CO_2 yield suffer from decreased bed inventory when using Cu15 as OC and shows a similar behavior as the experiments without nitrogen.
- The Cu15 OC is able to almost fully convert NH_3 (>99.8%), whereas NH_3 conversion was in the range of 70-75% for C28.
- The only emission of NO_X in the fuel reactor off gas was NO when using C28 as OC.
- The air reactor exhaust gas was not polluted with NO_X components at any time of the experiments
- Regeneration with the Cu15 material under CLC conditions after the ammonia feeding is possible but a clear statement cannot be made due to superimposed changes of bed inventory makeup and nitrogen dosing. With C28 as OC no immediate improvement have been observed.

Because of the character of this novel combustion technology with two separate exhaust gas streams, the emissions of a CLC process have to be evaluated individually for the AR and the FR. Further, it has to be discussed if there are better ways to quantify emissions, e.g., relating emissions to energy input instead of concentrations.

Nevertheless, with the right OC, the measured values are well below all limits in current regulations of NO_X emissions and available recommendations of NO_X concentrations for CO_2 purity in CCS. Thus, CLC has the potential not only to be an energy-efficient carbon capture technology but also to act as a highly efficient primary measure against NO_X emissions.

In a second campaign the same two oxygen carriers (C28 and Cu15) have been tested in the 120 kW_{th} CLC pilot plant using sulfurous fuel impurities. The experiments have been conducted dosing gaseous H_2S into the natural gas fuel feed. Thereby the H_2S concentration varied from 500 up to 2 000 ppmv at 800-850°C operating temperature and 73 kW_{th} of power input when using the copper based OC and from 100 up to 3 000 ppmv at 950°C operating temperature and 62 kWth of power input with the perovskite material. The experiments obtained following results:

- A stable operation of the CLC pilot plant with sulfur in the fuel feed was possible with Cu15 as OC. When using the C28 material no constant long-term operation was possible at the presence of significant large amounts of H_2S.
- Fuel conversion and CO_2 yield suffer from the presence of sulfur in the system with both OCs.
- With Cu15 as OC, the influence on CH_4 conversion and CO_2 yield is immediately visible but the worsening of the reactivity shows digressive behavior and only after a certain time, depending on the sulfur concentration, a stable operation could be achieved. Also an immediate worsening could be observed when using C28 as OC, but after an initial drop, the gradient of decrease returned to initial conditions.
- No H_2S slip was observed with both OCs.
- The only emission of sulfur is in the fuel reactor off gas as SO_2.
- During all operating points with H_2S in the fuel feed, the air reactor exhaust gas was not polluted with sulfur components at any time of the experiments.
- After switching off the H_2S feed, the CuO, γ-Al_2O_3 oxygen carrier starts to regenerate. The regeneration process with Cu15 as OC shows similarly slow behavior like the worsening of the reactivity. Regeneration under CLC conditions after the sulfur feeding is not possible for the C28 material. The fuel conversion remains at the same level as during the sulfur feeding period.
- Under long-lasting fluidized conditions without sulfur in the fuel feed, e.g. shut-down procedure, sulfur could be released from the C28 OC material.
- No effect on the degree of oxidation of the OCs could be observed.

Accumulation on the Cu15 particle could be detected on the surface as copper sulfide and as magnesium sulfide when using C28 as OC, but not quantified. Thereby the balance of in- and outbound sulfur shows inaccuracies during the experiment.

Figure 94 gives a visual illustration of the collected knowledge and properties of the different OCs, ranked from low (0) to high (5).

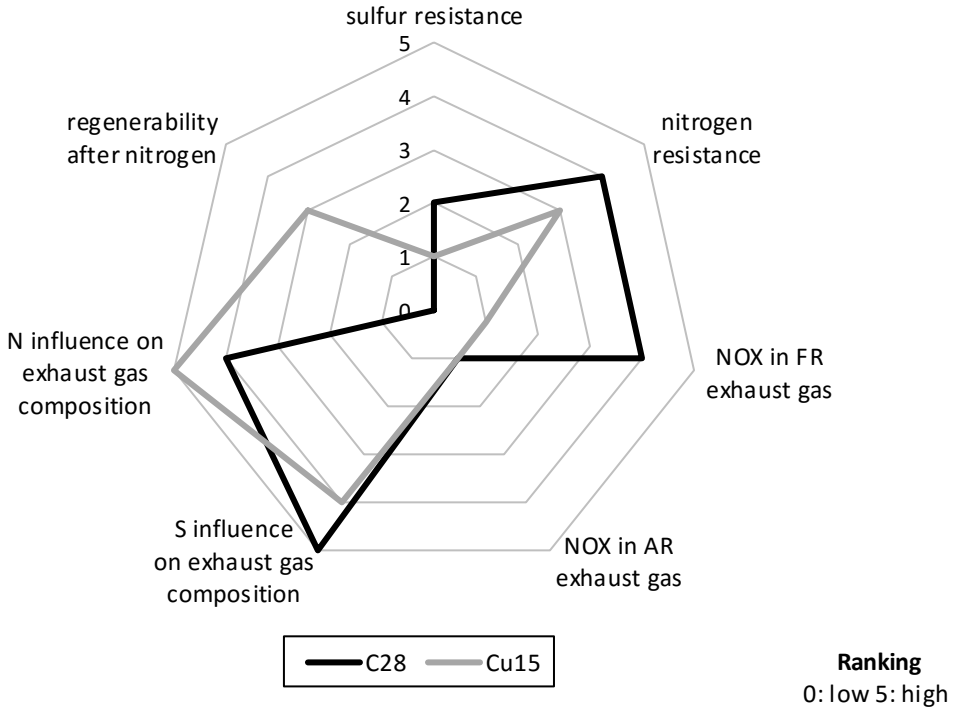

Figure 94: Effect of sulfur and nitrogen on process performance and emissions, 0: low, 5: high

The batch reactor system presented in this thesis offers the possibility to investigate various parameters and their influence on the CLC process. It is possible to test different oxygen carriers and to study their behavior with different solid or gaseous fuels. In particular, the study of solid fuels is of great importance, since biomass is traded as a potential fuel to reduce CO_2 emissions. The compact design of the system and especially of the reactor leads to relatively short duration of experiments. The heat-up times are significantly lower than with larger systems and thus the test stand is quickly ready for use. Furthermore, a novel semiautomatic solid sampling design allows to take samples during operation with low personnel expenses. The experiments conducted with the batch reactor represents a perfect supplement to the results obtained with the pilot plant. The possibility to use gaseous as well as solid fuels helps to enlarge the knowledge in the field of solid fuel CLC and conclusions from the small to the larger reactor system could be drawn. The developed method of measuring and evaluating the cycles shows satisfying and reproducible results.

The data obtained with the batch reactor show first trends but due to the small amount of operating points, only simple causal relationships and basic functions can be confirmed. Due to the loss of carbon in the exhaust gas, no clear carbon balance could be made. First measurements with a GC of gas samples confirmed the presence of the higher hydrocarbons such as ethylene, ethane and acetylene.

7.2. Outlook

In further investigations with the 120 kW pilot plant, the influence of important process parameters, e.g. temperature and/or Φ (OC-to-fuel ratio) could be observed with nitrogenous or sulfurous fuel impurities. Further experiments with actual nitrogenous or sulfurous fuels, without artificially added nitrogen or sulfur should be conducted to confirm the trends mentioned in this thesis.
Nevertheless it has to be mentioned here, that the results obtained with the batch reactor have to be seen as first achievements. In a next step, a method has to be developed, which is able to compare different kind of oxygen carriers and solid fuels (e.g. biomass) with each other and to transfer conclusions on the overall performance from the batch reactor to the DFCB system. To do so, a new method to measure higher hydrocarbons and tar in batch operation has to be developed. Without a nearly complete mass balance, the reproducibility, validity and comparability must be questioned. Once a discontinuous gas analysis method has been found, statistical methods for calculating the fuel conversion can be established.

For more meaningful results, a bunch of variations of conditions (e.g. fluidization rate, Xs, temperature), bed materials and solid fuel types have to be made. Furthermore the method of the gas analysis have to be refined.

After successful implementing an evaluation method with a suitable gas analysis, all kinds of new developed bed materials can be tested and benchmarked in a very short period of time and thus accelerate the development cycles for BioCLC and BECCS. Because as higher the TRL of BioCLC is, the more likely it will be selected by policy makers in future.

Chapter Eight

8. Nomenclature

8.1. Abbreviations

B2DS	beyond 2°C scenario of the IEA
2DS	2°C scenario of the IEA
4DS	4°C scenario of the IEA
AR	Air reactor
BECCS	Bio energy carbon capture and storage
Bio-CLC	Chemical looping combustion using biomass
CCS	Carbon capture and storage
CLC	Chemical looping combustion
CLOU	Chemical looping with oxygen uncoupling
DCFB	Dual circulating fluidized bed
DFB	Dual fluidized bed
EDS	X-ray spectroscopy
FB	Fixed bed
FIR	Flow indicating recording
FR	Fuel reactor
FTB	Fire tube burner
ICP-OES	inductively coupled plasma optical emission spectrometry
IEA	International Energy Agency
iG-CLC	In-situ gasification chemical looping combustion
IPCC	International Panel on Climate Change
LLS	Lower loop seal
MFC	Mass flow controller
OC	Oxigen Carrier
OP	Operating point
PIR	Pressure indicating recording
SEM	Scanning electron microscope
TI	Temperature indicating
TIR	Temperature indicating recording
TGA	Thermo-gravimetric analysis
ULS	Upper loop seal
XRD	X-ray diffraction
XRF	X-ray fluorescence

8.2. Symbols

a_0	Cross-sectional area of jet	[m²]
A_W	Cross-sectional area of the bed	[m²]
Ar	Archimedes number	[-]
d_0	Jet diameter	[m]
d_i	Diameter, particle size distribution	[m]
d_P	Sieve diameter	[m]
$d_P{}^*$	Dimensionless particle diameter	[m]
d_S	Surface-related diameter	[m]
d_{SV}	Sauter mean diameter	[m]
d_V	Volume-related diameter	[m]
d_W	Fluidized bed diameter	[m]
g	Gravity	[m/s²]
h_{mf}	Bed height at minimum fluidization	[m]
L_{down45}	Calculated jet penetration lenght	[m]
L_{exist}	Existing distance to nozzle plate	[m]
m_{Fuel}	Mass of solid fuel	[g]
$m_{C,EG}$	Mass of carbon in the exhaust gas	[g]
$m_{O,EG}$	Total mass of oxygen in the exhaust gas	[g]
m_{OC}	Mass of bed material (oxygen carrier)	[g]
$m_{O,OC}$	Total mass of oxygen on the oxygen carrier	[g]
M_i	Molar mass	[g/mol]
$\dot{m}_i$	Mass flow of species i	[kg/s]
m_{tot}	Total solids inventory of the pilot plant	[kg]
$\dot{n}_i$	Molar flow of species i	[mol/s]
N	Number of nozzle heads	[-]
$O_{2\,OC}$	Theor. maximum possible amount of oxygen on OC	[g]
$O_{2\,fuel}$	Amount of oxygen delivered by the fuel	[g]
$O_{2\,steam}$	Amount of oxygen delivered by the water vapor	[g]
OP	Operating point	[-]
P_{th}	Fuel power input based on the lower heating value	[W]
Δp_B	Bed pressure drop	[mbar]
Δp_V	Pressure drop of the gas distributor	[mbar]
Re	Reynolds number	[-]
R_O	Oxygen transport capacity	[kg/kg]
T_{AR}	Air reactor temperature	[°C]
T_{FR}	Fuel reactor temperature	[°C]
U	Superficial gas velocity	[m/s]
U^*	Dimensionless gas velocity	[-]
U_0	Velocity in the nozzle	[m/s]
U_c	Transition of bubbling and turbulent fluidized bed regime	[m/s]
U_{mf}	Minimum fluidization velocity	[m/s]
U_t	Terminal velocity	[m/s]
U_{se}	Transition of turbulent and fast fluidized bed regime	[m/s]

$\dot{V}_{D,N}$	Volume flow through a single nozzle at standard conditions	[Nm³/h]
$\dot{V}_{D,B}$	Volume flow through a single nozzle at operating conditions	[m³/h]
$\dot{V}_{ges,B}$	total volume flow inside the reactor at operating conditions	[m³/h]
$\dot{V}_i$	Volume flow of species i	[m³/h]
V_P	Volume of particle	[m³]
w_C	Mass fraction of carbon in the exhaust gas	[wt.-%]
w_O	Amount of oxygen on the OC	[-]
x_i	Frequency, particle size distribution	[-]
X_i	Conversion of species i	[-]
X_S	Degree of oxidation	[-]
y_i	Molar concentration of species i	[mol/mol]
ε	Void fraction	[-]
ε_{mf}	Void fraction at minimum fluidization	[-]
$\mu_{D,B}$	Dynamic viscosity steam	[Pa*s]
$\mu_{L,B}$	Dynamic viscosity air	[Pa*s]
ξ_D	Drag coefficient of the nozzle head	[-]
ρ_B	Bulk density	[kg/m³]
$\rho_{D,B}$	Operating density steam	[kg/m³]
ρ_g	Gas density	[kg/m³]
ρ_i	Density of species i	[kg/m³]
$\rho_{L,B}$	Operating density air	[kg/m³]
$\rho_{L,N}$	Density of air at standard conditions	[kg/m³]
ρ_P	Particle density	[kg/m³]
φ_i	Volume fraction of species i	[-]
ϕ	Shape factor	[-]
γ_{CO2}	CO_2-yield	[-]
λ	Air-to-fuel ratio	[-]

8.3. Indices

0	Related to initial
AR	Air reactor
B	Related to bulk or operating conditions
D	Related to nozzle of the gas distributor
down45	Related to the direction of 45° downwards
EG	Related to exhaust gas
exh	Related to exhaust stream of a reactor
exist	Related to existing
feed	Related to ingoing flow
FR	Fuel reactor
g	Related to gas
ges	Related to total
i	Related to species or inner
L	Related to air
mf	Related to minimum fluidization
N	Related to standard conditions
out	Related to outlet stream
p	Related to particle
s	Related to solid
S	Related to surface
stoichiometric	Stoichiometrically required amount
SV	Related to the ratio of surface to volume
th	Related to thermal
tot	Related to total
V	Related to volume or gas distributor
W	Related to fluidized bed

List of Tables

List of Figures

References

[1] Smil V. Energy transitions: history, requirements, prospects. ABC-CLIO; 2010.

[2] Team G. GISS Surface Temperature Analysis (GISTEMP), 2018.

[3] Hansen J, Ruedy R, Sato M, Lo K. Global surface temperature change. Reviews of Geophysics 2010;48(4).

[4] Tans PK, R.;. Trends in Atmospheric Carbon Dioxide. www.esrl.noaa.gov/gmd/ccgg/trends/: Scripps Institution of Oceanography; 2019.

[5] Joos F, Spahni R. Rates of change in natural and anthropogenic radiative forcing over the past 20,000 years. Proceedings of the National Academy of Sciences 2008;105(5):1425-30.

[6] Dlugokencky E, Tans P. NOAA/ESRL. J Geophys Res 2016;101:4115.

[7] Ciais P, Sabine C, Bala G, Bopp L, Brovkin V, Canadell J, et al. Carbon and other biogeochemical cycles. Climate change 2013: the physical science basis. Contribution of Working Group I to the Fifth Assessment Report of the Intergovernmental Panel on Climate Change. Cambridge University Press; 2014, p. 465-570.

[8] Le Quéré C, Andrew RM, Canadell JG, Sitch S, Korsbakken JI, Peters GP, et al. Global Carbon Budget 2016. 2016.

[9] Cook E. The flow of energy in an industrial society. Scientific American 1971;225(3):134-47.

[10] Key world energy statistics. International Energy Agency; 2018.

[11] World energs balances: Overview. International Energy Agency; 2018.

[12] Welt im Wandel: Gesellschaftsvertrag für eine große Transformation: Hauptgutachten. *WGBU.* Wissenschaftlicher Beirat der Bundesregierung Globale Umweltveränderungen; 2011.

[13] BP Statistical Review of World Energy June 2015, 2015. British Petroleum; 2015.

[14] Mercer. Quality of living ranking. https://mobilityexchange.mercer.com/Portals/0/Content/Rankings/rankings/qol2018l852963/index.html: Mercer; 2018.

[15] Mazur A, Rosa E. Energy and life-style. Science 1974;186(4164):607-10.

[16] Co-generation and Renewables: Solutions for a low-carbon energy future. OECD/International Energy Agency; 2011.

[17] Williamson P. Emissions reduction: scrutinize CO 2 removal methods. Nature News 2016;530(7589):153.

[18] Change IPoC. Global warming of 1.5°C. IPCC; 2018.

[19] Ellabban O, Abu-Rub H, Blaabjerg F. Renewable energy resources: Current status, future prospects and their enabling technology. Renewable and Sustainable Energy Reviews 2014;39:748-64.

[20] Energy Technology Perspectives 2012: Pathways to a Clean Energy System. OECD/International Energy Agency; 2012.

[21] Bull SR. Renewable energy today and tomorrow. Proceedings of the IEEE 2001;89(8):1216-26.

[22] Energy Technology Perspectives 2017 - Catalysing Energy Technology Transformation. International Energy Agency; 2017.

[23] Technology Roadmap Bioenergy for Heat and Power. OECD/International Energy Agency; 2012.
[24] Kirnbauer F. The impact of inorganic matter on the performance of dual fuidized bed biomass steam gasification plants. *Institute of Chemical, Environmental and Bioscience Engineering.* PhD. Vienna University of Technology; 2013.
[25] Xiaoding X, Moulijn J. Mitigation of CO2 by chemical conversion: Plausible chemical reactions and promising products. Energy & Fuels 1996;10(2):305-25.
[26] Metz B, Davidson O, De Coninck H. Carbon dioxide capture and storage: special report of the intergovernmental panel on climate change. Cambridge University Press; 2005.
[27] Keller DP, Lenton A, Littleton EW, Oschlies A, Scott V, Vaughan NE. The Effects of Carbon Dioxide Removal on the Carbon Cycle. Current Climate Change Reports 2018;4(3):250-65.
[28] Field CB. Climate change 2014–Impacts, adaptation and vulnerability: Regional aspects. Cambridge University Press; 2014.
[29] Paris Agreement, United nations framework convention on climate change. Paris, France; 2015.
[30] (UNEP) UNEP. The emissions gap report 2017. UNEP; 2017.
[31] Rogelj J, Fricko O, Meinshausen M, Krey V, Zilliacus JJJ, Riahi K. Understanding the origin of Paris Agreement emission uncertainties. Nature Communications 2017;8:15748.
[32] Sanderson BM, O'Neill BC, Tebaldi C. What would it take to achieve the Paris temperature targets? Geophysical Research Letters 2016;43(13):7133-42.
[33] Parson EA. Opinion: Climate policymakers and assessments must get serious about climate engineering. Proceedings of the National Academy of Sciences 2017;114(35):9227.
[34] Hansen J, Sato M, Kharecha P, von Schuckmann K, Beerling DJ, Cao J, et al. Young people's burden: requirement of negative CO2 emissions. Earth Syst Dynam 2017;8(3):577-616.
[35] Negative emission technologies: What role in meeting Paris Agreement targets? EASAC policy report 35. European Academies Science Advisory Concil (EASAC); 2018.
[36] Lyon RK, Cole JA. Unmixed combustion: an alternative to fire. Combustion and Flame 2000;121(1-2):249-61.
[37] Lewis W, Gilliland E, Sweeney M. Gasification of carbon-Metal oxides in a fluidized powder bed. Chem Eng Prog 1951;47(5):251-6.
[38] Ishida M, Zheng D, Akehata T. Evaluation of a chemical-looping-combustion power-generation system by graphic exergy analysis. Energy 1987;12(2):147-54.
[39] Ishida M, Jin H. A novel combustor based on chemical-looping reactions and its reaction kinetics. Journal of chemical engineering of Japan 1994;27(3):296-301.
[40] Bolland O. Fundamental thermodynamic approach for analyzing gas separation energy requirement for CO2-capture processes. *Proceedings of the 8th International Conference on greenhouse Gas Control Technologies (GHGT-8).* Trondheim, Norway; 2006.
[41] Mendiara T, Pérez-Astray A, Izquierdo MT, Abad A, de Diego LF, García-Labiano F, et al. Chemical Looping Combustion of different types of biomass in a 0.5kWth unit. Fuel 2018;211:868-75.

[42] Platform E. Biomass with CO2 capture and storage (Bio-CCS)-The way forward for Europe. Report; 2012.
[43] Technology roadmap: carbon capture and storage in industrial applications. *International Energy Agency, United Nations Industrial Development Organizations (UNIDO).* International Energy Agency; 2013.
[44] Wallquist L, Visschers VH, Siegrist M. Antecedents of risk and benefit perception of CCS. Enrgy Proced 2011;4:6288-91.
[45] Parzer S. Design, construction and commissioning of a lab scale fluidized bed unit for innovative processes. *Institute of Chemical, Environmental and Bioscience Engineering.* Master of Science. Vienna: Vienna University of Technology; 2018.
[46] Arlt S. Untersuchung zu Chemical Looping Combustion biogener Reststoffe an einer Laborwirbelschicht. *Institute of Chemical, Environmental and Bioscience Engineering.* Master of Science. Vienna: Vienna University of Technology; 2019.
[47] Fleiß B. Untersuchung zur Übertragbarkeit von Versuchsanlagen verschiedener Größe. *Institute of Chemical, Environmental and Bioscience Engineering.* Master of Science. Vienna: Vienna University of Technology; 2019.
[48] Energy Technology Perspectives: 495 Scenarios & Strategies To 2050. Publications 2010. International Energy Agency; 2010.
[49] Jerndal E, Mattisson T, Lyngfelt A. Thermal analysis of chemical-looping combustion. Chemical Engineering Research and Design 2006;84(9):795-806.
[50] Jerndal E, Mattisson T, Thijs I, Snijkers F, Lyngfelt A. NiO particles with Ca and Mg based additives produced by spray-drying as oxygen carriers for chemical-looping combustion. Enrgy Proced 2009;1(1):479-86.
[51] Lyngfelt A. Oxygen Carriers for Chemical Looping Combustion - 4 000 h of Operational Experience. Oil & Gas Science and Technology - Revue d'IFP Energies nouvelles 2011;66(2):161-72.
[52] Adánez J, Abad A, García-Labiano F, Gayán P, de Diego LF. Progress in Chemical-Looping Combustion and Reforming Technologies. Progress in Energy and Combustion Science 2012;38(2):215-82.
[53] Jerndal E, Mattisson T, Thijs I, Snijkers F, Lyngfelt A. NiO particles with Ca and Mg based additives produced by spray- drying as oxygen carriers for chemical-looping combustion. Enrgy Proced 2009;1(1):479–86.
[54] Cho P, Mattisson T, Lyngfelt A. Comparison of iron-, nickel-, copper- and manganese-based oxygen carriers for chemical-looping combustion. Fuel 2004;83(9):1215–25.
[55] Mayer K, Penthor S, Pröll T, Hofbauer H. The different demands of oxygen carriers on the reactor system of a CLC plant – Results of oxygen carrier testing in a 120kWth pilot plant. Applied Energy 2015;157:323-9.
[56] Mayer K, Piesenberger S, Penthor S, Pröll T, Hofbauer H. Chemical Looping Combustion Using Two Different Perovskite Based Oxygen Carriers: A Pilot Study. Energy Technology 2018.
[57] Adanez J, Abad A, Garcia-Labiano F, Gayan P, Luis F. Progress in chemical-looping combustion and reforming technologies. Progress in energy and combustion science 2012;38(2):215-82.
[58] Lyngfelt A. Oxygen carriers for chemical looping combustion-4 000 h of operational experience. Oil & Gas Science and Technology–Revue d'IFP Energies nouvelles 2011;66(2):161-72.

[59] Adánez J, Abad A, Mendiara T, Gayán P, de Diego LF, García-Labiano F. Chemical looping combustion of solid fuels. Progress in Energy and Combustion Science 2018;65:6-66.
[60] Leion H, Mattisson T, Lyngfelt A. Using chemical-looping with oxygen uncoupling (CLOU) for combustion of six different solid fuels. Enrgy Proced 2009;1(1):447-53.
[61] Pröll T, Schöny G, Mayer K, Hofbauer H. The impact of reaction mechanism on the design of continuously operating CLC systems–nickel based versus copper based oxygen carriers. *Proceedings of the 2nd International Conference on Chemical Looping, Darmstadt, Germany.* 2012.
[62] Adánez-Rubio I, Arjmand M, Leion H, Gayán P, Abad A, Mattisson T, et al. Investigation of Combined Supports for Cu-Based Oxygen Carriers for Chemical-Looping with Oxygen Uncoupling (CLOU). Energy & Fuels 2013;27(7):3918-27.
[63] Penthor S. Chemical looping combustion of biomass for below zero emission energy production. *Institute of Chemical, Environmental and Bioscience Engineering.* PhD. Vienna University of Technology; 2015.
[64] de Diego LF, Gayán P, García-Labiano F, Celaya J, Abad A, Adánez J. Impregnated CuO/Al2O3Oxygen Carriers for Chemical-Looping Combustion: Avoiding Fluidized Bed Agglomeration. Energy & Fuels 2005;19(5):1850-6.
[65] Wen Y-y, Li Z-s, Xu L, Cai N-s. Experimental Study of Natural Cu Ore Particles as Oxygen Carriers in Chemical Looping with Oxygen Uncoupling (CLOU). Energy & Fuels 2012;26(6):3919-27.
[66] Adánez J, Gayán P, Celaya J, de Diego LF, García-Labiano F, Abad A. Chemical Looping Combustion in a 10 kWth Prototype Using a CuO/Al2O3 Oxygen Carrier: Effect of Operating Conditions on Methane Combustion. Industrial & Engineering Chemistry Research 2006;45(17):6075-80.
[67] Pachler RF, Mayer K, Penthor S, Kollerits M, Hofbauer H. Fate of sulfur in chemical looping combustion of gaseous fuels using a copper-based oxygen carrier. International Journal of Greenhouse Gas Control 2018;71:86-94.
[68] Penthor S, Zerobin F, Mayer K, Pröll T, Hofbauer H. Investigation of the performance of a copper based oxygen carrier for chemical looping combustion in a 120kW pilot plant for gaseous fuels. Applied Energy 2015;145:52-9.
[69] Langørgen Ø, Saanum I, Haugen NEL. Chemical Looping Combustion of Methane Using a Copper-based Oxygen Carrier in a 150 kW Reactor System. Enrgy Proced 2017;114:352-60.
[70] Cabello A, Scullard A, Williams G, Matthey J, Gayán P, de Diego L, et al. Scale-up of CLC oxygen carriers for gaseous fuels. 2016.
[71] Cabello A, Gayán P, Abad A, de Diego LF, García-Labiano F, Izquierdo MT, et al. Long-lasting Cu-based oxygen carrier material for industrial scale in Chemical Looping Combustion. International Journal of Greenhouse Gas Control 2016;52:120-9.
[72] Arjmand M, Azad A-M, Leion H, Lyngfelt A, Mattisson T. Prospects of Al2O3 and MgAl2O4-supported CuO oxygen carriers in chemical-looping combustion (CLC) and chemical-looping with oxygen uncoupling (CLOU). Energy & Fuels 2011;25(11):5493-502.
[73] Imtiaz Q, Broda M, Müller CR. Structure–property relationship of co-precipitated Cu-rich, Al2O3- or MgAl2O4-stabilized oxygen carriers for chemical looping with oxygen uncoupling (CLOU). Applied Energy 2014;119:557-65.

[74] Gayán P, Forero CR, Abad A, de Diego LF, García-Labiano F, Adánez J. Effect of Support on the Behavior of Cu-Based Oxygen Carriers during Long-Term CLC Operation at Temperatures above 1073 K. Energy & Fuels 2011;25(3):1316-26.
[75] Tian X, Wei Y, Zhao H. Using a hierarchically-structured CuO@TiO2-Al2O3 oxygen carrier for chemical looping air separation in a paralleled fluidized bed reactor. Chemical Engineering Journal 2018;334:611-8.
[76] Arjmand M, Azad A-M, Leion H, Mattisson T, Lyngfelt A. Evaluation of CuAl2O4 as an oxygen carrier in chemical-looping combustion. Industrial & Engineering Chemistry Research 2012;51(43):13924-34.
[77] Zhou Z, Han L, Nordness O, Bollas GM. Continuous regime of chemical-looping combustion (CLC) and chemical-looping with oxygen uncoupling (CLOU) reactivity of CuO oxygen carriers. Applied Catalysis B: Environmental 2015;166-167:132-44.
[78] García-Labiano F, Gayán P, Adánez J, De Diego LF, Forero CR. Solid Waste Management of a Chemical-Looping Combustion Plant using Cu-Based Oxygen Carriers. Environmental Science & Technology 2007;41(16):5882-7.
[79] Peña MA, Fierro JLG. Chemical Structures and Performance of Perovskite Oxides. Chemical Reviews 2001;101(7):1981-2018.
[80] Sakata K, Nakamura T, Misono M, Yoneda Y. Reduction-Oxidation Mechanism of Oxide Catalysts. Oxygen Diffusion during Redox Cycles. Chemistry Letters 1979;8(3):273-6.
[81] Voorhoeve RJH. 5 - Perovskite-Related Oxides as Oxidation—Reduction Catalysts. In: Burton JJ, Garten RL, editors. Advanced Materials in Catalysis. Academic Press; 1977, p. 129-80.
[82] Rydén M, Lyngfelt A, Mattisson T, Chen D, Holmen A, Bjørgum E. Novel oxygen-carrier materials for chemical-looping combustion and chemical-looping reforming; LaxSr1−xFeyCo1−yO3−δ perovskites and mixed-metal oxides of NiO, Fe2O3 and Mn3O4. International Journal of Greenhouse Gas Control 2008;2(1):21-36.
[83] Bakken E, Norby T, Stølen S. Nonstoichiometry and reductive decomposition of CaMnO3−δ. Solid State Ionics 2005;176(1):217-23.
[84] Bakken E, Boerio-Goates J, Grande T, Hovde B, Norby T, Rørmark L, et al. Entropy of oxidation and redox energetics of CaMnO3−δ. Solid State Ionics 2005;176(29):2261-7.
[85] Leonidova EI, Leonidov IA, Patrakeev MV, Kozhevnikov VL. Oxygen non-stoichiometry, high-temperature properties, and phase diagram of CaMnO3–δ. Journal of Solid State Electrochemistry 2011;15(5):1071-5.
[86] Jing D, Mattisson T, Leion H, Ryd, #xe9, n M, et al. Examination of Perovskite Structure CaMnO3-δ with MgO Addition as Oxygen Carrier for Chemical Looping with Oxygen Uncoupling Using Methane and Syngas. International Journal of Chemical Engineering 2013;2013:16.
[87] Hallberg P, Jing D, Rydén M, Mattisson T, Lyngfelt A. Chemical Looping Combustion and Chemical Looping with Oxygen Uncoupling Experiments in a Batch Reactor Using Spray-Dried CaMn1–xMxO3–δ (M = Ti, Fe, Mg) Particles as Oxygen Carriers. Energy & Fuels 2013;27(3):1473-81.
[88] Rydén M, Lyngfelt A, Mattisson T. CaMn0.875Ti0.125O3 as oxygen carrier for chemical-looping combustion with oxygen uncoupling (CLOU)—Experiments in a

continuously operating fluidized-bed reactor system. International Journal of Greenhouse Gas Control 2011;5(2):356-66.
[89] Berguerand N, Lyngfelt A. Design and operation of a 10kWth chemical-looping combustor for solid fuels – Testing with South African coal. Fuel 2008;87(12):2713-26.
[90] Berguerand N, Lyngfelt A. The use of petroleum coke as fuel in a 10kWth chemical-looping combustor. International Journal of Greenhouse Gas Control 2008;2(2):169-79.
[91] Leion H, Mattisson T, Lyngfelt A. Solid fuels in chemical-looping combustion. International Journal of Greenhouse Gas Control 2008;2(2):180-93.
[92] Berguerand N, Lyngfelt A. Chemical-Looping Combustion of Petroleum Coke Using Ilmenite in a 10 kWth Unit–High-Temperature Operation. Energy & Fuels 2009;23(10):5257-68.
[93] Berguerand N, Lyngfelt A. Operation in a 10 kWth chemical-looping combustor for solid fuel—Testing with a Mexican petroleum coke. Enrgy Proced 2009;1(1):407-14.
[94] Thon A, Kramp M, Hartge E-U, Heinrich S, Werther J. Operational experience with a system of coupled fluidized beds for chemical looping combustion of solid fuels using ilmenite as oxygen carrier. Applied Energy 2014;118:309-17.
[95] Markström P, Linderholm C, Lyngfelt A. Operation of a 100kW chemical-looping combustor with Mexican petroleum coke and Cerrejón coal. Applied Energy 2014;113:1830-5.
[96] Berguerand N, Lyngfelt A. Batch testing of solid fuels with ilmenite in a 10 kWth chemical-looping combustor. Fuel 2010;89(8):1749-62.
[97] Linderholm C, Schmitz M, Knutsson P, Lyngfelt A. Chemical-looping combustion in a 100-kW unit using a mixture of ilmenite and manganese ore as oxygen carrier. Fuel 2016;166:533-42.
[98] Abad A, Mendiara T, Gayán P, García-Labiano F, de Diego LF, Bueno JA, et al. Comparative Evaluation of the Performance of Coal Combustion in 0.5 and 50 kWth Chemical Looping Combustion Units with Ilmenite, Redmud or Iron Ore as Oxygen Carrier. Enrgy Proced 2017;114:285-301.
[99] Berdugo Vilches T, Marinkovic J, Seemann M, Thunman H. Comparing Active Bed Materials in a Dual Fluidized Bed Biomass Gasifier: Olivine, Bauxite, Quartz-Sand, and Ilmenite. Energy & Fuels 2016;30(6):4848-57.
[100] Tan Y, Sun Z, Cabello A, Lu DY, Hughes RW. Effects of H2S on the Reactivity of Ilmenite Ore as Chemical Looping Combustion Oxygen Carrier with Methane as Fuel. Energy & Fuels 2019;33(1):585-94.
[101] Ströhle J, Orth M, Epple B. Design and operation of a 1MWth chemical looping plant. Applied Energy 2014;113:1490-5.
[102] Ströhle J, Orth M, Epple B. Chemical looping combustion of hard coal in a 1 MWth pilot plant using ilmenite as oxygen carrier. Applied Energy 2015;157:288-94.
[103] Rydén M, Lyngfelt A, Langørgen Ø, Larring Y, Brink A, Teir S, et al. Negative CO2 Emissions with Chemical-Looping Combustion of Biomass – A Nordic Energy Research Flagship Project. Enrgy Proced 2017;114:6074-82.
[104] Borowiec K, Rosenqvist T. Phase relations and oxidation studies in the system Fe-Fe2O3-TiO2 AT 700-1000°C. Scandinavian Journal of Metallurgy 1981;10(5):217-24.

[105] Nell J. An overview of the phase-chemistry involved in the production of high-titanium slag from ilmenite feedstock. Journal of the South African Institute of Mining and Metallurgy(South Africa) 2000;100(1):35-44.
[106] Abad A, Adánez J, Cuadrat A, García-Labiano F, Gayán P, de Diego LF. Kinetics of redox reactions of ilmenite for chemical-looping combustion. Chemical Engineering Science 2011;66(4):689-702.
[107] Hamers HP, Gallucci F, Cobden PD, Kimball E, van Sint Annaland M. CLC in packed beds using syngas and CuO/Al2O3: Model description and experimental validation. Applied Energy 2014;119:163-72.
[108] Kimball E, Lambert A, Fossdal A, Leenman R, Comte E, van den Bos W, et al. Reactor choices for chemical looping combustion (CLC)—Dependencies on materials characteristics. Enrgy Proced 2013;37:567-74.
[109] Fernández J, Abanades J. Conceptual design of a Ni-based chemical looping combustion process using fixed-beds. Applied Energy 2014;135:309-19.
[110] Dahl IM, Bakken E, Larring Y, Spjelkavik AI, Håkonsen SF, Blom R. On the development of novel reactor concepts for chemical looping combustion. Enrgy Proced 2009;1(1):1513-9.
[111] Abad A, Adánez J, García-Labiano F, Luis F, Gayán P, Celaya J. Mapping of the range of operational conditions for Cu-, Fe-, and Ni-based oxygen carriers in chemical-looping combustion. Chemical Engineering Science 2007;62(1-2):533-49.
[112] Kolbitsch P, Pröll T, Bolhar-Nordenkampf J, Hofbauer H. Design of a Chemical Looping Combustor using a Dual Circulating Fluidized Bed (DCFB) Reactor System. Chemical Engineering & Technology 2009;32(3):398-403.
[113] Pröll T, Kolbitsch P, Bolhàr-Nordenkampf J, Hofbauer H. A novel dual circulating fluidized bed system for chemical looping processes. AIChE Journal 2009;55(12):3255–66.
[114] Bolhàr-Nordenkampf J, Pröll T, Kolbitsch P, Hofbauer H. Performance of a NiO-based oxygen carrier for chemical looping combustion and reforming in a 120 kW unit. Energy Procedia 2009;1(1):19–25.
[115] Kolbitsch P, Bolhàr-Nordenkampf J, Pröll T, Hofbauer H. Operating experience with chemical looping combustion in a 120kW dual circulating fluidized bed (DCFB) unit. International Journal of Greenhouse Gas Control 2010;4(2):180–5.
[116] Penthor S, Mayer K, Kern S, Kitzler H, Wöss D, Pröll T, et al. Chemical-looping combustion of raw syngas from biomass steam gasification – Coupled operation of two dual fluidized bed pilot plants. Fuel 2014;127(0):178-85.
[117] Penthor S, Mayer K, Pröll T, Hofbauer H. Experimental Study of the Path of Nitrogen in Chemical Looping Combustion Using a Nickel-Based Oxygen Carrier. Energy & Fuels 2014;28(10):6604-9.
[118] Mayer K, Piesenberger S, Penthor S, Pröll T, Hofbauer H. Chemical Looping Combustion Using Two Different Perovskite Based Oxygen Carriers: A Pilot Study. Energy Technology 2018;6(12):2333-43.
[119] Mayer K, Schanz E, Pröll T, Hofbauer H. Performance of an iron based oxygen carrier in a 120 kWth chemical looping combustion pilot plant. Fuel 2018;217:561-9.
[120] Pröll T, Hofbauer H. A dual fluidized bed system for chemical looping combustion of solid fuels. na; 2010.

[121] Leion H, Mattisson T, Lyngfelt A. The use of petroleum coke as fuel in chemical-looping combustion. Fuel 2007;86(12-13):1947-58.
[122] Penthor S, Pröll T, Hofbauer H. Chemical-looping combustion using biomass as fuel. na; 2011.
[123] Reed T. Biomass gasification principles and technology, noyes data corporation. Part Ridge, New Jersey, US A 1981.
[124] Lyngfelt A. Chemical-looping combustion of solid fuels – Status of development. Applied Energy 2014;113:1869-73.
[125] Lyngfelt A, Linderholm C. Chemical-Looping Combustion of Solid Fuels – Status and Recent Progress. Enrgy Proced 2017;114:371-86.
[126] Mendiara T, Abad A, De Diego L, García-Labiano F, Gayán P, Adánez J. Biomass combustion in a CLC system using an iron ore as an oxygen carrier. International Journal of Greenhouse Gas Control 2013;19:322-30.
[127] Mendiara T, Gayán P, García-Labiano F, de Diego LF, Pérez-Astray A, Izquierdo MT, et al. Chemical Looping Combustion of Biomass: An Approach to BECCS. Enrgy Proced 2017;114:6021-9.
[128] Mendiara T, García-Labiano F, Abad A, Gayán P, de Diego LF, Izquierdo MT, et al. Negative CO2 emissions through the use of biofuels in chemical looping technology: A review. Applied Energy 2018;232:657-84.
[129] Adánez-Rubio I, Abad A, Gayán P, de Diego LF, García-Labiano F, Adánez J. Biomass combustion with CO2 capture by chemical looping with oxygen uncoupling (CLOU). Fuel Processing Technology 2014;124:104-14.
[130] Adánez-Rubio I, Pérez-Astray A, Mendiara T, Izquierdo MT, Abad A, Gayán P, et al. Chemical looping combustion of biomass: CLOU experiments with a Cu-Mn mixed oxide. Fuel Processing Technology 2018;172:179-86.
[131] Schmitz M, Linderholm CJ. Performance of calcium manganate as oxygen carrier in chemical looping combustion of biochar in a 10 kW pilot. Applied Energy 2016;169:729-37.
[132] Schmitz M, Linderholm C. Chemical looping combustion of biomass in 10- and 100-kW pilots – Analysis of conversion and lifetime using a sintered manganese ore. Fuel 2018;231:73-84.
[133] Shen L, Wu J, Xiao J, Song Q, Xiao R. Chemical-looping combustion of biomass in a 10 kWth reactor with iron oxide as an oxygen carrier. Energy & Fuels 2009;23(5):2498-505.
[134] Gu H, Shen L, Xiao J, Zhang S, Song T. Chemical looping combustion of biomass/coal with natural iron ore as oxygen carrier in a continuous reactor. Energy & Fuels 2010;25(1):446-55.
[135] Gu H, Shen L, Zhong Z, Zhou Y, Liu W, Niu X, et al. Interaction between biomass ash and iron ore oxygen carrier during chemical looping combustion. Chemical Engineering Journal 2015;277:70-8.
[136] Pérez-Astray A, Adánez-Rubio I, Mendiara T, Izquierdo MT, Abad A, Gayán P, et al. Comparative study of fuel-N and tar evolution in chemical looping combustion of biomass under both iG-CLC and CLOU modes. Fuel 2019;236:598-607.
[137] Moldenhauer P, Sundqvist S, Mattisson T, Linderholm C. Chemical-looping combustion of synthetic biomass-volatiles with manganese-ore oxygen carriers. International Journal of Greenhouse Gas Control 2018;71:239-52.

[138] Directive E. Directive 2001/81/EC of the European Parliament and of the Council of 23 October 2001 on national emission ceilings for certain atmospheric pollutants (National Emissions Ceiling Directive). Official Journal of the European Communities 2001;27(2001):L309.
[139] Directive C. Directive 2010/75/EU of the European Parliament and of the Council. Off J Eur Union L 2010;334:17-119.
[140] Normann F, Andersson K, Leckner B, Johnsson F. Emission control of nitrogen oxides in the oxy-fuel process. Progress in Energy and Combustion Science 2009;35(5):385-97.
[141] Wang J, Ryan D, Anthony EJ, Wildgust N, Aiken T. Effects of impurities on CO2 transport, injection and storage. Enrgy Proced 2011;4:3071-8.
[142] Wang J, Wang Z, Ryan D, Lan C. A study of the effect of impurities on CO2 storage capacity in geological formations. International Journal of Greenhouse Gas Control 2015;42:132-7.
[143] Wang Z, Wang J, Lan C, He I, Ko V, Ryan D, et al. A study on the impact of SO2 on CO2 injectivity for CO2 storage in a Canadian saline aquifer. Applied Energy 2016;184:329-36.
[144] Neele F, Koornneef J, Jakobsen JP, Brunsvold A, Eickhoff C. Toolbox of Effects of CO2 Impurities on CO2 Transport and Storage Systems. Enrgy Proced 2017;114:6536-42.
[145] Glarborg P, Jensen AD, Johnsson JE. Fuel nitrogen conversion in solid fuel fired systems. Progress in Energy and Combustion Science 2003;29(2):89-113.
[146] Leckner B. Fluidized bed combustion: Mixing and pollutant limitation. Progress in Energy and Combustion Science 1998;24(1):31-61.
[147] Glarborg P. Fuel nitrogen conversion in solid fuel fired systems. Progress in Energy and Combustion Science 2003;29(2):89-113.
[148] Hill SC, Douglas Smoot L. Modeling of nitrogen oxides formation and destruction in combustion systems. Progress in Energy and Combustion Science 2000;26(4-6):417-58.
[149] Miller JA, Bowman CT. Mechanism and modeling of nitrogen chemistry in combustion. Progress in Energy and Combustion Science 1989;15(4):287-338.
[150] Zel'dovich YB. The Oxidation of Nitrogen in Combustion and Explosions Dokl. Akad Nauk SSSR 1946;51(3):213.
[151] Toftegaard MB, Brix J, Jensen PA, Glarborg P, Jensen AD. Oxy-fuel combustion of solid fuels. Progress in Energy and Combustion Science 2010;36(5):581-625.
[152] Normann F, Cheng M, Zhao D, Li Z, Cai N, Leion H. Oxidation of ammonia over a copper oxide-containing solid oxygen carrier with oxygen uncoupling capability. Combustion and Flame 2016;165:445-52.
[153] Bidwe A, Mayer F, Hawthorne C, Charitos A, Schuster A, Scheffknecht G. Use of ilmenite as an oxygen carrier in chemical looping combustion-batch and continuous dual fluidized bed investigation. Enrgy Proced 2011;4:433-40.
[154] Linderholm C, Cuadrat A, Lyngfelt A. Chemical-looping combustion of solid fuels in a 10 kWth pilot–batch tests with five fuels. Enrgy Proced 2011;4:385-92.
[155] Bohnet M. Mechanische Verfahrenstechnik. John Wiley & Sons; 2012.
[156] Geldart D. Types of gas fluidization. Powder technology 1973;7(5):285-92.
[157] Grace JR, Knowlton T, Avidan A. Circulating fluidized beds. Springer Science & Business Media; 2012.

[158] Yates JG, Lettieri P. Fluidized-Bed Reactors: Processes and Operating Conditions. Springer; 2016.
[159] Kunii D, Levenspiel O. Fluidization engineering. Elsevier; 2013.
[160] Bi H, Grace J. Flow regime diagrams for gas-solid fluidization and upward transport. International Journal of Multiphase Flow 1995;21(6):1229-36.
[161] Schmid JC, Pröll T, Kitzler H, Pfeifer C, Hofbauer H. Cold flow model investigations of the countercurrent flow of a dual circulating fluidized bed gasifier. Biomass Conversion and Biorefinery 2012;2(3):229-44.
[162] Kolbitsch P, Pröll T, Bolhàr-Nordenkampf J, Hofbauer H. Characterization of Chemical Looping Pilot Plant Performance via Experimental Determination of Solids Conversion. Energy & Fuels 2009;23(3):1450–5.
[163] Mayer K, Apanel G, Pröll T, Hofbauer H. Dual Fluidized Bed Reforming: Tar Conversion and the Fate of Sulfur. *2013 AIChE Annual Meeting.* San Francisco, USA; 2013.
[164] Wilk V, Hofbauer H. Conversion of fuel nitrogen in a dual fluidized bed steam gasifier. Fuel 2013;106:793-801.
[165] de Diego LF, Gayán P, García-Labiano F, Celaya J, Abad A, Adánez J. Impregnated CuO/Al2O3 Oxygen Carriers for Chemical-Looping Combustion: Avoiding Fluidized Bed Agglomeration. Energy & Fuels 2005;19(5):1850–6.
[166] Adánez J, Gayán P, Celaya J, de Diego LF, García-Labiano F, Abad A. Chemical Looping Combustion in a 10 kW th Prototype Using a CuO/Al2O3 Oxygen Carrier: Effect of Operating Conditions on Methane Combustion. Industrial & Engineering Chemistry Research 2006;45(17):6075–80.
[167] Gayán P, Forero CR, Abad A, de Diego LF, García-Labiano F, Adánez J. Effect of Support on the Behavior of Cu-Based Oxygen Carriers during Long-Term CLC Operation at Temperatures above 1073 K. Energy & Fuels 2011;25(3):1316–26.
[168] Arjmand M, Azad A-M, Leion H, Mattisson T, Lyngfelt A. Evaluation of CuAl2O4 as an Oxygen Carrier in Chemical-Looping Combustion. Industrial & Engineering Chemistry Research 2012;51(43):13924–34.
[169] Arjmand M, Azad A-M, Leion H, Lyngfelt A, Mattisson T. Prospects of Al2O3 and MgAl2O4 -Supported CuO Oxygen Carriers in Chemical-Looping Combustion (CLC) and Chemical-Looping with Oxygen Uncoupling (CLOU). Energy & Fuels 2011;25(11):5493–502.
[170] Mattisson T, Adánez J, Mayer K, Snijkers F, Williams G, Wesker E, et al. Innovative Oxygen Carriers Uplifting Chemical-looping Combustion. Enrgy Proced 2014;63:113-30.
[171] Penthor S, Mattisson T, Adánez J, Bertolin S, Masi E, Larring Y, et al. The EU-FP7 Project SUCCESS – Scale-up of Oxygen Carrier for Chemical Looping Combustion using Environmentally Sustainable Materials. Enrgy Proced 2017;114:395-406.
[172] Jacobs M, van der Kolk T, Albertsen K, Mattisson T, Lyngfelt A, Snijkers F. Synthesis and upscaling of perovskite Mn-based oxygen carrier by industrial spray drying route. International Journal of Greenhouse Gas Control 2018;70:68-75.
[173] Abad A, García-Labiano F, Gayán P, de Diego LF, Adánez J. Redox kinetics of CaMg0.1Ti0.125Mn0.775O2.9−δ for Chemical Looping Combustion (CLC) and Chemical Looping with Oxygen Uncoupling (CLOU). Chemical Engineering Journal 2015;269:67-81.

[174] de Diego LF, Garcı´a-Labiano F, Gayán P, Celaya J, Palacios JM, Adánez J. Operation of a 10kWth chemical-looping combustor during 200h with a CuO–Al2O3 oxygen carrier. Fuel 2007;86(7):1036-45.
[175] Rietveld HM. A profile refinement method for nuclear and magnetic structures. Journal of Applied Crystallography 1969;2(2):65-71.
[176] Knowlton TM, Hirsan I. The Effect of Pressure on Jet Penetration in Semi-Cylindrical Gas-Fluidized Beds. In: Grace JR, Matsen JM, editors. Fluidization. Boston, MA: Springer US; 1980, p. 315-24.
[177] Karri SR, Knowlton TM. Gas Distributor and. Flat-panel Display Technologies: Japan, Russia, Ukraine, and Belarus 1995:209.
[178] Zenz F. Bubble formation and grid design. *Institution of Chemical Engineers Symposium Series.* 1968:136-9.
[179] Shakhova N. Discharge of turbulent jets into a fluidized bed. Journal of engineering physics 1968;14(1):32-6.
[180] Merry J. Penetration of vertical jets into fluidized beds. AIChE Journal 1975;21(3):507-10.
[181] Blake T, Webb H, Sunderland P. The nondimensionalization of equations describing fluidization with application to the correlation of jet penetration height. Chemical Engineering Science 1990;45(2):365-71.
[182] Yates J, Bejcek V, Cheesman D. Jet penetration into fluidized beds at elevated pressures. Fluidization V 1986:79.
[183] Yang W-C, Keairns DL. Estimating the jet penetration depth of multiple vertical grid jets. Industrial & Engineering Chemistry Fundamentals 1979;18(4):317-20.
[184] Roach PE. The penetration of jets into fluidized beds. Fluid Dynamics Research 1993;11(5):197.
[185] Massimilla L. Gas jets in fluidized beds. Fluidization 1985.
[186] Chen L, Weinstein H. Shape and extent of the void formed by a horizontal jet in a fluidized bed. AIChE journal 1993;39(12):1901-9.
[187] Merker G, Teichmann R. Grundlagen Verbrennungsmotoren. Funktionsweise, Simulation Messtechnik, ; ATZ/MTZ-Fachbuch. Springer Fachmedien Wiesbaden: Wiesbaden, Germany; 2014.
[188] Abad A, García-Labiano F, de Diego LF, Gayán P, Adánez J. Reduction kinetics of Cu-, Ni-, and Fe-based oxygen carriers using syngas (CO+ H2) for chemical-looping combustion. Energy & Fuels 2007;21(4):1843-53.
[189] Mayer K. Ilmenite and mixtures with Olivine as oxygen carriers in a chemical looping combustion pilot plant. *Institute of Chemical, Environmental and Bioscience Engineering.* MSc. Vienna University of Technology; 2011.

Appendix

Paper hinzufügen